

Unraveling the electronic structure of silicon vacancy centers in 4H-SiC

Ali Tayefeh Younesi,¹ Minh Tuan Luu,¹ Christopher Linderälv,² Vytautas Žalandauskas,² Marianne Etzelmüller Bathen,² Nguyen Tien Son,³ Takeshi Ohshima,⁴ Gergő Thiering,⁵ Lukas Razinkovas,⁶ and Ronald Ulbricht¹

¹⁾Max-Planck Institut für Polymerforschung, Ackermannweg 10, 55128 Mainz, Germany

²⁾Department of Physics / Centre for Material Science and Nanotechnology, University of Oslo, Norway

³⁾Department of Physics, Chemistry and Biology, Linköping University, SE-58183, Linköping, Sweden

⁴⁾Takasaki Institute for Advanced Quantum Science, National Institutes for Quantum Science and Technology: QST, Gunma 370-1292, Japan; Department of Materials Science, Tohoku University, Miyagi 980-8579, Japan

⁵⁾Wigner Research Centre for Physics, Hungarian Academy of Sciences, PO Box 49, Budapest 1525, Hungary

⁶⁾Department of Fundamental Research, Center for Physical Sciences and Technology (FTMC), Vilnius LT-10257, Lithuania

(*Electronic mail: ulbricht@mpip-mainz.mpg.de)

(Dated: February 17, 2026)

Point defects in silicon carbide (SiC), particularly the negatively-charged silicon vacancy (V_{Si}^-) in 4H-SiC, are leading candidates for scalable quantum technologies due to their favorable spin-optical properties and compatibility with industrial semiconductor fabrication processes. Comprehensive knowledge of a defect's electronic structure is essential for interpreting spin-optical dynamics and for the reliable design and optimization of defect-based quantum devices. Despite extensive study, our knowledge of the electronic structure of V_{Si}^- is limited since key excited-state manifolds have remained inaccessible to conventional steady-state spectroscopy. In this study, transient absorption spectroscopy is utilized to probe non-equilibrium electronic transitions of V_{Si}^- and to uncover previously unobserved excited states. The first direct observation of the elusive V2' quartet transition is presented, with its broad spectral signature attributed to nonadiabatic vibronic coupling. Within the spin-doublet manifold, which is central to optically detected magnetic resonance (ODMR) but has remained unresolved spectroscopically, multiple optical transitions are identified. The complete electronic level structure in the relevant energy range is elucidated by combining polarization-resolved spectroscopy, group-theoretical analysis, quantum embedding calculations and first-principles optical lineshape modeling. Collectively, these results provide a microscopic understanding of the V_{Si}^- electronic structure. Our approach also establishes a general framework for resolving and understanding complex excited-state manifolds in wide-bandgap color centers.

Introduction

Point defects in wide-bandgap semiconductors have emerged as a promising platform for quantum information and sensing applications, primarily due to their favorable optical and spin properties. In light of the advancements in utilizing nitrogen vacancy (NV) centers in diamond as a quantum platform, there has been a growing demand for alternative host materials with properties comparable to or superior to diamond, albeit with a more straightforward manufacturing process. Silicon carbide (SiC) shows favorable characteristics in this context, enabling the creation of defects with electronic levels deep within the band gap that give rise to optically bright emission and long-lived, controllable spin states required for quantum applications.¹ Furthermore, the mature fabrication and processing of SiC² ensure CMOS (complementary metal-oxide-semiconductor) compatibility, enabling on-chip integration of optically addressable single spins with electronic and photonic devices.³⁻⁵

The negatively-charged silicon vacancy (V_{Si}^-) in 4H-SiC shows particular promise for a variety of applications, exhibiting single-photon emission in the near-infrared^{6,7} and millisecond spin coherence times⁷ at room temperature. V_{Si}^- is one of the few color centers, and the only one in SiC, where indistinguishable photon emission has been demonstrated.⁸ In short, the intriguing spin-photon interface,⁹ demonstrated

charge-state control,¹⁰⁻¹² Stark and strain tuning,^{13,14} Purcell enhancement¹⁵, and photonic integration¹⁶ of the V_{Si}^- all mark it as highly exploitable in next-generation scalable quantum devices for sensing, communication, and computing. While these properties highlight the technological potential of V_{Si}^- , a complete understanding of its electronic structure, central to both its fundamental description and future device concepts, remains lacking.

In this article, we comprehensively characterize the electronic structure of both spin channels of V_{Si}^- using a combination of experimental and theoretical methods, including transient absorption (TA) spectroscopy, group theory, density functional theory (DFT) and quantum embedding calculations. For the spin-quartet transitions, we identify the so far elusive V2' zero-phonon line (ZPL), which appears strongly broadened as compared to the other ZPLs. We attribute this behavior to non-adiabatic coupling to vibronic modes. In the spin doublet channel, we for the first time measure the spectroscopic signatures of the relevant optical transitions, from which we can infer the electronic structure using polarization-resolved TA spectra and group theory. The holistic methodology presented herein can be applied to other color centers and host materials, making it an interesting tool for characterizing their electronic structure to aid the broader development of color center-based quantum technologies.

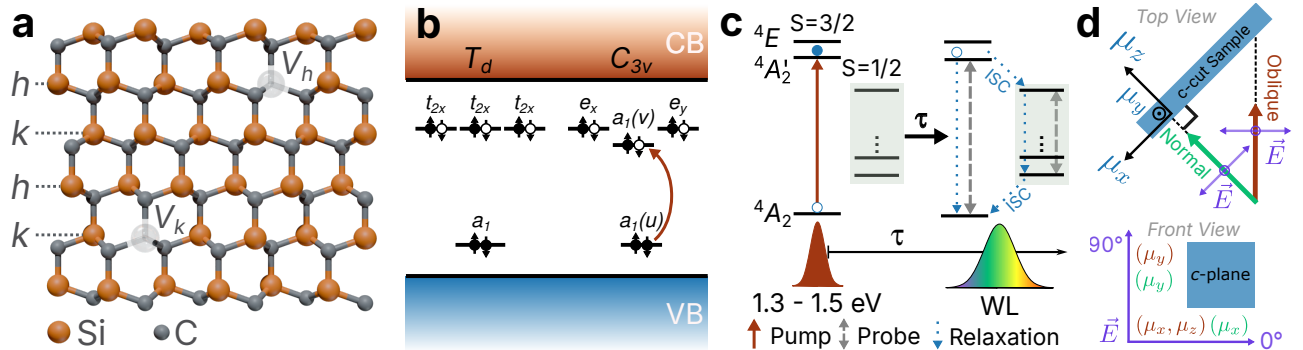


Figure 1. Overview. **a** Crystal structure of the V_{Si} center in 4H-SiC, with the basal-plane hexagonal (h) and quasi-cubic (k) lattice sites indicated. **b** Single-particle energy levels of V_{Si}^- . Left: Idealized T_d symmetry; Right: crystal-field splitting resulting in C_{3v} symmetry. Red arrow: excitation to $^4A'_2$ excited state. **c** Electronic states in the quartet ($S = 3/2$) and doublet ($S = 1/2$) spin channels and schematic of the transient absorption (TA) measurement scheme. **d** Top: Schematic of the probing geometry in both the oblique and normal incidence cases of V_{Si} electronic transitions relative to the c -plane, with a coordinate system for the transition dipole moments defined by μ_x , μ_y and μ_z . Purple arrows indicate the electric field vectors of the probe beam. Bottom: Front view of sample (c -plane), i.e., in the laser beam direction, with summary of the transition dipole moments (or "dipoles") excited by the 0° or 90° polarization of the electric field vector.

Results

The V_{Si} in 4H-SiC

We begin by describing the crystallographic environments and symmetry characteristics of the V_{Si} in 4H-SiC, which serve as the foundation for understanding its electronic structure. As illustrated in Fig. 1a, the Si-C bilayers in 4H-SiC stack along the crystallographic c -axis ([0001] direction), giving rise to two types of lattice sites: hexagonal (h) and quasi-cubic (k). Consequently, a silicon vacancy can occur in two inequivalent configurations, denoted V_h and V_k . Both share the same first-neighbor tetrahedral coordination, with local symmetry close to T_d , but they differ in the arrangement of their second-nearest neighbors. The actual point-group symmetry of both configurations is C_{3v} , with the threefold axis oriented along the crystallographic c -axis. The electronic structure of both the h and k vacancies can be described in terms of four molecular orbitals formed from the tetrahedrally oriented carbon dangling bonds surrounding the vacancy. Because the local symmetry is close to T_d , these orbitals can initially be classified according to the irreducible representations of this point group (left side of Fig. 1b): one a_1 orbital, given by the equal-weight linear superposition of the four carbon dangling bonds, and three degenerate orbitals of t_2 symmetry. Owing to its bonding character, the a_1 orbital lies lowest in energy, while the t_2 set resides at higher energies. When the symmetry is reduced from T_d to C_{3v} , the t_2 triplet splits into an orbital doublet of e symmetry and a singlet of a_1 symmetry (right side of Fig. 1b).

In the negatively charged state, the V_{Si}^- defect accommodates five electrons, giving rise to a rich electronic structure. The ground-state configuration, shown in Fig. 1b, is a spin quartet ($S = 3/2$) of A_2 orbital symmetry (4A_2). Optical excitation corresponds to promoting an electron from the lower-lying $a_1(u)$ orbital to either the $a_1(v)$ or e orbitals (as depicted by brown arrows in Fig. 1b), resulting in the $^4A'_2$ and 4E excited states, separated by a small crystal-field splitting, see Fig. 1c. The electronic structure further includes a spin-doublet ($S = 1/2$) channel that can be accessed through inter-

system crossing (ISC) between both spin channels.

The sharp zero-phonon lines (ZPLs) commonly observed in photoluminescence (PL) spectra of 4H-SiC have been identified with different configurations and excited states, namely V1 [1.439 eV, V_h], V1' [1.444 eV, V_h], and V2 [1.353 eV, V_k],⁶ see also Figs. 2a and 2b. These ZPLs are accompanied by broad phonon sidebands (PSBs) arising from the coupling of the electronic transitions to lattice vibrations (see Fig. 2).¹⁷ Interestingly, the V2' ZPL, which should arise from the transition to 4E of V_k and is predicted to lie 22 meV above $^4A'_2$,¹⁷ has not yet been observed.

While the quartet states and their associated transitions have been extensively characterized, considerably less is known about the spin-doublet channel of V_{Si}^- . This spin manifold can be populated from and de-populated to the quartet manifolds via ISC, which plays the key role in the spin polarization cycle that enables optically-detected magnetic resonance (ODMR) used in quantum applications. Despite this importance, ISC rates have only recently been measured¹⁸ and so far, the electronic structure of the $S = 1/2$ manifold has been established primarily through group-theoretical many-body analyses combined with physically motivated level ordering.^{9,19} Its role has only been inferred indirectly from spin-polarization dynamics rather than from direct spectroscopic observations.

Experimental conditions

To experimentally investigate the optical transitions and relaxation dynamics of V_{Si}^- ensembles, we employ TA spectroscopy, a pump–probe technique that has been successfully applied to NV centers in diamond.^{20–22} In this approach, a pump pulse excites the system, while a time-delayed probe monitors the resulting pump-induced change in sample transmission $\Delta T/T$. To this end, the photon energy of the pump pulse is tuned in the range of 1.3–1.5 eV to selectively excite ZPLs or the PSB associated with the V_{Si}^- quartet transitions, followed by broadband whitelight (WL) that transiently probes $\Delta T/T$ from 0.6–1.8 eV (see Fig. 1c), thereby monitoring both the quartet and doublet relaxation channels. Positive values of $\Delta T/T$ originate from ground-state bleaching

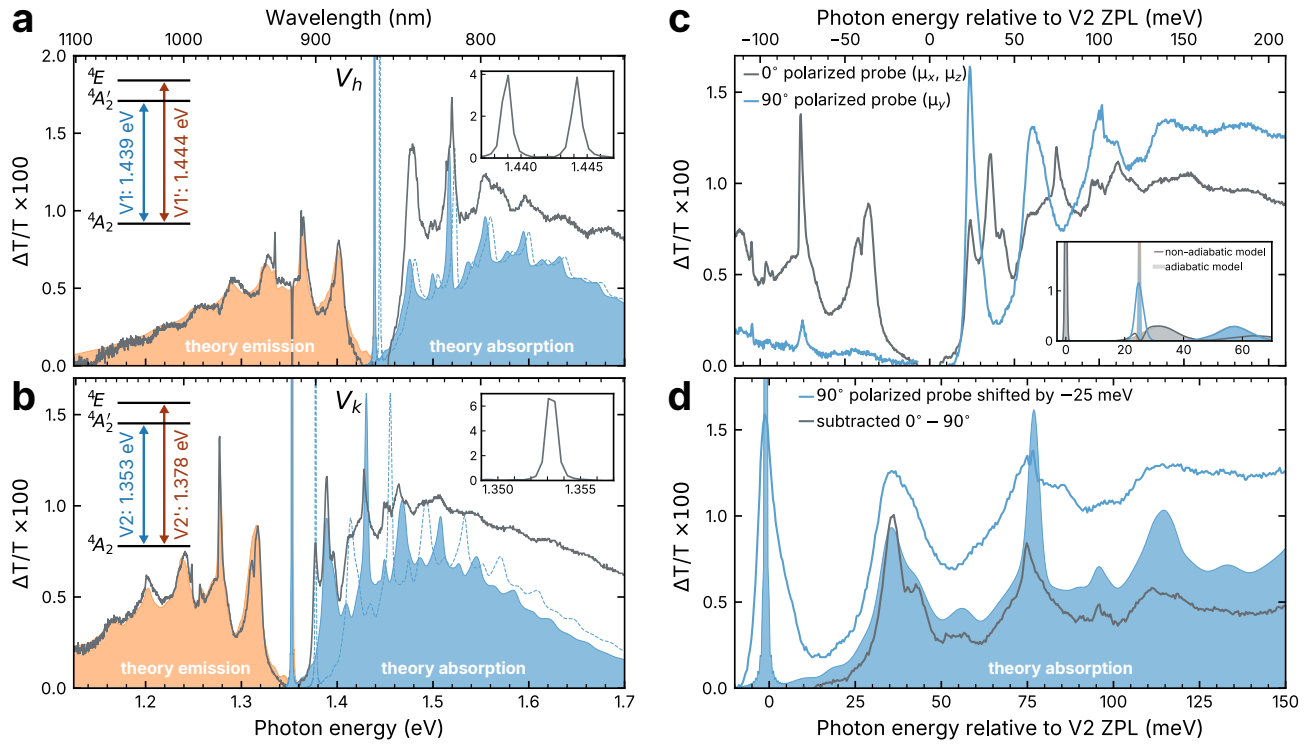


Figure 2. Spin-quartet electronic states and optical transitions. **a** V_h and **b** V_k : TA spectra at pump-probe delay of $t = 4$ ns (black curves), calculated PSBs of V1 and V2 in emission (orange shaded) and absorption (blue shaded); insets: enlarged version of the ZPL spectral regions (right) and electronic level scheme with optical transitions and transition energies in eV (left); **c** TA spectra of V_k for 0° and 90° probe polarizations with the energy axis referenced to the V2 ZPL; heuristic model simulating the broadening of the V2' ZPL in the inset; **d** TA spectra of V_k , focusing on the GSB by comparing the V2 PSB with absorption lineshape simulation (shaded) and V2' PSB red-shifted by 25 meV.

(GSB) and stimulated emission (SE) of the quartet transitions, whereas negative values arise from absorption of the doublet transitions.

The sample under study is a *c*-cut 4H-SiC wafer housed in a cryostat for measurements down to 4 K temperature. For the polarization components of the probe beam to access all possible transition dipole moments, the sample is held at an angle of either 0° ('normal incidence') or 45° ('oblique incidence') between the laser beams and the *c*-axis, see Fig. 1d. We define a coordinate system for the transition dipole moments μ , where μ_x and μ_y are within the *c*-plane and μ_z is perpendicular to it, i.e. along the *c*-axis (see Fig. 1d). Next to the normal or oblique incidence beam configurations, utilizing two orthogonal probe polarizations (0° and 90°) provides additional selectivity in picking certain transitions based on the optical selection rules. Where normal incidence only accesses polarization components within the *c*-plane (μ_x for 0° and μ_y for 90°), oblique incidence additionally also probes μ_z , however only for 0° ('*p*-polarization'). According to the optical selection rules for the quartet transitions, V1 and V2 only have active μ_z transition dipoles, whereas V1' and V2' have both μ_x and μ_y . Thus, in oblique incidence, 0° will probe all transitions (μ_x and μ_z), while 90° will probe only V1'/V2' (μ_y). In normal incidence, only V1'/V2' is probed for all polarizations (μ_x and μ_y).

Electronic structure of spin quartets

At early (< a few ns) pump-probe delays, the transient response is dominated by quartet optical transitions. Figs. 2a and 2b show $\Delta T/T$ (gray curves) for both the V_h and V_k configurations of V_{Si} under resonant ZPL excitation, with the ZPL region excluded due to the pump laser. The spectra exhibit broad PSBs, each comprising distinct vibronic peaks on the blue (GSB) and red (SE) sides, reflecting absorption and emission contributions, respectively. The insets in Fig. 2a and 2b show the ZPLs measured under excitation into the PSBs. In the inset of Fig. 2a, both the V1 and V1' ZPLs associated with the V_h configuration are clearly resolved and are separated by 5 meV, while in the inset of Fig. 2b, only one ZPL related to the V2 transition is visible in the displayed energy region.

To gain further insight into the vibronic structure behind the observed PSBs, Figs. 2a and 2b also show the overlaid theoretical absorption (blue shaded areas) and emission (orange shaded areas) lineshapes calculated for the $^4A_2 \leftrightarrow ^4A'_2$ optical transitions within the adiabatic Huang–Rhys (HR) model, see also Methods and Supplementary Section S20. For both the V1 and V2 transitions, the calculated emission lineshapes show strong agreement with the experimental data by capturing the overall redistribution of spectral weight and resolving most of the observed PSB fine structure. While at low temperatures the emission peaks can be explained by transitions

from the lower-lying $^4A'_2$ state, the vibronic peaks on the blue side (GSB) consist of two quartet absorption channels corresponding to the $^4A_2 \rightarrow ^4A'_2$ and $^4A_2 \rightarrow ^4E$ transitions. For the V_h configuration, the absorption lineshape calculated for the $^4A_2 \rightarrow ^4A'_2$ (V1) transition reproduces almost all observed vibronic features (blue shaded area in Fig. 2a), while the additional experimental broadening can be attributed to a second ZPL located 5 meV higher in energy. To illustrate this, we include an additional absorption lineshape, obtained by rigidly shifting the calculated $^4A_2 \rightarrow ^4A'_2$ lineshape by 5 meV to the V1' ZPL energy (dashed blue line in Fig. 2a). The ability of the adiabatic HR model to reproduce nearly all observed sideband features implies that non-adiabatic Jahn–Teller coupling within the 4E manifold and between the $^4A'_2$ and 4E states is not relevant.

Turning to the V_k configuration, the situation is qualitatively different. In contrast to V_h , only a single ZPL associated with the V2 transition is clearly observed in the experiment (inset of Fig. 2b). When overlaying the calculated absorption lineshape for the $^4A_2 \rightarrow ^4A'_2$ (V2) transition, it becomes evident that the observed GSB on the blue side cannot be explained by this channel alone. In particular, an additional absorption feature appears at approximately 25 meV above the V2 ZPL, which cannot be associated with a characteristic vibrational resonance of the V2 transition (\approx 35 meV above ZPL). Notably, this energy separation is close to the theoretically predicted splitting between the V2 and V2' ZPLs (22 meV), as reported in Ref. 17. Motivated by this proximity, we tentatively include an additional absorption contribution obtained by rigidly shifting the calculated V2 absorption lineshape by 25 meV (dashed blue line in Fig. 2b). The resulting superposition reproduces several additional features in the experimental PSB, suggesting that overlapping absorption from two transitions may contribute to the observed spectrum.

Assuming that the absorption feature observed 25 meV above the V2 ZPL corresponds to the $^4A_2 \rightarrow ^4E$ transition, we next turn to polarization-resolved experiments designed to test this hypothesis. From symmetry considerations, the $^4A_2 \rightarrow ^4A'_2$ transition is expected to have a transition dipole moment that is oriented perpendicular to the c -plane (μ_z), whereas the $^4A_2 \rightarrow ^4E$ transition should exhibit an in-plane polarization (μ_x and μ_y). Fig. 2c shows the corresponding TA spectra measured at oblique incidence using two orthogonal probe polarizations. For the 0° -polarized probe, which contains both out-of-plane and in-plane polarization components, contributions from both quartet transitions are expected and indeed observed, resulting in pronounced GSB and SE features. In contrast, the 90° -polarized probe predominantly samples the in-plane response and therefore probes mainly the $^4A_2 \leftrightarrow ^4E$ channel, exhibiting almost no SE and yielding a clear GSB signal that closely resembles an absorption lineshape, with an apparent ZPL located approximately 25 meV above the V2 transition and an associated PSB.

To further support this assignment, we analyze the polarization-resolved GSB line shapes in more detail. Fig. 2d shows the 90° -polarized GSB spectrum, where the first peak is shifted to zero energy and treated as an effective ZPL (blue line), together with the calculated absorption lineshape (blue

shaded area). The agreement between features in both lines confirms that this feature indeed corresponds to a ZPL accompanied by its PSB. In addition, Fig. 2d also displays the 0° -polarized spectrum (dark line) after subtracting the 90° -polarized contribution to effectively remove the absorption feature located 25 meV above the V2 ZPL. Notably, the resulting sideband shows the same set of vibronic peaks as the shifted 90° spectrum and the calculated absorption lineshape, indicating that all three spectra essentially share the same phonon sideband structure.

The only remaining feature that cannot be explained within the adiabatic framework is the anomalous linewidth of the V2' ZPL, which is broader by a factor of about eight compared to the other quartet ZPLs (see Supplementary Table S8). To rationalize this behavior, we introduce an effective many-mode vibronic model that captures non-adiabatic Jahn–Teller-type interactions between the $^4A'_2$ and 4E quartet manifolds. The main idea is that the nominal zero-phonon state of the 4E manifold becomes resonantly coupled to a dense set of vibronic states originating from the $^4A'_2$ configuration. This coupling occurs because the V2' ZPL lies within an energy range (around 25 meV) that overlaps with the frequency range of the first vacancy-related vibrational resonance (corresponding to the first PSB peak at about 35 meV). As a result, the oscillator strength of a single transition is redistributed among many closely spaced vibronic states, effectively broadening the observed ZPL. The result is shown in the inset of Fig. 2c, where lineshapes for the two orthogonal polarizations are modeled both without vibronic coupling (shaded areas) and with vibronic coupling included (solid lines); see Supplementary Section S8. Our model captures the core physics and reproduces the broadening of the V2' ZPL, resulting in a lineshape that resembles the experimental ZPL.

The five times larger energy difference between $^4A'_2$ and 4E for V_k as compared to V_h (25 meV vs. 5 meV) explains why previous PL measurements did not detect V2': because these measurements are usually done at cryogenic temperatures, the population of 4E after photoexcitation, as described by the Boltzmann distribution, is simply too low to be observed in PL. Absorption measurements (or here: GSB in TA) capture both transitions regardless of temperature. However, the non-adiabatic broadening of the V2' ZPL makes it easy to be mistaken for a vibronic peak.

Optical transitions in the spin doublet channel

By analyzing the TA dynamics over extended timescales, we can track the entire spin-polarization cycle by monitoring relevant electronic transitions. This is demonstrated in Fig. 3a, which displays spectro-temporal TA results obtained under broadband excitation into the PSB of the V_h and V_k quartet transitions (\approx 1.55 eV). The data show positive differential transmission signals (red) linked to the quartet transition, as well as new absorptive features (blue) corresponding to the expected doublet transitions. The measurement was conducted at oblique incidence using unpolarized probe light, ensuring that all components of the transition dipole moment (μ_x , μ_y and μ_z) are detected.

Fig. 3b schematically shows the electronic energy levels and relaxation time constants for the V_h and V_k configura-

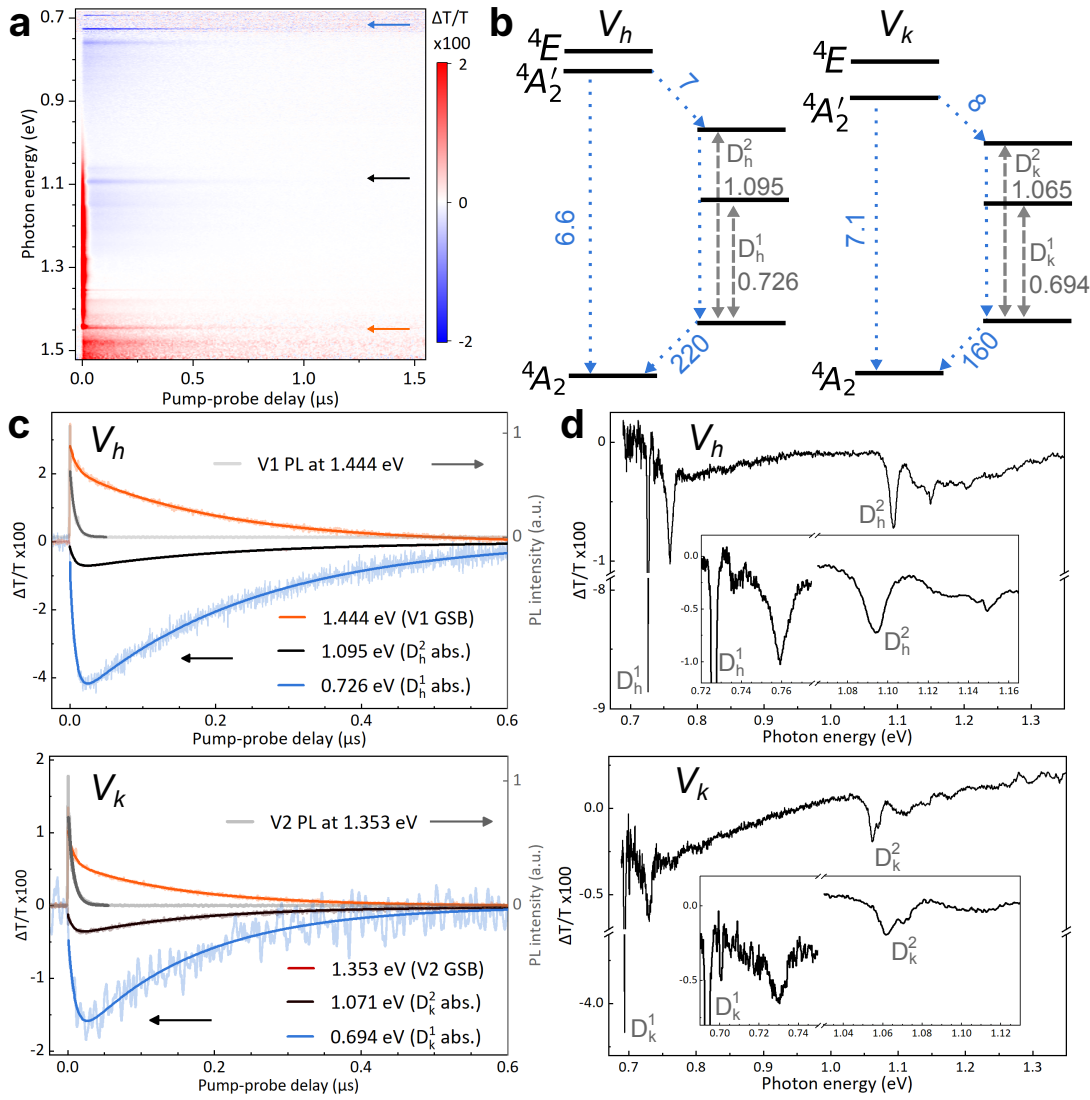


Figure 3. Spin-doublet electronic states and optical transitions. **a** Spectrally-resolved TA dynamics for V_h and V_k ; colored arrows indicate transitions whose dynamics are shown in panel c. **b** Extracted electronic level scheme and relaxation dynamics of V_h and V_k . Gray dashed arrows denote optical transition energies (in eV), while blue dashed arrows indicate relaxation pathways with time constants (in ns). **c** TA dynamics of spin-quartet and spin-doublet transitions and PL decay (right axis) of spin-quartet transitions of V_h and V_k ; **d** TA spectra of spin-doublet transitions of V_h and V_k at a pump–probe delay of 90 ns. The insets show magnified views of selected doublet features.

tions, as determined from this and complementary measurements. The blue-dashed arrows are relaxation pathways with time constants in ns, whereas gray-dashed arrows denote the observed doublet transitions with photon energies in eV. For each defect site (h and k), two doublet transitions are observed: the first around 0.7 eV (D_h^1 and D_k^1) and the second around 1.1 eV (D_h^2 and D_k^2), which appear as blue features in Fig. 3a.

Fig. 3c shows the dynamics of the relevant transitions for both V_h (top) and V_k (bottom) sites (semi-transparent lines), along with fits to the appropriate kinetic models (solid lines). The gray traces represent time-resolved PL measurements of the V1 and V2 ZPLs, which were fitted using an exponential decay model to determine the $4A_2'$ to $4A_2$ radiative lifetimes shown in Fig. 3b. The orange trace shows the TA GSB dy-

namics of the V1 and V2 ZPLs, exhibiting a bi-exponential decay with a fast component associated with the upper ISC (7 ns and 8 ns for V_h and V_k , respectively), and a slow component governed by the lower ISC (220 ns for V_h and 160 ns for V_k). The numbers for the lower ISC time are in very good agreement with previous results¹⁸, whereas the values for the upper ISC time are in good agreement with the radiative lifetime of the quartet transition as measured with time-resolved PL (Fig. 3c).

The blue and black plots in Fig. 3c show the TA dynamics of absorption (i.e., negative $\Delta T/T$ values) from the two doublet transitions D^1 and D^2 , as illustrated in Fig. 3b. Both signals initially display an increasing negative $\Delta T/T$ amplitude, followed by a decrease at longer pump–probe delays. The initial rise is attributed to population transfer from the quartet

to the doublet spin channel via the upper ISC, while the subsequent decline indicates doublet-to-quartet relaxation via the lower ISC. The observed timescales align with those derived from the quartet GSB dynamics (see Supplementary Sections S14 and S15). The lifetime of the upper doublet state cannot be directly resolved in our TA measurements. Such a state would give rise to stimulated emission at early pump–probe delays, as observed for spin-singlet states in NV centers²³. While our sub-picosecond time resolution is adequate, the expected weak doublet SE signal is masked by the dominant SE of the quartet transition.

To better isolate the doublet spectral signatures of the V_h and V_k configurations, we resonantly excited the V1 and V2 ZPLs to enable a clear separation of their respective TA responses. The TA spectra at a pump–probe delay of 90 ns are shown in Fig. 3d, with the V_h and V_k configurations displayed in the top and bottom panels, respectively. The D^1 ZPLs appear as sharp resonances with approximately 1.5 meV linewidth, similar to most of the quartet ZPLs, at transition energies of 0.726 eV (D_h^1) and 0.694 eV (D_k^1). Both ZPLs are accompanied by distinct vibronic peaks about 35 meV to the blue side, like for the quartet transitions. A second set of transitions are found at around 1.095 eV for V_h (D_h^2) and about 1.07 eV for V_k (D_k^2). The insets of Fig. 3d show an enlarged version of these peaks, revealing a splitting of the transition in two components, most pronounced for D_k^2 . This double-peak feature becomes clearer in the probe polarization dependence that we will discuss further down, while the data shown here were recorded with an unpolarized probe.

Electronic structure of spin doublets

Having established the energies and kinetics of the spin-doublet transitions, we now turn to their microscopic interpretation. In the following, we analyze the symmetry structure of the doublet manifold, resolve the ordering of the states using group theory and quantum embedding calculations, examine crystal-field splittings, and derive the resulting optical selection rules and polarization dependence.

As discussed earlier, the silicon vacancy center is conveniently described within a near- T_d local environment. The C_{3v} symmetry results from a weak trigonal distortion, as shown by the small splittings observed in the excited quartet manifold (5 meV and 25 meV for V_h and V_k , respectively). This indicates that the $T_d \rightarrow C_{3v}$ crystal field acts only as a minor perturbation. Therefore, the dominant energy separations correspond to the term splittings emerging from many-body electron–electron interactions already present in ideal T_d symmetry. This type of energy scale supports the construction of many-body electronic states within the parent T_d symmetry for simplicity, accompanied by the treatment of the C_{3v} crystal field as a small perturbation.

Within T_d symmetry, the low-energy electronic structure of a t_2^3 hole configuration is well described by classical multiplet theory.²⁴ The spin-doublet manifold consists of three distinct symmetry terms: 2T_1 , 2E , and 2T_2 . This framework places the 2T_2 term as the highest energy term of the t_2^3 manifold, whereas the relative ordering of the remaining 2T_1 and 2E terms cannot be determined from symmetry considerations alone (see Supplementary Section S10). As a consequence, the detailed

ordering of the spin-doublet manifold must be established beyond symmetry arguments. Moreover, the multi-determinant character of the doublet states prevents a description within standard single-determinant DFT, motivating the use of quantum embedding methodologies.^{25–28} This approach allows for an explicit treatment of electronic correlations on top of a mean-field DFT description by separating a localized active space of defect electronic degrees of freedom from the surrounding bulk environment and solving the many-body problem within this space beyond the single-determinant level.

Quantum embedding calculations for V_k were performed using an active space with four Wannierized spatial orbitals, as detailed in the Methods and Supplementary Section S9. The resulting energy level structure for the maximum spin projections ($m_s = 3/2$ and $m_s = 1/2$) is shown in Fig. 4a. Within the quartet ($S = 3/2$) manifold, the second excited state is located 1.52 eV above the ground state, which aligns well with the experimental ZPL (≈ 1.4 eV). However, contrary to the experimental data, an artificial splitting between three excited quartet levels is observed. This splitting should be regarded as a methodological artifact stemming from the approximate nature of the Wannier construction and the inability to preserve point-group symmetry in the embedded system.

Within the spin-doublet manifold depicted in Fig. 4a, the calculated energy levels form three distinct groups, centered at approximately 0.26 eV (three states), 0.84 eV (two states), and 1.12 eV (three states) above the ground state. This grouping, together with the T_d symmetry analysis described above, allows for identification of the lowest spin-doublet as possessing 2T_1 character, while the next higher doublet exhibits 2E character. The calculated transition energies between these multiplets, 0.6 eV and 0.9 eV, are in favorable agreement with the experimentally observed values of approximately 0.7 eV and 1.1 eV for the D^1 and D^2 transitions, respectively (Fig. 3b).

Following the identification of the relevant electronic multiplets within the parent T_d symmetry, we analyze the term structure and polarization dependence in the actual C_{3v} symmetry (for group-theoretical details, see Supplementary Sections S10 and S12). Fig. 4b shows the already discussed quartet channel, where orange arrows indicate polarization within the basal c -plane (μ_x and μ_y), while blue arrows correspond to polarization along the crystallographic c -axis (μ_z). With the exception of the 4T_1 crystal-field splitting of V_k (25 meV), the description is consistent with previous work⁶.

Fig. 4c extends this discussion to the spin-doublet channel. Within the C_{3v} crystal field, both spin-doublet T terms split into an orbital singlet and a doublet, i.e., $^2T_1 \rightarrow ^2E' \oplus ^2A_2$ and $^2T_2 \rightarrow ^2E'' \oplus ^2A_1$. Although symmetry considerations alone do not determine the relative ordering of the $^2E'$ and 2A_2 sub-levels from 2T_1 , group-theoretical analysis predicts an inverted ordering for the 2T_2 splitting compared to the quartet case, resulting in an $^2E''$, 2A_1 energy sequence (see Supplementary Section S11). In contrast to the quartet manifold, symmetry arguments predict that linear crystal-field splitting should vanish for the spin-doublet T levels. The finite splittings observed experimentally, as discussed below, could therefore be attributed to higher-order crystal-field effects or coupling to other T states that are not considered in our analysis (e.g., resulting from $a_1t_2^2$ configuration).

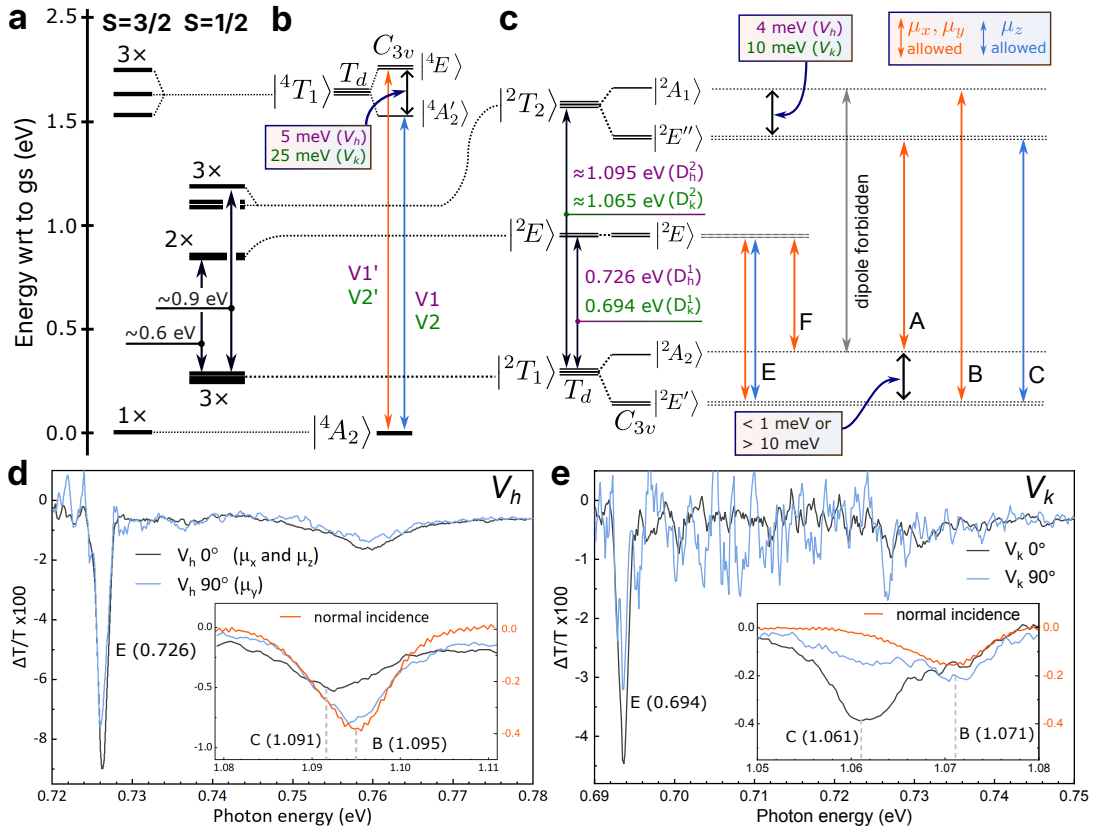


Figure 4. Electronic structure and optical selection rules of spin-doublet and spin-quartet channels. **a** Electronic levels for V_h calculated using quantum embedding. **b,c** Electronic structure and optical selection rules of the spin-quartet and spin-doublet channels, respectively. **d,e** TA probe polarization dependence of spin-doublet transitions for the V_h and V_k configurations, measured under oblique incidence (blue and black traces) and normal incidence (orange traces).

Deriving the multiplet structure from the parent T_d symmetry imposes additional constraints on the optical selection rules for sublevels of doublet T states beyond those obtained from C_{3v} symmetry alone (see Supplementary Section S12). Specifically, transitions between the E' and E'' levels are allowed only for z -polarized light (transition C in Fig. 4c), while in-plane polarization induces transitions from A to E states (transitions A and B in Fig. 4c). In contrast, a description within C_{3v} symmetry would allow E to E transitions for all polarizations, as is the case for transitions between $^2E'$ and 2E (transition E in Fig. 4c). Finally, the transition F from 2A_2 to 2E is restricted to in-plane polarization.

Having established the group-theoretical framework, we turn to polarization-resolved TA measurements to examine the optical selection rules of the doublet transitions. Figs. 4d and 4e show the polarization-resolved TA spectra of the D^1 transition for V_h and V_k , respectively. The spectra were measured at 5 K at oblique incidence with 0° and 90° probe polarizations probing (μ_x, μ_z) and μ_y dipoles. The insets display the corresponding D^2 spectra measured for 0° , 90° , and normal incidence, the latter being sensitive only to the in-plane dipole components (μ_x, μ_y) irrespective of the probe polarization. From the group-theoretical analysis it follows that the D^1 transition should be composed of the E and F sub-transitions. However, we can only observe a single resonance

that is of Gaussian shape with a linewidth of 1.5 meV, in contrast to the Lorentzian-shaped V1, V1' and V2 ZPLs that have about 0.8 meV linewidth. This larger linewidth with Gaussian lineshape is most likely because for D^1 we are limited by the spectral measurement resolution in this energy range (see Supplementary Section S1).

Observing only one resonance instead of two (E and F, see Fig. 4c) could have two reasons. First, a single resonance would be observed if the splitting of 2T_1 is much less than 1 meV, effectively merging E and F into a single transition in our measurements. Another possibility is that the splitting is large enough for the 2A_2 level not to be thermally populated at 5 K. We therefore measured D^1 at 60 K, anticipating the appearance of the F transition as a new peak to the red side of the E transition, which however was not detected (see Supplementary Section S18). The absence of the F transition at both 5 K and 60 K sample temperature leads us to estimate the 2T_1 splitting to be either larger than 10 meV or smaller than 1 meV, see Supplementary Section S18.

The probe-polarization dependence for D^1 transitions (insets in Figs. 4d and 4e) reveals a slight reduction of the D^1 amplitude when changing from 0° to 90° polarization. This behavior is consistent with the expected electronic structure if 2A_2 lies above the E level, since the probe sensitivity changes from (μ_x, μ_z) to μ_y , i.e., the polarization component along the

c direction is suppressed.

Finally, we turn to the D^2 transitions, shown in the insets of Figs. 4d and 4e. In contrast to D^1 , the polarization dependence is markedly different. Here, the relevant sub-transitions are A, B, and C, and the insets reveal a characteristic double-peak structure with central energies of 1.091 eV and 1.095 eV for D_h^2 , and 1.061 eV and 1.071 eV for D_k^2 (see Supplementary Section S17 for quantitative peak fits).

We can thus conclude that the 2T_2 splitting is 4 meV (V_h) and 10 meV (V_k). In normal incidence (orange plots), which probes μ_x and μ_y but not μ_z (and thus only the B transition), we only observe the high-energy transitions (1.095 eV and 1.071 eV), which must be the B transition. It follows that $^2A_1 > E''$ in 2T_2 and that the low-energy transition (1.091 eV and 1.061 eV) corresponds to C. We performed further TA measurements of the D^2 transitions at normal incidence, where we varied the sample temperature from 5 K to 120 K (see Supplementary Section S18). Only very subtle changes in the A, B and C transitions were observed, which is consistent with our hypothesis of the 2T_1 splitting being < 1 meV or > 10 meV. The assignment of C to the low-energy transition is consistent with the fact that in oblique incidence, its peak amplitude is reduced when going from 0° to 90° (black and blue plots in Fig. 4d and 4e), i.e. from probing μ_x and μ_z to μ_y , since this is the only transition containing μ_z components.

Having determined the electronic structure of the doublet channel, we want to conclude this section with a short discussion on the linewidths of the doublet transitions. Whereas the linewidth of D^1 is similar to $V1$, $V1'$ and $V2$ (around 1 meV), the linewidth of D^2 is broader and more akin to $V2'$ (6-8 meV). For $V2'$, we explained the broadening with non-adiabatic coupling to vibronic modes of $V2$ that redistributes its oscillator strength, resulting in the observed broadening. This approach seems less justified for D^2 due to the paucity of vibronic modes in the relevant energy range, which is 25 meV for $V2'$ vs. 4 meV (D_h^2) and 10 meV (D_k^2), and the fact that $V1'$ is not broadened with a distance to $V1$ of 5 meV, i.e. very similar to D_h^2 . We are currently not able to explain this broadening. It could be related to Jahn–Teller-induced effects in E'' that couple it to 2A_1 , resulting in additional dephasing processes that broaden the linewidth.²⁹ This would not occur in the quartet excited state since the splitting there is inverted and $^4E > ^4A_2'$.

Discussion

In conclusion, we extended the known electronic structure landscape of V_{Si}^- in 4H-SiC via a combination of experimental and theoretical techniques, including transient absorption spectroscopy, density functional theory, quantum embedding calculations and group theory. We spectroscopically characterized and analyzed the spin quartet and spin doublet transitions by taking into account the optical polarization dependencies with respect to the crystal orientation and the resulting optical selection rules. For the quartet transitions, we identify the so far elusive $V2'$ ZPL at a photon energy that is 25 meV higher than the $V2$ ZPL. This $V2'$ ZPL appears strongly broadened as compared to the $V1$, $V1'$ and $V2$ ZPLs, which we attribute to non-adiabatic coupling to vibronic modes of the $V2$ transition. A heuristic model is shown to qualitatively

reproduce the broadening effect. Future work could address the underlying mechanism in more detail, both experimentally by, e.g., employing multidimensional coherent spectroscopy, as well as theoretically using non-adiabatic *ab initio* simulations. We also calculate the full absorption and emission line-shapes, including phonon sidebands, of the spin quartet transitions of V_{Si}^- in excellent agreement with the measured spectra.

In the spin doublet channel, we for the first time measure the spectroscopic signatures of the V_{Si}^- electronic transitions that reveal important details about the doublet channel electronic structure, which is expanded upon using quantum embedding methods and group theory. Each defect configuration (V_h and V_k) shows two distinct doublet absorption transitions from the lowest doublet level 2T_1 : D_h^1 and D_k^1 in the 0.7 eV range and D_h^2 and D_k^2 in the 1.1 eV range. Furthermore, the ZPLs of the D^2 transitions show a double peak structure that we attribute to a crystal-field splitting of the 2T_2 excited state into 2A_1 and 2E levels (4 meV for V_h and 10 meV for V_k), similar to the quartet transitions, where it is 5 meV for V_h and 25 meV for V_k . The identified doublet transitions suggest a possible alternative ODMR readout signal to the commonly measured quartet PL. Similar to the singlet transition of NV centers in diamond^{30,31}, the absorption or PL of the doublet transitions could be exploited as a signal for ODMR. This approach could be beneficial for quantum technologies with fiber-based access, since the doublet transitions are situated in the important telecom wavelength range. It is conceivable that employing the doublet transitions for ODMR could improve the spin contrast, as is the case for the singlet transitions of NV centers in diamond^{31,32}, which would be interesting to investigate in future work. Our determination of the doublet level energies could potentially also aid in improving state-selective photoionization that forms the basis of photoelectric detection of magnetic resonance (PDMR).^{33,34}

Our combined experimental and theoretical approach described here can be applied to other color centers and host materials, marking it as a versatile toolbox for characterizing their electronic structure to aid the broader development of color center-based quantum technologies. TA spectroscopy can be applied to other ‘quantum defects’, where metastable transitions (and excited states in general) have not been identified yet, such as the boron vacancy in hexagonal boron nitride (h-BN).^{35,36} Depending on the crystal structure and defect symmetries, polarization-resolved TA spectra combined with optical selection rules derived by group theory and *ab initio* methods can then be used to infer details about the defect’s electronic structure.

Methods

Spectroscopy and Materials

We employed two TA spectroscopy setups, one for long timescale dynamics (ns- μ s)²⁰ and another setup for short timescales (fs-ns)²¹. As a pump, we either use an optical parametric oscillator (OPO, Ekspla NT242) that generates wavelength-tunable narrowband pulses with few-ns pulse duration or a non-collinear optical parametric amplifier (NOPA, AG Riedle) that generates broadband pulses with sub-ps pulse duration. The SiC sample was housed in a

closed-cycle Helium-cooled cryostat. We used a high-purity semi-insulating (HPSI) 4H-SiC sample that was irradiated by 2-MeV electrons at room temperature to a fluence of $8 \times 10^{18} \text{ cm}^{-2}$ at room temperature. More details can be found in Supplementary Section S1.

Lineshape calculations

Lineshape calculations were performed utilizing spin-polarized density functional theory with the meta-GGA $r^2\text{SCAN}$ functional³⁷ and a force-constant embedding approach, which facilitates the description of defect electron–phonon coupling in the dilute limit.^{38,39} The methodology considerably reduces finite-size effects that arise from restricted supercell geometry, such as the limited number of vibrational modes and insufficient representation of coupling to long-wavelength phonons, thereby enabling the calculation of high-resolution optical lineshapes.

Optical lineshapes are computed for transitions between 4A_2 and ${}^4A'_2$ states using the adiabatic Huang–Rhys framework.^{40,41} Mode-resolved Huang–Rhys factors are determined by calculating the displacement between the equilibrium geometries of the ground- and excited-state potential-energy surfaces in a large supercell. These displacements are then projected onto the phonon eigenmodes of the embedded system. The resulting absorption and emission spectra are evaluated using the generating-function formalism.^{42,43}

Non-adiabatic vibronic coupling between near-degenerate electronic states, including Jahn–Teller effects, is not considered in this DFT based study. Additional technical details about the density functional theory parameters, embedding procedure, phonon calculations, and lineshape evaluation are available in the Supplementary Information.

Group-theory framework

Since the trigonal crystal field in 4H-SiC represents only a minor perturbation to the local tetrahedral environment, the primary energy separations of the silicon vacancy center are dictated by the intrinsic multiplet structure of the underlying many-body configurations in ideal T_d symmetry. Specifically, the low-energy electronic structure is determined by the multiplet splittings of the $a_1t_2^2$ and t_2^3 hole configurations, which result from two-body Coulomb and exchange interactions and are well described by classical multiplet theory.²⁴ Conversely, starting directly from C_{3v} symmetry and constructing many-body states based on the occupation of slightly split single-particle levels ($t_2 \rightarrow a_1(v) \oplus e$) can obscure the parent multiplet structure and potentially result in an incorrect ordering of the many-body energy levels.

Therefore, a T_d -based description is adopted as the starting point. Within T_d symmetry, the lowest-lying spin-doublet manifold originates from the t_2^3 hole (or equivalently, electron) configuration, whose term structure is well established in classical multiplet theory.²⁴ The corresponding many-body wavefunctions are detailed in Supplementary Note S10S10.1.

To analyze the polarization dependence of the optical transitions, the resulting electronic terms are reformulated in a symmetry-adapted basis whose components transform as irreducible representations of the C_{3v} point group. This is accomplished by transforming the standard representation matrices

of the T_2 irreducible representation of T_d so that its components correspond to the A_1 and E representations of the C_{3v} subgroup. This procedure is equivalent to rotating the coordinate system so that the z -axis is aligned with the crystallographic c -axis and coincides with the C_{3v} rotational axis, while the x - and y -axes lie within the basal plane of 4H-SiC. This method preserves the underlying T_d multiplet structure and at the same time allows the electronic states to be treated as eigenstates of C_{3v} symmetry. Additional technical details regarding the basis construction and symmetry reduction are provided in Supplementary Section S12.

cRPA+FCI calculations

The cRPA calculations were performed in the VASP software package⁴⁴ to extract screened two-body Coulomb matrix elements. The minimal active space consisted of 4 spatial orbitals localized on the neighboring atoms. Localization was performed using the Wannier90 package as interfaced with vasp. Eigenvalues from DFT calculations were used as approximations to the one-body matrix elements. The mean-field electron-electron interaction was removed but the exchange-correlation energy contribution from the active space to the one-body matrix elements remained. The resulting Hamiltonian was diagonalized using full configuration interaction in an in-house implementation. A 128 atom supercell was used in conjunction with Γ -point sampling of the Brillouin zone. A plane wave cutoff of 520 eV was used. Further details are given in Supplementary Sections S9 and S21.

Data availability

The data that support the findings of this study are available from the corresponding author upon request. Source data are provided with this paper.

References

- 1 C. P. Anderson, A. Bourassa, K. C. Miao, G. Wolfowicz, P. J. Mintun, A. L. Crook, H. Abe, J. Ul Hassan, N. T. Son, T. Oshima, and D. D. Awschalom. Electrical and optical control of single spins integrated in scalable semiconductor devices. *Science*, 366:1225–1230, 2019.
- 2 T. Kimoto and J. A. Cooper. *Fundamentals of Silicon Carbide Technology: Growth, Characterization, Devices and Applications*. Wiley, 2014.
- 3 Stefania Castelletto, Brett C. Johnson, and Alberto Boretti. Visible and infrared photoluminescence in hexagonal silicon carbide by direct femtosecond laser writing. *IOP Conf. Ser.: Mater. Sci. Eng.*, 840:012010, 2020.
- 4 Victoria A. Norman, Sridhar Majety, Zhipan Wang, William H. Casey, Nicholas Curro, and Marina Radulaski. Novel color center platforms enabling fundamental scientific discovery. *InfoMat*, pages 1–24, 2020.
- 5 Marianne Etzelmüller Bäthen and Lasse Vines. Manipulating single-photon emission from point defects in diamond and silicon carbide. *Advanced Quantum Technologies*, 4(7):2100003, 2021.
- 6 Erik Janzén, Adam Gali, Patrick Carlsson, Andreas Gällström, Björn Magnusson, and N.T. Son. The silicon vacancy in SiC. *Physica B: Condensed Matter*, 404(22):4354–4358, dec 2009.
- 7 Matthias Widmann, Sang-Yun Lee, Torsten Rendler, Nguyen Tien Son, Helmut Fedder, Seoyoung Paik, Li-Ping Yang, Nan Zhao, Sen Yang, Ian Booker, Andrej Denisenko, Mohammad Jamali, S. Ali Momenzadeh, Ilja Gerhardt, Takeshi Ohshima, Adam Gali, Erik Janzén, and Jörg Wrachtrup. Coherent control of single spins in silicon carbide at room temperature. *Nature Materials*, 14(2):164–168, dec 2015.
- 8 N. Morioka, C. Babin, R. Nagy, I. Gediz, E. Hesselmeier, D. Liu, M. Joliffe, M. Niethammer, D. Dasari, V. Vorobyov, R. Kolesov, R. Stöhr, J. Ul Hassan, N. T. Son, T. Ohshima, P. Udvarhelyi, G. Thiering, A. Gali, J. Wrachtrup, and F. Kaiser. Spin-controlled generation of indistinguishable and distinguishable photons from silicon vacancy centres in silicon carbide. *Nature Communications*, 11:2516, 2020.

⁹Ö. O. Soyal, P. Dev, and S. E. Economou. Silicon vacancy center in 4H-SiC: Electronic structure and spin-photon interfaces. *Physical Review B*, 93:081207(R), 2016.

¹⁰Gary Wolfowicz, Christopher P. Anderson, Andrew L. Yeats, Samuel J. Whiteley, Jens Niklas, Oleg G. Poluektov, F. Joseph Heremans, and David D. Awschalom. Optical charge state control of spin defects in 4h-sic. *Nature Communications*, 8(1):1876, 2017.

¹¹Marianne Etzelmüller Bathen, Augustinas Galeckas, Johanna Müting, Hussein M. Ayedh, Ulrike Grossner, José Coutinho, Ymir Kalmann Frodason, and Lasse Vines. Electrical charge state identification and control for the silicon vacancy in 4h-sic. *npj Quantum Information*, 5(1):111, 2019.

¹²M. Widmann, M. Niethammer, D. Yu. Fedyanin, I. A. Khramtsov, T. Rendler, I. D. Booker, J. Ul Hassan, N. Morioka, Y.-C. Chen, I. G. Ivanov, N. T. Son, T. Ohshima, M. Bockstedte, A. Gali, C. Bonato, S.-Y. Lee, and J. Wrachtrup. Electrical charge state manipulation of single silicon vacancies in a silicon carbide quantum optoelectronic device. *Nano Letters*, 19:7173–7180, 2019.

¹³M. Rühl, L. Bergmann, M. Krieger, and H. B. Weber. Stark tuning of the silicon vacancy in silicon carbide. *Nano Letters*, 20:658–663, 2020.

¹⁴G. C. Vásquez, M. E. Bathen, A. Galeckas, C. Baziotti, K. M. Johansen, D. Maestre, A. Cremades, Ø. Prytz, A. M. Moe, A. Yu. Kuznetsov, and L. Vines. Strain modulation of Si vacancy emission from SiC micro- and nanoparticles. *Nano Letters*, 20:8689–8695, 2020.

¹⁵D. O. Bracher, X. Zhang, and E. L. Hu. Selective purcell enhancement of two closely linked zero-phonon transition of a silicon carbide color center. *Proc. Natl. Acad. Sci. U.S.A.*, 114:4060, 2017.

¹⁶D. M. Lukin, C. Dory, M. A. Guidry, K. Y. Yang, S. D. Mishra, R. Trivedi, M. Radulaski, S. Sun, D. Vercruyse, G. H. Ahn, and J. Vucković. 4H-silicon-carbide-on-insulator for integrated quantum and nonlinear photonics. *Nature Photonics*, 14:330–334, 2020.

¹⁷Péter Udvarhelyi, Gergő Thiering, Naoya Morioka, Charles Babin, Florian Kaiser, Daniil Lukin, Takeshi Ohshima, Jawad Ul-Hassan, Nguyen Tien Son, Jelena Vučković, et al. Vibronic states and their effect on the temperature and strain dependence of silicon-vacancy qubits in 4 h-si c. *Physical Review Applied*, 13(5):054017, 2020.

¹⁸Di Liu, Florian Kaiser, Vladislav Bushmakin, Erik Hesselmeier, Timo Steidl, Takeshi Ohshima, Nguyen Tien Son, Jawad Ul-Hassan, Öney O. Soyal, and Jörg Wrachtrup. The silicon vacancy centers in sic: determination of intrinsic spin dynamics for integrated quantum photonics. *npj Quantum Information*, 10(1):72, 2024.

¹⁹Wenzheng Dong, MW Doherty, and Sophia E Economou. Spin polarization through intersystem crossing in the silicon vacancy of silicon carbide. *Physical Review B*, 99(18):184102, 2019.

²⁰Ali Tayefeh Younesi and Ronald Ulbricht. Broadband transient absorption spectroscopy using an incoherent white-light source as probe. *Opt. Express*, 30(21):38896–38906, Oct 2022.

²¹Minh Tuan Luu, Ali Tayefeh Younesi, and Ronald Ulbricht. Nitrogen-vacancy centers in diamond: discovery of additional electronic states. *Materials for Quantum Technology*, 4(3):035201, jul 2024.

²²Minh Tuan Luu, Christopher Linderälv, Zsolt Benedek, Ádám Gányecz, Gergely Barcza, Viktor Ivády, and Ronald Ulbricht. Identifying high-energy electronic states of nv- centers in diamond. *Applied Physics Letters*, 126(23):234001, 06 2025.

²³Ronald Ulbricht and Zhi-Heng Loh. Excited-state lifetime of the NV- infrared transition in diamond. *Physical Review B*, 98(9):094309, 2018.

²⁴Satoru Sugano, Yukito Tanabe, and Hiroshi Kamimura. *Multiplets of Transition-Metal Ions in Crystals*. Number v. 33 in *Pure and Applied Physics*. Academic Press, New York, 1970.

²⁵M. Bockstedte, F. Schütz, T. Garratt, V. Ivády, and A. Gali. Ab initio description of highly correlated states in defects for realizing quantum bits. *npj Quantum Materials*, 3:31, 2018.

²⁶Lukas Muechler, Danis I. Badrtdinov, Alexander Hampel, Jennifer Cano, Malte Rösner, and Cyrus E. Dreyer. Quantum embedding methods for correlated excited states of point defects: Case studies and challenges. *Phys. Rev. B*, 105:235104, Jun 2022.

²⁷He Ma, Nan Sheng, Marco Govoni, and Giulia Galli. Quantum embedding theory for strongly correlated states in materials. *Journal of Chemical Theory and Computation*, 17(4):2116–2125, 2021. PMID: 33739106.

²⁸Siyuan Chen, Victor Wen-zhe Yu, Yu Jin, Marco Govoni, and Giulia Galli. Advances in quantum defect embedding theory. *Journal of Chemical Theory and Computation*, 21(16):7797–7812, 2025. PMID: 40802497.

²⁹Ronald Ulbricht, Shuo Dong, I-Ya Chang, Bala Murali Krishna Mariserla, Keshav M. Dani, Kim Hyeon-Deuk, and Zhi-Heng Loh. Jahn-Teller-induced femtosecond electronic depolarization dynamics of the nitrogen-vacancy defect in diamond. *Nature Communications*, 7(1):13510, November 2016.

³⁰V. M. Acosta, E. Bauch, A. Jarmola, L. J. Zipp, M. P. Ledbetter, and D. Budker. Broadband magnetometry by infrared-absorption detection of nitrogen-vacancy ensembles in diamond. *Applied Physics Letters*, 97(17):174104, 2010.

³¹Ali Tayefeh Younesi, Muhib Omar, Arne Wickenbrock, Dmitry Budker, and Ronald Ulbricht. Towards high-sensitivity magnetometry with nitrogen-vacancy centers in diamond using the singlet infrared absorption. *Phys. Rev. Appl.*, 23:054019, May 2025.

³²I. Meirzada, S. A. Wolf, A. Naiman, U. Levy, and N. Bar-Gill. Enhanced spin state readout of nitrogen-vacancy centers in diamond using infrared fluorescence. *Phys. Rev. B*, 100:125436, Sep 2019.

³³Matthias Niethammer, Matthias Widmann, Torsten Rendler, Naoya Morioka, Yu-Chen Chen, Rainer Stöhr, Jawad Ul Hassan, Shinobu Onoda, Takeshi Ohshima, Sang-Yun Lee, Amlan Mukherjee, Junichi Issoya, Nguyen Tien Son, and Jörg Wrachtrup. Coherent electrical readout of defect spins in silicon carbide by photo-ionization at ambient conditions. *Nature Communications*, 10(1):5569, December 2019.

³⁴Tetsuri Nishikawa, Naoya Morioka, Hiroshi Abe, Koichi Murata, Kazuki Okajima, Takeshi Ohshima, Hidekazu Tsuchida, and Norikazu Mizuuchi. Coherent photoelectrical readout of single spins in silicon carbide at room temperature. *Nature Communications*, 16(1):3405, April 2025.

³⁵T. Clua-Provost, Z. Mu, A. Durand, C. Schrader, J. Happacher, J. Bocquel, P. Maletinsky, J. Fraunié, X. Marie, C. Robert, G. Seine, E. Janzen, J. H. Edgar, B. Gil, G. Cassabois, and V. Jacques. Spin-dependent photodynamics of boron-vacancy centers in hexagonal boron nitride. *Phys. Rev. B*, 110:014104, Jul 2024.

³⁶Hannah L. Stern, Qiushi Gu, John Jarman, Simone Eizagirre Barker, Noah Mendelson, Dipankar Chugh, Sam Schott, Hoe H. Tan, Henning Sirringhaus, Igor Aharonovich, and Mete Atatüre. Room-temperature optically detected magnetic resonance of single defects in hexagonal boron nitride. *Nature Communications*, 13(1):618, February 2022.

³⁷James W. Furness, Aaron D. Kaplan, Jinliang Ning, John P. Perdew, and Jianwei Sun. Accurate and numerically efficient r2SCAN meta-generalized gradient approximation. *The journal of physical chemistry letters*, 11(19):8208–8215, 2020.

³⁸Lukas Razinkovas, Marcus W. Doherty, Neil B. Manson, Chris G. Van de Walle, and Audrius Alkauskas. Vibrational and vibronic structure of isolated point defects: The nitrogen-vacancy center in diamond. *Physical Review B*, 104:045303, 2021.

³⁹Vytautas Žalandauskas, Rokas Silkinis, Lasse Vines, Lukas Razinkovas, and Marianne Etzelmüller Bathen. Theory of the divacancy in 4H-SiC: impact of Jahn-Teller effect on optical properties. *npj Computational Materials*, 11(1):155, 2025.

⁴⁰Kun Huang and Avril Rhys. Theory of light absorption and non-radiative transitions in f-centres. *Proc. R. Soc. Lond. A*, 204:406–423, 1950.

⁴¹Audrius Alkauskas, Bob B. Buckley, David D. Awschalom, and Chris G. Van de Walle. First-principles theory of the luminescence lineshape for the triplet transition in diamond nv centres. *New Journal of Physics*, 16(7):073026, 2014.

⁴²Melvin Lax. The Franck-Condon Principle and Its Application to Crystals. *The Journal of Chemical Physics*, 20(11):1752–1760, November 1952.

⁴³Ryogo Kubo and Yutaka Toyozawa. Application of the Method of Generating Function to Radiative and Non-Radiative Transitions of a Trapped Electron in a Crystal. *Progress of Theoretical Physics*, 13(2):160–182, February 1955.

⁴⁴G. Kresse and J. Furthmüller. Efficiency of ab-initio total energy calculations for metals and semiconductors using a plane-wave basis set. *Computational Materials Science*, 6(1):15–50, Jul 1996.

⁴⁵G. Kresse and J. Hafner. Ab initio molecular dynamics for liquid metals. *Physical Review B*, 47(1):558–561, Jan 1993.

⁴⁶G. Kresse and J. Hafner. Ab initio molecular-dynamics simulation of the liquid-metal–amorphous–semiconductor transition in germanium. *Physical Review B*, 49(20):14251–14269, May 1994.

⁴⁷P. E. Blöchl. Projector augmented-wave method. *Physical Review B*, 50(24):17953–17979, dec 1994.

⁴⁸G. Kresse and J. Furthmüller. Efficient iterative schemes for ab initio total-energy calculations using a plane-wave basis set. *Physical Review B*, 54(16):11169–11186, oct 1996.

⁴⁹Ghulam Abbas, Oscar Buhacea-Lindvall, Joel Davidsson, Rickard Armiento, and Igor A Abrikosov. Theoretical characterization of NV-like defects in 4H-SiC using ADAQ with SCAN and r2SCAN meta-GGA functionals. *Applied Physics Letters*, 126(15), 2025.

⁵⁰Atsushi Togo and Isao Tanaka. First principles phonon calculations in materials science. *Scripta Materialia*, 108:1–5, 2015.

⁵¹Jordan J. Markham. Interaction of normal modes with electron traps. *Rev. Mod. Phys.*, 31(4):956–989, 1959.

⁵²J. E. Lowther and J. A. van Wyk. Strongly perturbed negative-vacancy-related centers in diamond. *Phys. Rev. B*, 49:11010–11015, Apr 1994.

⁵³P. Udvarhelyi, G. Thiering, N. Morioka, C. Babin, F. Kaiser, D. Lukin, T. Ohshima, J. Ul Hassan, N. T. Son, J. Vucković, J. Wrachtrup, and A. Gali. Vibronic states and their effect on the temperature and strain dependence of silicon-vacancy qubits in 4H-SiC. *Physical Review Applied*, 13:054017, 2020.

⁵⁴J. P. Elliott and P. G. Dawber. *Symmetry in Physics Vol1*. Macmillan Education UK, London, 1979.

⁵⁵R. Matthias Geilhufe and Wolfram Hergert. GTPack: A Mathematica Group Theory Package for Application in Solid-State Physics and Photonics. *Frontiers in Physics*, 6:86, 2018.

⁵⁶Wolfram Hergert and R. Matthias Geilhufe. *Group Theory in Solid State Physics and Photonics: Problem Solving with Mathematica*. Wiley-VCH, 2018. ISBN: 978-3-527-41133-7.

⁵⁷Arsalan Hashemi, Christopher Linderälvd, Arkady V Krasheninnikov, Tapio Ala-Nissila, Paul Erhart, and Hannu-Pekka Komsa. Photoluminescence line shapes for color centers in silicon carbide from density functional theory calculations. *Physical Review B*, 103(12):125203, 2021.

⁵⁸M. W. Doherty, V. M. Acosta, A. Jarmola, M. S. J. Barson, N. B. Manson, D. Budker, and L. C. L. Hollenberg. Temperature shifts of the resonances of the nv^- center in diamond. *Phys. Rev. B*, 90:041201, Jul 2014.

⁵⁹John P. Perdew, Kieron Burke, and Matthias Ernzerhof. Generalized gradient approximation made simple. *Physical Review Letters*, 77(18):3865–3868, oct 1996.

⁶⁰Jochen Heyd, Gustavo E. Scuseria, and Matthias Ernzerhof. Hybrid functionals based on a screened coulomb potential. *The Journal of Chemical Physics*, 118(18):8207–8215, may 2003.

Acknowledgments

RU acknowledges funding by the Max-Planck Society. MEB, CL and LR acknowledge financial support that was kindly provided by the Research Council of Norway and the University of Oslo through the frontier research projects QuTe (no. 325573, FriPro ToppForsk-program) and TASQ (no. 354419, FriPro). NTS acknowledges fundings from the European Union under Horizon Europe for the projects QuS-PARC (no. 10118689), QRC-4-ESP (no. 101129663) and QUEST (no. 101156088), the Knut and Alice Wallenberg Foundation (KAW 2018.0071), the Vinnova (no. 2024-00461 and no. 2025-03848). Some of the computations were performed on resources provided by UNINETT Sigma2 — the National Infrastructure for High Performance Computing and Data Storage in Norway, supercomputer GALAX of the Center for Physical Sciences and Technology, Lithuania, and the High Performance Computing Center “HPC Saulėtekis” in the Faculty of Physics, Vilnius University. GT was supported by the János Bolyai Research Scholarship of the Hungarian Academy of Sciences and acknowledges the funding from the Hungarian National Research, Development and Innovation Office (NKFIH) under the NKKP STARTING grant (no. 150113).

Author contributions

RU initiated and supervised the project. ATY and MTL performed the experiments and analyzed the data. VŽ, LR and MEB performed the lineshape calculations. CL performed the quantum embedding calculations. GT and LR worked on the group theory. NTS provided the SiC sample. TO performed the electron irradiation. All authors participated in writing the manuscript.

Competing interests

The authors declare no competing interests.

Supplementary Information Contents

Experimental Methods	13
S1. Measurement setup	13
S2. Oblique Incidence Probe Configuration	14
S3. Scanning Excitation Transient Absorption	14
S4. Materials	15
 Theoretical methods	16
S5. DFT calculations	16
S6. Electron-phonon coupling	16
S7. Force-constant embedding methodology	17
S8. Simple model for non-adiabatic broadening	18
S9. Quantum embedding for electronic structure	20
S10. Electronic states and crystal-field splitting: group theory analysis	20
S10.1. Symmetry-adapted many-body wavefunctions.	20
S10.2. Crystal-field Hamiltonian and symmetry lowering for the quartet excited state.	21
S10.3. Quenching of crystal-field splitting in the doublet manifolds	22
S11. Crystal-field splitting by means of multi-configurational corrections from quantum embedding	23
S11.1. Excited symmetry-adapted three-hole wavefunctions	23
S11.2. First order multi-configurational crystal field corrections for $ ^2T_1\rangle$ and $ ^2T_2\rangle$	24
S11.3. Second order corrections	25
S12. Optical selection rules for spin doublets	26
 Supplemental results and discussion	28
S13. Transient Absorption Spectroscopy Results	28
S14. Photoexcitation dynamics of h-site vacancy V_h	29
S15. Photoexcitation dynamics of k-site vacancy V_k	30
S16. V2' PSB characterization and analysis	33
S17. Polarization dependence of the spin-doublet transitions	36
S18. Temperature dependence of spin-doublet transitions	37
S19. ZPL characteristics of the spin-doublet and spin-quartet transitions	38
S20. Calculated emission and absorption spectra of V_{Si}^-	40
S21. Quantum embedding results	41

Experimental methods

S1 Measurement setup

A more detailed description of the employed transient absorption (TA) spectroscopy setups has been previously published^{20,21}. Here, we present the essential information explaining the setups, including the specific parameters used in this study.

Two TA setups are employed: one spanning the femto- to nano-second (fs-ns) range, and the other spanning the nano- to micro-second (ns- μ s) range. In both methods, a fiber laser (Amplitude Tangerine SP) with a repetition rate at typically 2 kHz is employed as the main output source. Although the repetition rate can reach up to 40 MHz for this laser, the chosen value is appropriate to allow the measured defects to return to the initial state after pumping, as well as compatibility with the optical parametric oscillator (OPO) laser system, whose repetition rate is locked to 1 kHz. The output of the fiber laser is about 175 μ J with a pulse duration of \sim 150 fs, which is then distributed to a non-collinear optical amplifier (NOPA, AG Riedle NOPA Rainbow) and a home-built OPA. The spectral output of the NOPA spans in the 390–1300 nm range, although it is mostly operating in the 620–900 nm range for the measurements presented in this paper. In this spectral range, the output pulse energy is about 2–4 μ J depending on the wavelength. The output is employed as the pump in several experiments. As for the OPA, the output spectral range is 660–2100 nm. The extension to the near IR is due to the collinear geometry allowing the idler to be used as an output.

In order to perform the TA measurements, either the output the NOPA or the output of a tunable OPO laser (Ekspla NT242) was utilized as the pump. The NOPA output has a pulse duration of about 150 fs (inheriting from the fiber laser) and thus suitable for studying fast population dynamics. However, the broad linewidth (at least \sim 5 nm/10 meV) of the output means that resonant excitation of the ZPLs may not be efficient. The main use of the NOPA output here is to cover the excitation around 700–750 nm (1.55–1.65 eV) in non-resonant pumping experiments, since the OPO laser power output is inefficient in this spectral range. In contrast, the OPO laser has a pulse duration of approximately 4 ns and a linewidth of sub-0.5 nm (<0.4 meV) in the interested spectral range. The narrow optical bandwidth of the ns-OPO enables superior spectrally selective pumping, enabling precise resonant excitation of specific ZPLs and hence the straightforward distinction of the features associated with h- and k-site vacancies (V_h and V_k , respectively).

For the fs-ns TA setup, the probe beam is the idler output of the OPA at about 1170 nm focused onto a 4 mm-thick c-cut sapphire crystal to generate a broadband pulse spanning between the 500–1300 nm spectral region. The probe beam is then recollimated and subsequently focused on to the sample with a diameter of about 60 μ m to be completely filled by the pump beam. Exiting the sample, the probe is then imaged onto a line camera (Teledyne e2v Octoplus for < 1100 nm and Xenics Manx for 950 – 1600 nm). The spectral resolution is determined by the groove density of the grating used to image the probe onto each pixel of the line camera. In our case, this resolution is about 0.25 nm per pixel, which is roughly 0.3–0.6 meV in the spectral range where this setup is employed. Due to the detection limit of this setup towards the IR, the D^1 transitions can not be observed.

In the case of the ns- μ s TA setup, a continuous wave (CW) incoherent broadband WL source (XWS-30, ISTEQ BV) is used as the probe instead. This method allows observation of TA spectra in the μ s range as it is only limited by the repetition rate of the pump pulses. This WL source produces a spectrum in the range of 400–2000 nm (0.6–3.1 eV) and thus covers most electronic transitions relevant to the discussion. After interacting with the sample, this probe beam passes through a monochromator and is then detected with a photodiode (PD). The process is repeated for each wavelength until the desired spectral range is covered. The spectral resolution is limited primarily by the slit width of the monochromator, and thus is sometimes a trade-off between spectral resolution and signal-to-noise ratio. Generally, this resolution is sub-2 meV in most of the interested spectral regions, although further into the IR region (> 1700 nm – < 0.73 eV), where the D^1 transitions are observed, the slit width is increased and thus the resolution may be higher than the aforementioned value. The setup can also be used to measure time-resolved PL by blocking the WL and simply recording the emission.

All measurements performed in this paper are conducted at 5 K in a closed-cycle helium cryostat (Advanced Research Systems ARS-10HW), unless stated otherwise.

S2 Oblique Incidence Probe Configuration

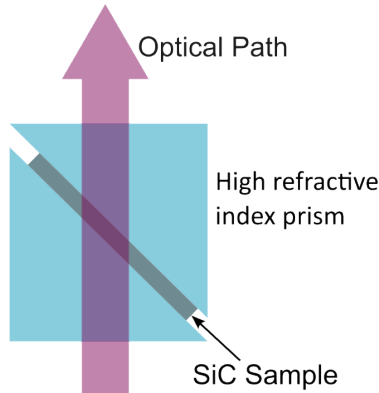


Figure S1. Schematic of the sample sandwiched between two high refractive index rutile prisms and optical path.

As illustrated in Figure 1d, we can infer the coupling of the polarization vector of the probe with the transition dipoles as follows:

- Oblique incidence case: 0°-polarization couples to the μ_x and μ_z dipoles; 90°-polarization couples to the μ_y dipole.
- Normal incidence case: 0°-polarization couples to the μ_x dipole; 90°-polarization couples to the μ_y dipole.

Under the C_{3v} point group, the transition dipole moments transform as either (x, y) (E) or z (A_1) in Cartesian coordinates. For example, optical transitions between electronic states $A_2 \leftrightarrow A_2$ (whose direct product transforms as A_1) are allowed by z dipoles, while the $A_2 \leftrightarrow E$ transition (direct product transforms as E) is allowed with x, y dipoles¹⁷. A more complete description of selection rules is detailed in S12 below.

For the oblique incidence case, we can summarize this experimental scheme with a few useful statements:

- 0°-polarization probe can observe all transitions in either V_h or V_k configuration.
- 90°-polarization probe only couples to the μ_y dipole, thus any transition allowed by μ_z cannot be observed by the probe pulse.

To achieve oblique incidence, a c-cut 4H-SiC sample was placed at an angle of 45° with the incident beam. However, due to the considerable refractive index mismatch between the SiC sample and vacuum (approximately 2.7 and 1, respectively), the beam enters the sample at a much smaller angle (~15°), therefore barely probing the μ_z component. To resolve this issue, the sample was positioned between two high refractive index rutile right-angle prisms, thereby ensuring the beam passed with minimal refraction (see Fig. S1 for a schematic representation of the sample configuration). Although passing the laser pulses through the prisms chirps the pulses to a few ps and limits the temporal resolution, all the population dynamics observed in this study are in the ns range.

S3 Scanning Excitation Transient Absorption

The narrow linewidth of the EKSPLA NT242 OPO is utilized to scan the pump excitation wavelength on the SiC samples at every 1 nm, then a TA measurement is carried out at each excitation wavelength. We call this method scanning excitation TA (SETA).

The timing of the OPO laser (pump) pulse and the fiber laser (probe) pulse needs to be synchronized and thus requires an interlock scheme that can also generate an electronically delayed signal. This is achieved by using a frequency-divided signal of the internal clock of the fiber laser at 10 MHz, before using this signal to serve as an external clock for a set of function generators. The function generators produce a pulse train at 1 kHz, whose delay is adjustable with minimum increments of 5 ns, relative to the fiber laser pulse. This pulse train is then used to trigger the OPO laser, producing output at 1 kHz repetition rate and synchronized to the fiber laser. The pulse sequence and synchronization schemes are illustrated in Fig. S2.

The OPO laser output beam passes through a variable neutral density filter to allow control of the pulse energy of the pump pulse. It is then coupled to a 5 m-long multimode fiber by a spherical mirror with a focal length of 200 mm. The output from the fiber is then collimated before being focused onto the sample using an achromatic lens with anti-reflective coating in the VIS-NIR region (400-1100 nm) with a focal length of +75 mm. The spot size of the pump pulse at the sample is approximately 200 μm in diameter. The energy output of the OPO laser at each wavelength is measured with a power meter, and is later used to normalize the obtained TA spectra to the photon flux arriving at the sample.

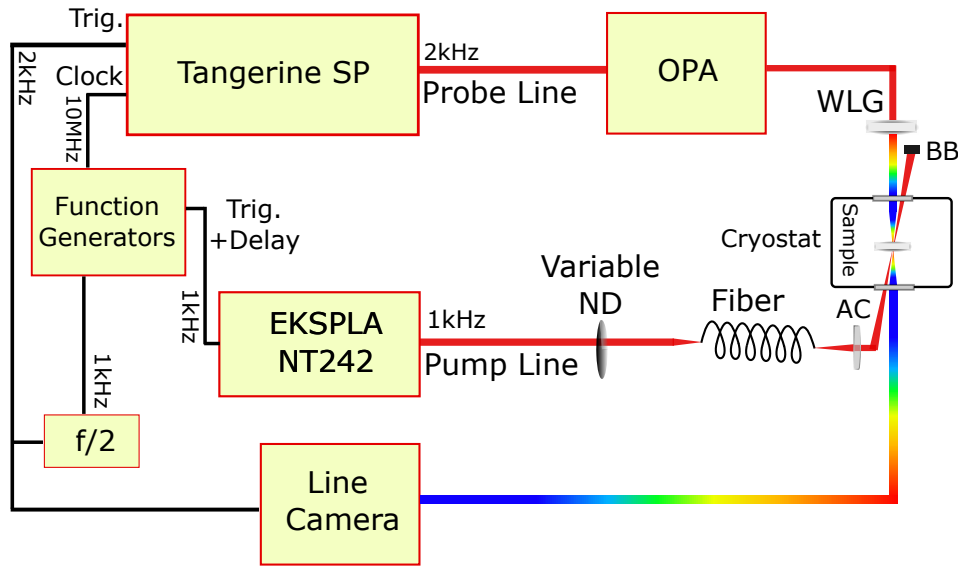


Figure S2. Schematics of the SETA setup including the interlock scheme between the fiber laser (Tangerine SP) and the OPO laser (EKSPLA NT242).

This method outputs a two-dimensional dataset of the TA spectrum at each excitation wavelength, as shown in Fig. S4. The spectra obtained were measured at about 4 ns pump-probe delay. This delay time was chosen such that the probe pulse would arrive after the temporally-broad pump pulse from the OPO laser, yet early enough to observe population in the excited quartet states of the SiC samples as SE.

S4 Materials

We used a high-purity semi-insulating (HPSI) 4H-SiC sample that was irradiated by 2-MeV electrons at room temperature to a fluence of $8 \times 10^{18} \text{ cm}^{-2}$ at room temperature. The samples were cut from a top of a boule and the top layer is curved with original as-grown surface (the (0001) plane).

Theoretical methods

S5 DFT calculations

Vibrational properties of the V_{Si}^- defects in 4H-SiC were computed using density functional theory (DFT) within the Kohn–Sham formalism. All calculations were performed using the Vienna *ab initio* Simulation Package (VASP)^{44–46}. Core and valence electrons were treated using the projector augmented-wave (PAW) method^{47,48} and a plane-wave basis set, respectively. The meta-GGA functional $r^2\text{SCAN}$ ³⁷ was employed, owing to its demonstrated accuracy in describing the structural and electronic properties of point defects in 4H-SiC^{39,49}.

Hexagonal 4H-SiC supercells containing 576 atoms were constructed by repeating the primitive cell $6 \times 6 \times 2$ times along the crystallographic axes. The Brillouin zone was sampled at the Γ point, and a plane-wave cutoff energy of 600 eV was employed. The electronic self-consistent field (SCF) cycle and atomic forces were converged to within 10^{-8} eV and 0.005 eV Å⁻¹, respectively. Point defects were introduced by removing a silicon atom from the lattice to create a silicon vacancy (V_{Si}^-). All calculations were performed for the negative charge state of the vacancy, V_{Si}^- , which corresponds to the only known optically bright states of this defect center.

Phonon modes of 4H-SiC supercells containing V_{Si}^- defects were computed using the finite-displacement method, with the displaced atomic configurations generated by the PHONOPY package⁵⁰. A displacement amplitude of 0.01 Å from the equilibrium geometry was used.

S6 Electron-phonon coupling

Within the Franck–Condon approximation, the normalized luminescence and absorption lineshapes at absolute zero temperature ($T = 0$ K) are given by³⁸:

$$L(\hbar\omega) = C\omega^\kappa A(\hbar\omega), \quad (\text{S1})$$

where C denotes a normalization constant, $A(\hbar\omega)$ denotes the spectral function of electron–phonon coupling, and the exponent κ is equal to 3 for luminescence and 1 for absorption. The spectral function is then defined by the equation

$$A(\hbar\omega) = \sum_m |\langle \chi_{i;0} | \chi_{f;m} \rangle|^2 \delta(E_{\text{ZPL}} \mp (\varepsilon_{fm} - \varepsilon_{f0}) - \hbar\omega), \quad (\text{S2})$$

where E_{ZPL} denotes the zero-phonon line (ZPL) energy, and $\chi_{i;0}$ and $\chi_{f;m}$ are the vibrational wave functions of the initial and final electronic states, respectively. The quantity ε_{fm} corresponds to the energy of the m -th vibrational level in the final electronic manifold, measured relative to the minimum of the potential energy surface. The sign in the argument of the δ function distinguishes luminescence (minus sign) from absorption (plus sign) processes. The optical spectral function $A(\hbar\omega)$ describes the vibrational transition amplitudes and plays a crucial role in determining the lineshape.

Owing to the intrinsic differences between the vibrational structures of the ground and excited electronic states, the overlap integrals $\langle \chi_{i;0} | \chi_{f;m} \rangle$ appearing in Eq. (S2) are inherently multidimensional. A direct evaluation of these integrals in defect systems with numerous vibrational modes becomes computationally challenging. To overcome this limitation we employ equal-mode approximation, which assumes identical vibrational mode shapes and frequencies in the initial and final electronic states^{38,51}. The spectral function $A(\hbar\omega)$ can be obtained in the time domain using the generating function approach introduced by Kubo and Lax^{42,43}. Within this approach, $A(\hbar\omega)$ is derived from the generating function $G(t)$ as:

$$A(\hbar\omega) = \frac{1}{2\pi} \int_{-\infty}^{\infty} G(t) e^{-\gamma|t|} e^{-i(E_{\text{ZPL}}/\hbar - \omega)t} dt, \quad (\text{S3})$$

where the $e^{-\gamma|t|}$ term is introduced to phenomenologically account for homogeneous Lorentzian broadening of the ZPL not captured by the present theoretical framework, while also effectively incorporating inhomogeneous broadening effects. The broadening parameter γ is chosen to reproduce the experimentally observed ZPL linewidth and is set to $\gamma = 0.30$ meV in all calculations. Within the equal-mode approximation, the generating function $G(t)$ takes the form

$$G(t) = \exp \left[-S_{\text{tot}} + \sum_k S_k e^{\pm i\omega_k t} \right], \quad (\text{S4})$$

where the plus (minus) sign corresponds to luminescence (absorption), S_k denotes the partial Huang–Rhys (HR) factor, and the summation runs over all vibrational modes in the system. The total electron–phonon coupling strength is defined as $S_{\text{tot}} = \sum_k S_k$. The partial HR factor S_k quantifies the average number of phonons excited during an optical transition⁴⁰ and is given by

$$S_k = \frac{\omega_k \Delta Q_k^2}{2\hbar}. \quad (\text{S5})$$

Here, ΔQ_k represents the ionic displacement along the k -th normal mode induced by the optical transition. More explicitly, ΔQ_k is defined as the projection of the mass-weighted displacement between the ground- and excited-state equilibrium configurations onto the normalized phonon eigenvector η_k :

$$\Delta Q_k = \sum_{m\alpha} \sqrt{M_m} \Delta R_{m\alpha} \eta_{k;m\alpha}. \quad (\text{S6})$$

In this expression, $\Delta R_{m\alpha}$ denotes the displacement of atom m along the Cartesian direction α , and M_m is the corresponding atomic mass.

To describe the generating function in Eq. (S4) for extended systems, there is a need to account for a continuum of vibrational frequencies. We introduce the spectral density of the electron–phonon coupling (also referred to as the spectral function of electron–phonon coupling):

$$S(\hbar\omega) \equiv \sum_k S_k \delta(\hbar\omega_k - \hbar\omega). \quad (\text{S7})$$

With this definition the generating function can be recast in the integral form

$$G(t) = \exp \left[-S_{\text{tot}} + \int S(\hbar\omega) e^{\pm i\omega t} d\omega \right]. \quad (\text{S8})$$

The Dirac δ -functions in Eq. (S7) are approximated using Gaussian functions, yielding a smooth representation of the spectral function of electron–phonon coupling. The Gaussian widths σ are chosen to decrease gradually from 1.5 meV at zero frequency to 0.5 meV at the maximum phonon frequency.

Within the supercell approach, a particular challenge arises when trying to determine the relaxation profile after an optical transition. The finite size of the supercell in direct DFT calculations limits the long-wavelength components of $\Delta R_{m\alpha}$ in Eq. (S6). To capture the relaxation profile in the dilute limit, we compute ΔQ_k for each vibrational mode of a large supercell constructed using the force-constant embedding methodology (described in the following subsection). This approach exploits the linear relation between forces and atomic displacements within the harmonic approximation. The relaxation component ΔQ_k is then obtained as follows:

$$\Delta Q_k = \frac{1}{\omega_k^2} \sum_{m\alpha} \frac{F_{m\alpha}}{\sqrt{M_m}} \eta_{k;m\alpha}, \quad (\text{S9})$$

where $F_{m\alpha}$ is the force acting on atom m along direction α when the system is in the final electronic state, but maintains the equilibrium geometry of the initial state, as calculated in the directly accessible supercell. $\eta_{k;m\alpha}$ denotes the vibrational mode shape obtained from the embedded supercell. By using forces that already converged in the computationally tractable supercell, this approach, combined with the embedding methodology, captures electron–phonon coupling for low-frequency modes (and subsequently vibrational resonances) and provides an accurate description of optical lineshapes.

In our calculations, the vibrational mode frequencies are in very good agreement with experimental data. However, when employing the r^2 SCAN functional, we observe a systematic underestimation of atomic relaxations. We assume that the overall shape of the calculated spectral densities $S(\hbar\omega)$ closely reflects the peak positions and the general description of the vibrational structure. To compensate for the underestimated atomic relaxations, we therefore apply a linear scaling factor $\zeta = 1.25$, such that $S'(\hbar\omega) = \zeta S(\hbar\omega)$ is used in all lineshape calculations.

S7 Force-constant embedding methodology

The force-constant embedding methodology described in Refs. 38 and 41 was employed to model the vibrational properties of large defect-containing supercells. This approach exploits the short-range nature of interatomic forces in semiconductors to construct an effective Hessian matrix for systems comprising thousands of atoms. In this framework, Hessian matrix elements are assigned based on the relative positions of the atoms: for pairs lying within a specified bulk cutoff radius r_b , the corresponding elements are taken from the bulk supercell Hessian; for atom pairs located within a cutoff radius r_d of the defect, the elements are taken from the defect-containing supercell; in all remaining cases, the matrix elements are set to zero.

The bulk 4H-SiC supercell had dimensions of $8 \times 8 \times 3$, comprising 1536 atomic sites, whereas the defect-containing supercell had dimensions of $6 \times 6 \times 2$ and contained 576 atomic sites. The cutoff radius for the bulk system was $r_b = 12.200 \text{ \AA}$, while the defect cutoff radius was $r_d = 9.228 \text{ \AA}$. The Hessian matrix was constructed using a $25 \times 25 \times 8$ supercell comprising approximately 40 000 atomic sites. By employing the embedding methodology to mitigate finite-size effects, the vibrational basis is expanded from 1 722 modes in the $6 \times 6 \times 2$ defect supercell to a total of 119 994 vibrational modes, corresponding to an increase by a factor of approximately ~ 70 . This substantial enlargement of the vibrational space enables the use of smaller Gaussian smoothing widths σ , thereby significantly improving the spectral resolution. Such enhanced resolution is essential for resolving fine spectral features, such as the splitting of the first phonon sideband peak in the emission lineshape of $\text{V}_{\text{Si}}^-(k)$. Moreover, this methodology grants access to an extensive set of vibrational modes, including low-energy acoustic phonons, and yields a relaxation profile representative of the dilute-defect limit (see Eq. (S9)).

S8 Simple model for non-adiabatic broadening

In this Supplementary Note, we develop a simplified theoretical model describing non-adiabatic broadening of a ZPL arising from electron–phonon coupling between two electronic states. Electronic states are defined as solutions of the electronic Schrödinger equation at fixed ionic coordinates. Within the adiabatic approximation, these states generate potential energy surfaces (PES) governing nuclear motion. When the electronic energy separation becomes comparable to phonon energies, vibrational motion induces non-adiabatic mixing between the states, leading to vibronic broadening of optical transitions. Hartree atomic units are used throughout.

Adiabatic model. The complete electron–ion Hamiltonian is expressed as the sum of the electronic kinetic energy, the ionic kinetic energy, and the total potential energy:

$$H = T_e + T_n + U(\mathbf{r}, \mathbf{Q}) \quad (\text{S10})$$

$$= T_e + T_n + U(\mathbf{r}, \mathbf{Q}_0) + \Delta U(\mathbf{r}, \mathbf{Q}), \quad (\text{S11})$$

where \mathbf{Q} denotes the ionic normal coordinates and \mathbf{Q}_0 their equilibrium configuration. The term $U(\mathbf{r}, \mathbf{Q}_0)$ represents the electronic potential energy with the ions frozen at equilibrium, while $\Delta U(\mathbf{r}, \mathbf{Q})$ accounts for all modifications induced by ionic displacements. The electronic eigenstates $|\psi_i\rangle$ of the frozen-ion Hamiltonian $H_{\text{el}} = T_e + U(\mathbf{r}, \mathbf{Q}_0)$ form a convenient basis for the expansion of the total vibronic wavefunction,

$$\Psi(\mathbf{r}, \mathbf{Q}) = \sum_i \chi_i(\mathbf{Q}) |\psi_i\rangle.$$

Restricting the electronic basis to two electronic states, $|\psi_1\rangle$ and $|\psi_2\rangle$, with energies $\varepsilon_1 = 0$ and $\varepsilon_2 = \Delta$, the adiabatic Hamiltonian is diagonal in the electronic subspace. Under the harmonic approximation, the PES are taken to be identical, $V_{11}(\mathbf{Q}) = V_{22}(\mathbf{Q}) = \sum_k \frac{1}{2} \omega_k^2 Q_k^2$, where $V_{ii} = \langle \psi_i | \Delta U(\mathbf{r}, \mathbf{Q}) | \psi_i \rangle$. The vibrational wavefunctions are phonon Fock states $|n_1, n_2, \dots\rangle$.

Non-adiabatic coupling. Non-adiabatic effects arise from off-diagonal matrix elements of ΔU , which are assumed to be real and symmetric. Expanding the coupling linearly in normal coordinates yields

$$V_{12}(\mathbf{Q}) = \sum_k C_k Q_k = \sum_k K_k \omega_k (a_k^\dagger + a_k), \quad (\text{S12})$$

where K_k are dimensionless vibronic coupling constants. The resulting vibronic Hamiltonian in second-quantized form reads

$$H = \begin{pmatrix} 0 & 0 \\ 0 & \Delta \end{pmatrix} + \sum_k \frac{1}{2} \omega_k \begin{pmatrix} a_k^\dagger a_k + \frac{1}{2} & 0 \\ 0 & a_k^\dagger a_k + \frac{1}{2} \end{pmatrix} + \sum_k K_k \omega_k \begin{pmatrix} 0 & a_k^\dagger + a_k \\ a_k^\dagger + a_k & 0 \end{pmatrix}. \quad (\text{S13})$$

The eigenstates are expanded in a truncated phonon basis with a cutoff on the total number of excited phonons, $\sum_k n_k \leq N_{\text{max}}$. Diagonalization of Eq. (S13) yields vibronic eigenstates of the form

$$|\Psi_l\rangle = \sum_{i=1}^2 \sum_{\substack{n_1, \dots, n_N \\ \sum_k n_k \leq N_{\text{max}}}} c_{i; n_1 \dots n_N}^l |n_1, \dots, n_N\rangle |\psi_i\rangle. \quad (\text{S14})$$

a. Optical lineshape. To calculate the optical lineshape, we consider transitions from an initial adiabatic electronic state in the vibrational ground configuration $|\psi_0\rangle |0 \dots 0\rangle$ to the vibronic eigenstates defined in Eq. (S14). In addition to the non-adiabatic mixing contained in the vibronic eigenstates, further electron–phonon coupling is incorporated through vibrational overlap factors. This allows phonon sidebands to be generated on top of the broadened zero-phonon line and enables direct visualization of changes in the vibronic structure.

The vibrational overlaps are evaluated within the Huang–Rhys formalism for shifted harmonic oscillators, characterized by Huang–Rhys factors $S_i = \lambda_i^2$,

$$\langle \mathbf{n} | \mathbf{0} \rangle \equiv \langle n_1 \dots n_N | 0 \dots 0 \rangle = \prod_{i=1}^N e^{-\lambda_i^2/2} \frac{(-\lambda_i)^{n_i}}{\sqrt{n_i!}}.$$

The absorption lineshape is then given by

$$A(\hbar\omega) = \sum_i \left| \sum_{\mathbf{n}} (c_{1; \mathbf{n}}^i \langle \mathbf{n} | \mathbf{0} \rangle \langle \psi_1 | \mu | \psi_0 \rangle + c_{2; \mathbf{n}}^i \langle \mathbf{n} | \mathbf{0} \rangle \langle \psi_2 | \mu | \psi_0 \rangle) \right|^2 \times \delta(E_{\text{ZPL}} + \varepsilon_0 + \varepsilon_i - \hbar\omega). \quad (\text{S15})$$

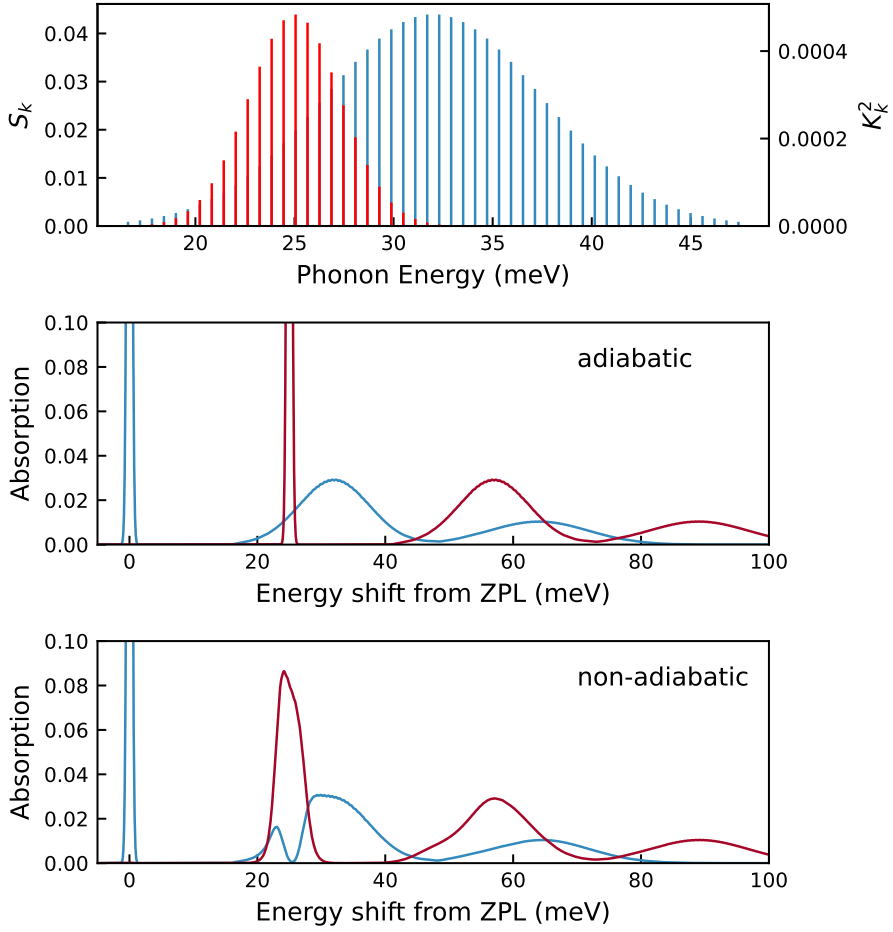


Figure S3. Minimal model for non-adiabatic ZPL broadening. (a) Distributions of Huang–Rhys factors S_k (blue) and non-adiabatic coupling strengths K_k^2 (red) over 52 effective vibrational modes. The parameters are chosen such that $S_{\text{tot}} = \sum_k S_k = 1$ and $K_{\text{tot}}^2 = \sum_k K_k^2 = 0.005$, with non-adiabatic coupling restricted to modes in the vicinity of the second ZPL at 25 meV. (b) Calculated absorption lineshapes for the two optical transitions in the absence of non-adiabatic coupling ($K_{\text{tot}} = 0$), assuming orthogonal polarization directions for transitions involving ψ_1 and ψ_2 . (c) Absorption lineshapes obtained from the full vibronic Hamiltonian including non-adiabatic coupling, illustrating the resulting broadening of the zero-phonon line. The model is intended to capture the mechanism of non-adiabatic ZPL broadening rather than to reproduce the full phonon sideband structure quantitatively.

Because the phonon spectrum is discrete, the energy-conserving delta function is replaced in practice by a Gaussian of finite width σ .

When the optical transitions $\psi_0 \rightarrow \psi_1$ and $\psi_0 \rightarrow \psi_2$ couple to orthogonal optical polarization directions, the polarization-resolved absorption lineshapes are obtained by projecting the dipole operator onto the selected polarization. In Eq. (S15), this is implemented by setting the electronic transition matrix element associated with the non-selected polarization to zero. For example, when evaluating the lineshape for the polarization corresponding to the $\psi_0 \rightarrow \psi_1$ transition, the matrix element $\langle \psi_2 | \mu | \psi_0 \rangle$ is set to zero, and vice versa. This procedure is applied in the numerical calculations presented below.

b. Numerical simulations. The numerical implementation of the model is illustrated in Fig. S3. Figure S3a shows the distributions of the non-adiabatic coupling strengths K_k^2 (red) and Huang–Rhys factors S_k (blue) over 52 vibrational modes. The accumulated Huang–Rhys factor is $S_{\text{tot}} = \sum_k S_k = 1$, while the total non-adiabatic coupling strength is comparatively small, $K_{\text{tot}}^2 = \sum_k K_k^2 = 0.005$. Non-adiabatic coupling is included only for modes in the vicinity of the second zero-phonon line at 25 meV, modeled by a Gaussian distribution centered at 25 meV with a width of $\sigma = 3.3$ meV. In contrast, the Huang–Rhys factors follow a broader Gaussian distribution centered at 32 meV with $\sigma = 5.5$ meV, chosen to approximately reproduce the first experimentally observed phonon sideband peak discussed in the main text.

Figure S3b shows the calculated absorption lineshapes for two orthogonal polarization directions associated with the two optical transitions in the absence of non-adiabatic coupling ($K_{\text{tot}} = 0$), assuming that transitions involving ψ_1 and ψ_2 couple to orthogonal polarizations. Finally, Fig. S3c presents the absorption lineshapes obtained from the full vibronic Hamiltonian. The

phonon basis is truncated by imposing a maximum total number of excited phonons $N_{\max} = 2$.

The dip in the absorption sideband visible in the spectral overlap region in Fig. S3c should not be interpreted as a physical feature expected in experiment. It originates from the restricted set of Jahn–Teller–active modes included in the present model and reflects a redistribution of spectral weight rather than a true suppression of absorption. In an experimental spectrum, this region would be filled by contributions from additional vibrational modes, including those coupled non-adiabatically, leading to a smooth overlap of spectral features. The purpose of the present model is therefore not to reproduce the full phonon sideband in detail, but to demonstrate the mechanism by which non-adiabatic coupling leads to a broadening of the ZPL.

S9 Quantum embedding for electronic structure

Quantum embedding calculations were performed based on constrained random phase approximation (cRPA). In this method an effective Hamiltonian for a subset of states

$$h = - \sum_{ij} t_{ij} c_i^\dagger c_j + \frac{1}{2} \sum_{ijkl} u_{ijkl} c_i^\dagger c_j^\dagger c_l c_k, \quad (\text{S16})$$

is parameterized using a combination of density functional theory and cRPA²⁶. The cRPA calculations were performed using the projector augmented wave method as implemented in VASP.⁴⁴ The parameterized Hamiltonian was then diagonalized using an in house implementation of full configuration interaction. The Hamiltonian was constructed according to the methodology outlined in Ref. 26, including double counting corrections for the mean field Coulomb energy. To recap it briefly, spin polarized DFT is used to obtain the geometry upon which a spin paired calculation is performed. Here, based on the localization of the Bloch states, the activate space is chosen. In the case of the silicon vacancy, the activate space consists of 4 spatial orbitals, corresponding to the dangling bonds. The one-body matrix elements (t) are obtained as the Kohn–Sham eigenenergies of the activate space states. Next, a cRPA calculation is performed to obtain the two-body matrix elements (u) in the active space. The double counting corrections is then computed from the two-body matrix elements²⁶, which are then applied to the one-body matrix elements.

S10 Electronic states and crystal-field splitting: group theory analysis

As discussed in the main text, we describe the electronic structure of the silicon vacancy within the ideal tetrahedral (T_d) symmetry. The relevant many-body configurations are formulated in terms of three holes occupying the defect-centered t_2 and a_1 orbitals. We use the conventional representation found in multiplet-theory literature, in which the three components of the t_2 manifold transform as Cartesian vectors under T_d symmetry operations, i.e., the orbitals t_{2x} , t_{2y} , and t_{2z} transform as the x , y , and z components of a vector in a standardized coordinate system where the threefold (trigonal) rotational axes are oriented along directions equivalent to $x + y + z$. The choice of coordinate system is not aligned with the crystallographic axes of hexagonal SiC; specifically, the $x + y + z$ direction coincides with the crystallographic c -axis and is perpendicular to the basal (c) plane. In this representation, the symmetry-adapted many-body wavefunctions for a t_2^3 and $a_1 t_2^2$ configuration are well established from classical multiplet theory, as summarized, for example, in the monograph by Sugano–Tanabe–Kamimura.²⁴ For completeness and to establish notation, we explicitly list below the symmetry-adapted wavefunctions relevant for the quartet and doublet manifolds.

S10.1 Symmetry-adapted many-body wavefunctions.

Quartet states. For the $S = 3/2$ quartet manifold, the optical ground state is $|^4A_2\rangle$ where three electrons (or equivalently three holes) occupy the t_2 orbital and transforms according to the A_2 irreducible representation. The wavefunctions of all four spin projections $m_s = \{\pm \frac{3}{2}, \pm \frac{1}{2}\}$ can be written as:

$$|^4A_2\rangle = \begin{cases} m_s = +3/2, & |t_{2x}t_{2y}t_{2z}\rangle \\ m_s = +1/2, & (|t_{2x}t_{2y}\bar{t}_{2z}\rangle + |t_{2x}\bar{t}_{2y}t_{2z}\rangle + |t_{2x}t_{2y}\bar{t}_{2z}\rangle)/\sqrt{3} \\ m_s = -1/2, & (|\bar{t}_{2x}\bar{t}_{2y}t_{2z}\rangle + |\bar{t}_{2x}t_{2y}\bar{t}_{2z}\rangle + |\bar{t}_{2x}\bar{t}_{2y}\bar{t}_{2z}\rangle)/\sqrt{3} \\ m_s = -3/2, & |\bar{t}_{2x}\bar{t}_{2y}\bar{t}_{2z}\rangle \end{cases} = \begin{aligned} &= \frac{1}{\sqrt{6}} \begin{vmatrix} t_{2x}^\uparrow(\vec{x}_1) & t_{2y}^\uparrow(\vec{x}_1) & t_{2z}^\uparrow(\vec{x}_1) \\ t_{2x}^\uparrow(\vec{x}_2) & t_{2y}^\uparrow(\vec{x}_2) & t_{2z}^\uparrow(\vec{x}_2) \\ t_{2x}^\uparrow(\vec{x}_3) & t_{2y}^\uparrow(\vec{x}_3) & t_{2z}^\uparrow(\vec{x}_3) \end{vmatrix}, \\ &= \frac{1}{\sqrt{6}} \begin{vmatrix} t_{2x}^\downarrow(\vec{x}_1) & t_{2y}^\downarrow(\vec{x}_1) & t_{2z}^\downarrow(\vec{x}_1) \\ t_{2x}^\downarrow(\vec{x}_2) & t_{2y}^\downarrow(\vec{x}_2) & t_{2z}^\downarrow(\vec{x}_2) \\ t_{2x}^\downarrow(\vec{x}_3) & t_{2y}^\downarrow(\vec{x}_3) & t_{2z}^\downarrow(\vec{x}_3) \end{vmatrix}, \end{aligned} \quad (\text{S17})$$

where $|\cdots\rangle$ denotes a Slater determinant where \vec{x}_1 , \vec{x}_2 , \vec{x}_3 variables are the coordinates of three particles and we introduce the usual $t_{2\alpha}^\uparrow = t_{2\alpha}$, $t_{2\alpha}^\downarrow = \bar{t}_{2\alpha}$ notation for spin degrees of freedom. From now on for simplicity, we consider only the states exhibiting maximal spin projection $m_s = +\frac{3}{2}$ ($+\frac{1}{2}$) for spin quartets (doublets) unless noted explicitly.

Exciting one electron from a_1 orbital into one of the three t_{2x}, t_{2y}, t_{2z} triply degenerate levels gives rise the $|^4T_1\rangle$ multiplet that transforms as T_1 . The corresponding symmetry-adapted components can be written in electron or hole pictures as follows

$$|^4T_{1i}\rangle = \underbrace{\begin{cases} |\bar{a}_1\bar{t}_{2x}\bar{t}_{2y}\bar{t}_{2z}t_{2x}\rangle, & i = x, \\ |\bar{a}_1\bar{t}_{2x}\bar{t}_{2y}\bar{t}_{2z}t_{2y}\rangle, & i = y, \\ |\bar{a}_1\bar{t}_{2x}\bar{t}_{2y}\bar{t}_{2z}t_{2z}\rangle, & i = z. \end{cases}}_{\text{electron picture}} \iff |^4T_{1i}\rangle = \underbrace{\begin{cases} |a_1t_{2y}t_{2z}\rangle, & i = x, \\ |a_1t_{2z}t_{2x}\rangle, & i = y, \\ |a_1t_{2x}t_{2y}\rangle, & i = z. \end{cases}}_{\text{hole picture}} \quad (\text{S18})$$

where we now also need to depict the occupation of the a_1 orbitals. One may notice that the electron picture is now a five-particle wavefunction, in fact even Eq. (S17) should have an additional $|a_1\bar{a}_1\rangle$ closed shell that we neglected that time. On the other hand, the hole picture is much more simple. One can describe $|^4T_1\rangle$ by exciting one hole into the a_1 orbital from one of the three t_{2x}, t_{2y}, t_{2z} orbitals by a three-particle wavefunction. The two pictures are equivalent; however, for simplicity, we opt for the three particle language due to its much simpler and straightforward form. Here, we remind the reader again that Eq. (S18) only spans the $m_s = +\frac{3}{2}$ maximal spin projection. However, we will depict the $m_s = +\frac{1}{2}$ spin projection of $|^4T_1\rangle$ in Eq. (S31) later. It is worth to mention that, the x, y , and z components of the T_1 representation transform as axial vectors oriented along [100], [010] and [001] crystallographic directions in the same manner as the angular-momentum operators \hat{L}_x, \hat{L}_y , and \hat{L}_z .

Doublet states. We next consider the doublet manifold in spin projection $m_s = 1/2$. The $|^2T_1\rangle$ multiplet is spanned by the following combinations,

$$|^2T_{1i}\rangle = \frac{1}{\sqrt{2}} \begin{cases} |t_{2x}t_{2y}\bar{t}_{2y}\rangle - |t_{2x}t_{2z}\bar{t}_{2z}\rangle, & i = x, \\ |t_{2y}t_{2z}\bar{t}_{2z}\rangle - |t_{2y}t_{2x}\bar{t}_{2x}\rangle, & i = y, \\ |t_{2z}t_{2x}\bar{t}_{2x}\rangle - |t_{2z}t_{2y}\bar{t}_{2y}\rangle, & i = z. \end{cases} \quad (\text{S19})$$

The doubly degenerate $|^2E\rangle$ manifold is given by

$$|^2E_i\rangle = \begin{cases} \frac{1}{\sqrt{2}}(|t_{2x}\bar{t}_{2y}t_{2z}\rangle - |\bar{t}_{2x}t_{2y}t_{2z}\rangle), & i = x^2 - y^2, \\ \frac{1}{\sqrt{6}}(2|t_{2x}t_{2y}\bar{t}_{2z}\rangle - |t_{2x}\bar{t}_{2y}t_{2z}\rangle - |\bar{t}_{2x}t_{2y}t_{2z}\rangle), & i = 2z^2 - x^2 - y^2. \end{cases} \quad (\text{S20})$$

Finally, the $|^2T_2\rangle$ multiplet is spanned by

$$|^2T_{2i}\rangle = \frac{1}{\sqrt{2}} \begin{cases} |t_{2x}t_{2y}\bar{t}_{2y}\rangle + |t_{2x}t_{2z}\bar{t}_{2z}\rangle, & i = x, \\ |t_{2y}t_{2z}\bar{t}_{2z}\rangle + |t_{2y}t_{2x}\bar{t}_{2x}\rangle, & i = y, \\ |t_{2z}t_{2x}\bar{t}_{2x}\rangle + |t_{2z}t_{2y}\bar{t}_{2y}\rangle, & i = z. \end{cases} \quad (\text{S21})$$

Here we note that, in contrast to T_1 previously, x, y, z components of the T_2 representation transform as polar (real) vectors oriented along [100], [010], [001] crystallographic directions.

The energies of these multiplets can be parametrized entirely in terms of two-body Coulomb and exchange integrals within the Sugano–Tanabe–Kamimura formalism.²⁴ In this parametrization, the multiplet energies are given by:

$$\begin{aligned} E[|^4A_2\rangle] &= 3J(xy) - 3K(xy), & E[|^2T_1\rangle] &= 2J(xy) + J(zz) - 2K(xy), \\ E[|^2E\rangle] &= 3J(xy), & E[|^2T_2\rangle] &= 2J(xy) + J(zz), \end{aligned} \quad (\text{S22})$$

where J and K denote the relevant Coulomb and exchange integrals between pairs of t_{2x}, t_{2y} or t_{2z} orbitals depicted by x, y, z labels. Taking into account that $K(xy) > 0$ and $J(zz) > J(xy)$, the lowest-lying state is predicted to be $|^4A_2\rangle$, while the highest is $|^2T_2\rangle$. However, the relative ordering of the $|^2E\rangle$ and $|^2T_2\rangle$ states cannot be determined from these considerations alone.

To place this ambiguity in context, we note that in the well-studied case of the negatively charged vacancy in diamond,⁵² the experimentally and theoretically accepted level ordering is $|^2T_1\rangle, |^2E\rangle$, and $|^2T_2\rangle$ from lowest to highest energy (see Fig. 2 therein). While this analogy does not by itself fix the ordering in the present system, it provides a physically motivated reference for the expected hierarchy of the doublet states.

S10.2 Crystal-field Hamiltonian and symmetry lowering for the quartet excited state.

We describe the effect of symmetry lowering from the ideal T_d environment by introducing an effective crystal-field perturbation H_{cf} that lowers the symmetry to the trigonal C_{3v} symmetry. The relevant distortion corresponds to an uniaxial stress projected from the [111] direction. In the single-particle basis $\{t_{2x}, t_{2y}, t_{2z}\}$ of electronic orbitals in T_d , the corresponding crystal-field operator can be written as⁵³

$$H_{\text{cf}}^{(1)} = -\frac{\delta}{3} \left(|t_{2x}\rangle\langle t_{2y}| + |t_{2y}\rangle\langle t_{2z}| + |t_{2z}\rangle\langle t_{2x}| + \text{h.c.} \right) = -\frac{\delta}{3} \begin{pmatrix} 0 & 1 & 1 \\ 1 & 0 & 1 \\ 1 & 1 & 0 \end{pmatrix}, \quad (\text{S23})$$

where δ parameterizes the strength of the symmetry-lowering distortion. When acting on the $|a_1\rangle$ orbital, \hat{H}_{cf} merely produces a constant energy shift, which is not relevant for the level splittings discussed here and is therefore omitted.

Using the Slater–Condon rules, one can straightforwardly show that the effective crystal-field Hamiltonian within the many-body $|^4T_1\rangle$ manifold has the same matrix structure as in the single-particle $|t_{2i}\rangle$ basis:

$$\langle^4T_{1x}|\hat{H}_{\text{cf}}^{(1)}|^4T_{1y}\rangle = \underbrace{\langle\bar{a}_1\bar{t}_{2x}\bar{t}_y\bar{t}_{2z}t_{2x}|\hat{H}_{\text{cf}}^{(1)}|}_{=\langle^5A_2|}\underbrace{\bar{a}_1\bar{t}_{2x}\bar{t}_y\bar{t}_{2z}t_{2y}\rangle}_{=|^5A_2\rangle} = \langle^5A_2|^5A_2\rangle\langle t_{2x}|\hat{H}_{\text{cf}}^{(1)}|t_{2y}\rangle = -\frac{\delta}{3}. \quad (\text{S24})$$

However, there is opposite sign in the hole picture:

$$\langle^4T_{1x}|\hat{H}_{\text{cf}}^{(1)}|^4T_{1y}\rangle = \langle a_1t_{2y}t_{2z}|\hat{H}_{\text{cf}}^{(1)}|a_1t_{2z}t_{2x}\rangle = \langle t_{2y}t_{2z}|\hat{H}_{\text{cf}}^{(1)}|t_{2z}t_{2x}\rangle = -\langle t_{2z}t_{2y}|\hat{H}_{\text{cf}}^{(1)}|t_{2z}t_{2x}\rangle = -\langle t_{2y}|\hat{H}_{\text{cf}}^{(1)}|t_{2x}\rangle = +\frac{\delta}{3}. \quad (\text{S25})$$

Therefore, one would need to take into account that the crystal field parameter is inverted for holes because both pictures describe the exact same system. On the other hand, it is convenient to transform the coordinate system towards the $[111] C_{3v}$ symmetry axis by $|^4A'_2\rangle = \frac{1}{\sqrt{3}}(|^4T_{1x}\rangle + |^4T_{1y}\rangle + |^4T_{1z}\rangle)$, $|^4E_y\rangle = \frac{1}{\sqrt{2}}(|^4T_{1x}\rangle - |^4T_{1y}\rangle)$, $|^4E_x\rangle = \frac{1}{\sqrt{6}}(|^4T_{1x}\rangle + |^4T_{1y}\rangle - 2|^4T_{1z}\rangle)$ that transforms the crystal field Hamiltonian as follows:

$$\hat{H}_{\text{cf},[111]}^{(^4T_1)} = \frac{\delta}{3}\left(|^4E_x\rangle\langle^4E_x| + |^4E'_y\rangle\langle^4E_y| - |^4A'_2\rangle\langle^4A'_2|\right) = U\hat{H}_{\text{cf}}^{(1)}U^\dagger = \frac{\delta}{3}\begin{pmatrix} +1 & 0 & 0 \\ 0 & +1 & 0 \\ 0 & 0 & -2 \end{pmatrix}, \quad (\text{S26})$$

where the U unitary transformation depicts the change of natural basis that of T_d and C_{3v} :

$$U = \begin{pmatrix} \langle^4E_x| \\ \langle^4E_y| \\ \langle^4A'_2| \end{pmatrix} \begin{pmatrix} |^4T_{1x}\rangle & |^4T_{1y}\rangle & |^4T_{1z}\rangle \end{pmatrix} = \begin{pmatrix} \frac{1}{\sqrt{6}} & \frac{1}{\sqrt{6}} & \frac{-2}{\sqrt{6}} \\ \frac{1}{\sqrt{2}} & \frac{-1}{\sqrt{2}} & 0 \\ \frac{1}{\sqrt{3}} & \frac{1}{\sqrt{3}} & \frac{1}{\sqrt{3}} \end{pmatrix}. \quad (\text{S27})$$

Therefore, the parameter δ corresponds directly to the energy splitting between V_1 and V'_1 (or, analogously, V_2 and V'_2) optical transitions.

S10.3 Quenching of crystal-field splitting in the doublet manifolds

Having established the value of δ , we now estimate the crystal-field splitting of the doublet T_1 and T_2 electronic states. We treat H_{cf} as a spin-independent one-body operator acting within the $\{t_{2x}, t_{2y}, t_{2z}\}$ orbital subspace, and evaluate its matrix elements in the symmetry-adapted many-body basis using the Slater–Condon rules.

In the basis $\{|^2T_{1x}\rangle, |^2T_{1y}\rangle, |^2T_{1z}\rangle\}$ (as defined above), the diagonal matrix elements are all zeros because $\hat{H}_{\text{cf}}^{(1)}$ can only excite a single electron:

$$\begin{aligned} \langle^2T_{1x}|\hat{H}_{\text{cf}}^{(1)}|^2T_{1x}\rangle &= \frac{1}{2}\left(\langle t_{2x}t_{2y}\bar{t}_{2y} - \langle t_{2x}t_{2z}\bar{t}_{2z}|\right)\hat{H}_{\text{cf}}^{(1)}\left(\langle t_{2x}t_{2y}\bar{t}_{2y} - \langle t_{2x}t_{2z}\bar{t}_{2z}\rangle\right) \\ &= \frac{1}{2}\underbrace{\left(\langle t_{2x}t_{2y}\bar{t}_{2y}|\hat{H}_{\text{cf}}^{(1)}|t_{2x}t_{2y}\bar{t}_{2y}\right)}_{=0} \underbrace{\left(\langle t_{2x}t_{2y}\bar{t}_{2y}|\hat{H}_{\text{cf}}^{(1)}|t_{2x}t_{2z}\bar{t}_{2z}\rangle\right)}_{=0} \underbrace{\left(\langle t_{2x}t_{2z}\bar{t}_{2z}|\hat{H}_{\text{cf}}^{(1)}|t_{2x}t_{2y}\bar{t}_{2y}\rangle\right)}_{=0} \underbrace{\left(\langle t_{2x}t_{2z}\bar{t}_{2z}|\hat{H}_{\text{cf}}^{(1)}|t_{2x}t_{2z}\bar{t}_{2z}\rangle\right)}_{=0} = 0 \end{aligned} \quad (\text{S28})$$

where (i) and (iv) terms try to connect the same configurations, while (ii) and (iii) connecting configurations differ by two particles, thus all zeroes. Similarly, we determine the off-diagonal matrix elements as

$$\begin{aligned} \langle^2T_{1x}|\hat{H}_{\text{cf}}^{(1)}|^2T_{1y}\rangle &= \frac{1}{2}\left(\langle t_{2x}t_{2y}\bar{t}_{2y} - \langle t_{2x}t_{2z}\bar{t}_{2z}|\right)\hat{H}_{\text{cf}}^{(1)}\left(\langle t_{2y}t_{2z}\bar{t}_{2z} - \langle t_{2y}t_{2x}\bar{t}_{2x}\rangle\right) \\ &= \frac{1}{2}\left(\underbrace{\langle t_{2x}t_{2y}\bar{t}_{2y}|\hat{H}_{\text{cf}}^{(1)}|t_{2y}t_{2z}\bar{t}_{2z}\rangle}_{=0} - \langle t_{2x}t_{2y}\bar{t}_{2y}|\hat{H}_{\text{cf}}^{(1)}|t_{2y}t_{2x}\bar{t}_{2x}\rangle - \langle t_{2x}t_{2z}\bar{t}_{2z}|\hat{H}_{\text{cf}}^{(1)}|t_{2y}t_{2z}\bar{t}_{2z}\rangle + \underbrace{\langle t_{2x}t_{2z}\bar{t}_{2z}|\hat{H}_{\text{cf}}^{(1)}|t_{2y}t_{2x}\bar{t}_{2x}\rangle}_{=0}\right) \\ &= \frac{1}{2}\left(0 + \underbrace{\langle\bar{t}_{2y}|\hat{H}_{\text{cf}}^{(1)}|\bar{t}_{2x}\rangle}_{=\delta/3} - \underbrace{\langle t_{2x}|\hat{H}_{\text{cf}}^{(1)}|t_{2y}\rangle}_{=-\delta/3} + 0\right) = 0 \end{aligned} \quad (\text{S29})$$

where even the innermost two terms are annihilating each other due to Slater–Condon rules: $-\langle t_{2x}t_{2y}\bar{t}_{2y}|\hat{H}_{\text{cf}}^{(1)}|t_{2y}t_{2x}\bar{t}_{2x}\rangle = +\langle t_{2y}t_{2x}\bar{t}_{2y}|\hat{H}_{\text{cf}}^{(1)}|t_{2y}t_{2x}\bar{t}_{2x}\rangle = +\langle\bar{t}_{2y}|\hat{H}_{\text{cf}}^{(1)}|\bar{t}_{2x}\rangle = \langle\bar{t}_{2y}|\hat{H}_{\text{cf}}^{(1)}|\bar{t}_{2x}\rangle = \delta/3$. Therefore, the crystal field is quenched for the doublets at the zeroth order of perturbation.

S11 Crystal-field splitting by means of multi-configuration corrections from quantum embedding

In this section, we shall try to determine the crystal field splitting for the correlated $|^2T_1\rangle$, $|^2T_2\rangle$ multiplets from the following ingredients:

- Crystal field splitting parameter (δ) observed in the spin quartet transition: $|^4A_2\rangle \xrightleftharpoons{1.4\text{eV}} |^4T_1\rangle$.
- Multiconfigurational expansion of the doublet states up to first and second excited Slater determinants as obtained from quantum embedding.

Then, we will evaluate the $H_{\text{cf}}^{(1)} = -\frac{\delta}{3}(|t_{2x}\rangle\langle t_{2y}| + \dots)$ single particle crystal field operator on the multiconfigurational expansion of $|^2T_1\rangle$ and $|^2T_2\rangle$ doublets:

$$|^2T_1^{\text{corr}}\rangle = a\underbrace{|^2T_1\rangle}_{a_1^1 t_2^3} + b\underbrace{|^2T_1'\rangle}_{a_1^1 t_2^4}, \quad |^2T_2^{\text{corr}}\rangle = c\underbrace{|^2T_2\rangle}_{a_1^2 t_2^3} + d\underbrace{|^2T_2'\rangle}_{a_1^1 t_2^4} + e\underbrace{|^2T_2''\rangle}_{a_1^0 t_2^5}, \quad |^2E^{\text{corr}}\rangle = f\underbrace{|^2E\rangle}_{a_1^2 t_2^3} + g\underbrace{|^2E'\rangle}_{a_1^1 t_2^4}. \quad (\text{S30})$$

First, we need to obtain the symmetry adapted form of the first excited $|^2T_1'\rangle$, $|^2T_2'\rangle$ and second excited $|^2T_2''\rangle$ configurations.

We estimate each configuration's expansion directly from our quantum embedding calculations for the V_k site thus we obtain the following $a^2 = 93(2)\%$, $b^2 = 6(1)\%$, $c^2 = 85(5)\%$, $d^2 = 11(6)\%$, $e^2 = 4(1)\%$, $f^2 = 78(1)\%$, $g^2 = 20(2)\%$ factors where the error bars are originating from the inherent crystal field of a 128-atom model. The small supercell size gives rise to severe numerical inaccuracies in the quantum embedding calculations as well, a system size is so small cannot capture the finite size effects of δ correctly. Thus, the value of parameters a - e as well as the energy position of $|^4T_1\rangle$, $|^2T_2^{\text{corr}}\rangle$, $|^2E^{\text{corr}}\rangle$, $|^2T_1^{\text{corr}}\rangle$ are not exactly the same see Fig. S19 or Fig. 4(a) of the main text where degenerate levels are not exactly degenerate. Therefore, we rely only the average of these parameters and take the δ crystal field parameter from the $|^4T_2\rangle$ excited quartet.

S11.1 Excited symmetry-adapted three-hole wavefunctions

The first excited determinants originate from the $(a_1^1 t_2^4)$ single particle occupation spanning total 5 electrons in the configurational space. In contrast, it is far more convenient to describe the system in the equivalent hole picture that can be represented by three holes: $(a_1 t_2^3)$.

According to Fig. 2.2 in the book of Sugano²⁴, we can expand t_2^2 for the first excited configurations $(a_1^1 t_2^2) = {}^2A_1 \otimes ({}^3T_1 \oplus {}^1E \oplus {}^1T_2 \oplus {}^1A_1) = {}^4T_1 \oplus {}^2T_1 \oplus {}^2E \oplus {}^2T_2 \oplus {}^2A_1$ thus we can identify both $|^2T_1'\rangle$ and $|^2T_2'\rangle$ configurations in Eq. (S30). Specifically, we can identify that both $|^4T_2\rangle$ from Eq. (S18) and $|^2T_2'\rangle$ multiplets originates by adding an additional a_1 particle to the two particle construction: $|^3T_2\rangle = \{|t_{2y}t_{2z}\rangle, |t_{2z}t_{2x}\rangle, |t_{2x}t_{2y}\rangle\}$ as defined in Table 2.2 of the book²⁴. However, determining the wavefunction that of $|^2T_2'\rangle$ is not a trivial task, thus we shall proceed on an alternative tour. What we know for sure is that the spin projection $m_s = +\frac{1}{2}$ of $|^4T_2\rangle$ can be written as

$$|^4T_{1i}^{m_s=+\frac{1}{2}}\rangle = \frac{1}{\sqrt{3}} \begin{cases} |\bar{a}_1 t_{2y} t_{2z}\rangle + |a_1 \bar{t}_{2y} t_{2z}\rangle + |a_1 t_{2y} \bar{t}_{2z}\rangle, & i = x, \\ |\bar{a}_1 t_{2z} t_{2x}\rangle + |a_1 \bar{t}_{2z} t_{2x}\rangle + |a_1 t_{2z} \bar{t}_{2x}\rangle, & i = y, \\ |\bar{a}_1 t_{2x} t_{2y}\rangle + |a_1 \bar{t}_{2x} t_{2y}\rangle + |a_1 t_{2x} \bar{t}_{2y}\rangle, & i = z, \end{cases} \quad (\text{S31})$$

that expression can be obtained by applying the \hat{S}_- pin lowering operator on Eq. (S18)'s $m_s = +\frac{3}{2}$ case. At this point, one may notice that both $|^2T_2'\rangle$ and $|^4T_{1i}^{m_s=+\frac{1}{2}}\rangle$ have to be composed from the same $(a_1^1 t_{2\alpha}^1 t_{2\beta}^1)$ orbitals where $\alpha \neq \beta$. Therefore, we can construct the following additional six symmetry adapted configurations made from $|a_1 t_{2\alpha} t_{2\beta}\rangle$'s that are orthogonal to the wavefunctions from Eq. (S31):

$$|^2T'_{1i}\rangle = \frac{1}{\sqrt{6}} \begin{cases} 2|\bar{a}_1 t_{2y} t_{2z}\rangle - |a_1 \bar{t}_{2y} t_{2z}\rangle - |a_1 t_{2y} \bar{t}_{2z}\rangle, & i = x, \\ 2|\bar{a}_1 t_{2z} t_{2x}\rangle - |a_1 \bar{t}_{2z} t_{2x}\rangle - |a_1 t_{2z} \bar{t}_{2x}\rangle, & i = y, \\ 2|\bar{a}_1 t_{2x} t_{2y}\rangle - |a_1 \bar{t}_{2x} t_{2y}\rangle - |a_1 t_{2x} \bar{t}_{2y}\rangle, & i = z \end{cases} \quad \text{and} \quad |^2T'_{2i}\rangle = \frac{1}{\sqrt{2}} \begin{cases} |a_1 \bar{t}_{2y} t_{2z}\rangle - |a_1 t_{2y} \bar{t}_{2z}\rangle, & i = x, \\ |a_1 \bar{t}_{2z} t_{2x}\rangle - |a_1 t_{2z} \bar{t}_{2x}\rangle, & i = y, \\ |a_1 \bar{t}_{2x} t_{2y}\rangle - |a_1 t_{2x} \bar{t}_{2y}\rangle, & i = z. \end{cases} \quad (\text{S32})$$

One can identify the first orbital triplet as a $|^2T_1'\rangle$ because it can be proven that it is transforming as the T_1 irreducible representation. Surprisingly the other $|^2T_2'\rangle$ configuration is also a configuration we are looking for. It is trivial that, the C_3 threefold rotations will just permute the x , y , z coordinates for both $|^2T'_{1i}\rangle$ and $|^2T'_{2i}\rangle$. However, we still need to prove that σ_v mirror planes do not mix $|^2T'_{1i}\rangle$ and $|^2T'_{2i}\rangle$ thus they will form individual T_1 and T_2 representations. The first mirror plane ($\sigma_v^{(1)}$) will interchange the first two coordinates: $x \leftrightarrow y$ while it will leave z intact. Therefore its effect will be $\sigma_v^{(1)}|^2T'_{1x}\rangle = \hat{\sigma}_v^{(1)}(2|\bar{a}_1 t_{2y} t_{2z}\rangle - |a_1 \bar{t}_{2y} t_{2z}\rangle - |a_1 t_{2y} \bar{t}_{2z}\rangle) = (2|\bar{a}_1 t_{2x} t_{2z}\rangle - |a_1 \bar{t}_{2x} t_{2z}\rangle - |a_1 t_{2x} \bar{t}_{2z}\rangle) = -|^2T'_{1y}\rangle$ on the first wavefunction. We leave the case of $|^2T'_{1y}\rangle$ and $|^2T'_{1z}\rangle$ to the reader and the case of the other 5 remaining ($\sigma_v^{(2-6)}$) mirror planes. The

final transformation law will be $\sigma_v^{(1)} |^2 T'_{1i} \rangle = \begin{pmatrix} 0 & -1 & 0 \\ -1 & 0 & 0 \\ 0 & 0 & -1 \end{pmatrix} |^2 T'_{1i} \rangle$ for $\sigma_v^{(1)}$, thus the trace of the operation will be: $\text{Tr}(\sigma_v^{(1)}) = -1$. This is the same value that appears in the character table of T_d at the column for the six $6\sigma_v$ mirror planes at the T_1 irreducible representation's row. Similarly, in the case of $|^2 T'_{2i} \rangle$ the trace of the operation would be $\text{Tr}(\sigma_v^{(1)}) = +1$ therefore, we correctly assumed in Eq. (S32) that it is transforming as T_2 .

The excited $|^2 E' \rangle$ can be generated by multiplying the $|^1 E \rangle$ (t_2^2) two-hole wavefunction (see Table 2.2 in the book²⁴ of Sugano) by an $(a_1^1) = |^2 A_1 \rangle$ hole:

$$|^2 E' \rangle = |a_1 \rangle \otimes |^1 E \rangle = \begin{cases} \frac{1}{\sqrt{6}} (2|a_1 \bar{t}_2 z t_{2z} \rangle - |a_1 \bar{t}_2 x t_{2x} \rangle - |a_1 \bar{t}_2 y t_{2y} \rangle), \\ \frac{1}{\sqrt{2}} (|a_1 \bar{t}_2 x t_{2x} \rangle - |a_1 \bar{t}_2 y t_{2y} \rangle), \end{cases} \quad (\text{S33})$$

Finally, only one configuration is possible by occupation $(a_1^0 t_2^5)$:

$$|^2 T''_{2i} \rangle = \begin{cases} |\bar{a}_1 a_1 t_{2x} \rangle, & i = x, \\ |\bar{a}_1 a_1 t_{2y} \rangle, & i = y, \\ |\bar{a}_1 a_1 t_{2z} \rangle, & i = z, \end{cases} \quad (\text{S34})$$

thus $|^2 T''_1 \rangle, |^2 E'' \rangle$ terms are not possible in the configuration expansion that of Eq. (S30). Now, with all ingredients at hand, our next step will be to determine the crystal field matrix elements for $|^2 T_1^{\text{corr}} \rangle$ and $|^2 T_2^{\text{corr}} \rangle$ in the next subsection.

S11.2 First order multi-configurational crystal field corrections for $|^2 T_1 \rangle$ and $|^2 T_2 \rangle$

In this subsection we will determine the leading terms due to $\hat{H}_{\text{cf}}^{(1)}$ from Eq. Eq. (S23) by means of first order perturbation theory. Firstly, we determine the expansion for the lower $|^2 T_1^{\text{corr}} \rangle$ doublet. One may notice that $H_{\text{cf}}^{(1)}$ does not contain any excitation $|a_1 \rangle \langle t_{2i}|$ term, thus $\langle^2 T_{1i} | H_{\text{cf}}^{(1)} |^2 T'_{1j} \rangle$ is zero.

Therefore, we can write simply that only the third term matters in the multi-configurational expansion: $\langle^2 T_{1i}^{\text{corr}} | H_{\text{cf}}^{(1)} |^2 T_{1j}^{\text{corr}} \rangle = a^2 \langle^2 T_{1i} | H_{\text{cf}}^{(1)} |^2 T_{1j} \rangle + 2ab \langle^2 T_{1i} | H_{\text{cf}}^{(1)} |^2 T'_{1j} \rangle + b^2 \langle^2 T'_{1i} | H_{\text{cf}}^{(1)} |^2 T'_{1j} \rangle$. According to the Slater–Condon rules the matrix element will be:

$$\begin{aligned} \langle^2 T'_{1x} | H_{\text{cf}}^{(1)} |^2 T'_{1y} \rangle &= \frac{1}{6} (2\langle \bar{a}_1 t_{2y} t_{2z} | - \langle a_1 \bar{t}_2 y t_{2z} | - \langle a_1 t_{2y} \bar{t}_2 z |) \hat{H}_{\text{cf}}^{(1)} (2|\bar{a}_1 t_{2y} t_{2z} \rangle - |a_1 \bar{t}_2 y t_{2z} \rangle - |a_1 t_{2y} \bar{t}_2 z \rangle) = \\ &= \frac{1}{6} \left(\underbrace{+4\langle \bar{a}_1 t_{2y} t_{2z} | \hat{H}_{\text{cf}}^{(1)} | \bar{a}_1 t_{2z} t_{2x} \rangle}_{=+4\delta/3} - \underbrace{2\langle \bar{a}_1 t_{2y} t_{2z} | \hat{H}_{\text{cf}}^{(1)} | a_1 \bar{t}_2 z t_{2x} \rangle}_{=0} - \underbrace{2\langle \bar{a}_1 t_{2y} t_{2z} | \hat{H}_{\text{cf}}^{(1)} | a_1 t_{2z} \bar{t}_2 x \rangle}_{=0} \right. \\ &\quad - \underbrace{2\langle a_1 \bar{t}_2 y t_{2z} | \hat{H}_{\text{cf}}^{(1)} | \bar{a}_1 t_{2z} t_{2x} \rangle}_{=0} + \underbrace{\langle a_1 \bar{t}_2 y t_{2z} | \hat{H}_{\text{cf}}^{(1)} | a_1 \bar{t}_2 z t_{2x} \rangle}_{=0} + \underbrace{\langle a_1 \bar{t}_2 y t_{2z} | \hat{H}_{\text{cf}}^{(1)} | a_1 t_{2z} \bar{t}_2 x \rangle}_{=+\delta/3} \\ &\quad \left. - \underbrace{2\langle a_1 t_{2y} \bar{t}_2 z | \hat{H}_{\text{cf}}^{(1)} | \bar{a}_1 t_{2z} t_{2x} \rangle}_{=0} + \underbrace{\langle a_1 t_{2y} \bar{t}_2 z | \hat{H}_{\text{cf}}^{(1)} | a_1 \bar{t}_2 z t_{2x} \rangle}_{=\delta/3} + \underbrace{\langle a_1 t_{2y} \bar{t}_2 z | \hat{H}_{\text{cf}}^{(1)} | a_1 t_{2z} \bar{t}_2 x \rangle}_{=0} \right) = \frac{\delta}{3} \times \frac{4+1+1}{6} = +\frac{\delta}{3} \end{aligned} \quad (\text{S35})$$

that is the exact same that we seen for the spin quartet $|^4 T_1 \rangle$. Therefore, $|^2 T_1 \rangle$ will split into $|^2 A_2 \rangle$ and $|^2 E \rangle$ where the $|^2 A_2 \rangle$ is the lowest followed by $|^2 E \rangle$ with an energy value of κ_{theory} . However, the $|^2 T'_{1z} \rangle$ configuration is only present with a small probability of b^2 thus the crystal field splitting for $|^2 T_1^{\text{corr}} \rangle$ will be:

$$\boxed{\kappa^{(1)} = b^2 \delta} \quad (\text{S36})$$

In the case of $|^2 T_2^{\text{corr}} \rangle$ the configuration decomposition is the following: $\langle^2 T_{2i}^{\text{corr}} | H_{\text{cf}}^{(1)} |^2 T_2^{\text{corr}} \rangle = d^2 \langle^2 T_{2i} | H_{\text{cf}}^{(1)} |^2 T_{2j} \rangle + e^2 \langle^2 T'_{2i} | H_{\text{cf}}^{(1)} |^2 T''_{2j} \rangle$ because the $\langle^2 T_{1i} | H_{\text{cf}}^{(1)} |^2 T_{1j} \rangle, \langle^2 T_{1i} | H_{\text{cf}}^{(1)} |^2 T'_{1j} \rangle, \langle^2 T'_{2i} | H_{\text{cf}}^{(1)} |^2 T''_{2j} \rangle$ matrix elements are all zeroes. The matrix elements for the first excited configuration is:

$$\begin{aligned} \langle^2 T'_{2x} | H_{\text{cf}}^{(1)} |^2 T'_{2y} \rangle &= \frac{1}{2} (\langle a_1 \bar{t}_2 y t_{2z} | - \langle a_1 t_{2y} \bar{t}_2 z |) \hat{H}_{\text{cf}}^{(1)} (|a_1 \bar{t}_2 z t_{2x} \rangle - |a_1 t_{2z} \bar{t}_2 x \rangle) = \\ &= \frac{1}{2} \left(\underbrace{+\langle a_1 \bar{t}_2 y t_{2z} | \hat{H}_{\text{cf}}^{(1)} | a_1 \bar{t}_2 z t_{2x} \rangle}_{=0} - \underbrace{\langle a_1 \bar{t}_2 y t_{2z} | \hat{H}_{\text{cf}}^{(1)} | a_1 t_{2z} \bar{t}_2 x \rangle}_{=-\delta/3} \right. \\ &\quad \left. - \underbrace{\langle a_1 t_{2y} \bar{t}_2 z | \hat{H}_{\text{cf}}^{(1)} | a_1 \bar{t}_2 z t_{2x} \rangle}_{=-\delta/3} + \underbrace{\langle a_1 t_{2y} \bar{t}_2 z | \hat{H}_{\text{cf}}^{(1)} | a_1 t_{2z} \bar{t}_2 x \rangle}_{=0} \right) = \frac{\delta}{3} \times \frac{-1-1}{2} = -\frac{\delta}{3} \end{aligned} \quad (\text{S37})$$

while the second excited configuration will be:

$$\langle {}^2T''_{2x} | H_{\text{cf}}^{(1)} | {}^2T''_{2y} \rangle = \langle \bar{a}_1 a_1 t_{2x} | H_{\text{cf}}^{(1)} | \bar{a}_1 a_1 t_{2y} \rangle = \langle t_{2x} | H_{\text{cf}}^{(1)} | t_{2y} \rangle = -\frac{\delta}{3}. \quad (\text{S38})$$

Therefore the $|^2E''\rangle$ orbital doublet will precede the $|^2A_1\rangle$ orbital singlet in $|^2T_1^{\text{corr}}\rangle$'s crystal field splitting by the following energy:

$$\boxed{\eta^{(1)} = -(d^2 + e^2)\delta}. \quad (\text{S39})$$

S11.3 Second order corrections

In order to determine the second order corrections due to $H_{\text{cf}}^{(1)}$, first, we rewrite the projector to the $|^2E\rangle$ doublet that of Eq. (S20) as follows:

$$|^2E\rangle\langle {}^2E| = \sum_{\substack{\alpha=\{x^2-y^2 \\ ,2z^2-x^2-y^2\}}} |^2E_\alpha\rangle\langle {}^2E_\alpha| = \frac{2}{3}\text{Re} \left[\begin{aligned} & \left(|t_{2x}t_{2y}\bar{t}_{2z}\rangle + e^{i2\pi/3}|t_{2x}\bar{t}_{2y}t_{2z}\rangle + e^{-i2\pi/3}|\bar{t}_{2x}t_{2y}t_{2z}\rangle \right) \\ & \times \left(\langle t_{2x}t_{2y}\bar{t}_{2z}| + \langle t_{2x}\bar{t}_{2y}t_{2z}|e^{-i2\pi/3} + \langle \bar{t}_{2x}t_{2y}t_{2z}|e^{+i2\pi/3} \right) \end{aligned} \right], \quad (\text{S40})$$

where one may notice that the perturbation jumps to an energetically lower state $|^2E\rangle$, thus the Δ energy difference is negative. We do this to get a more compact form for the second order perturbation through the middle $|^2E\rangle$ doublet:

$$\kappa_E^{(2)} = 3 \frac{\langle {}^2T_{2x}^{\text{corr}} | \hat{H}_{\text{cf}}^{(1)} | {}^2E^{\text{corr}} \rangle \langle {}^2E^{\text{corr}} | \hat{H}_{\text{cf}}^{(1)} | {}^2T_{2y}^{\text{corr}} \rangle}{\underbrace{E[|{}^2E\rangle] - E[|{}^2T_2\rangle]}_{=-\Delta}} = -\frac{3c^2f^2}{\Delta\sqrt{2}\sqrt{2}} \times \hat{H}_{\text{cf}}^{(1)} \left(|t_{2y}t_{2z}\bar{t}_{2z}\rangle + |t_{2y}t_{2x}\bar{t}_{2x}\rangle \right). \quad (\text{S41})$$

where the terms containing d, g coefficients all vanish because it can be derived that the second term in the transition matrix element is zero: $\langle {}^2T_2^{\text{corr}} | \hat{H}_{\text{cf}}^{(1)} | {}^2E^{\text{corr}} \rangle = cf\langle {}^2T_2 | \hat{H}_{\text{cf}}^{(1)} | {}^2E \rangle + dg\cancel{\langle {}^2T_2' | \hat{H}_{\text{cf}}^{(1)} | {}^2E' \rangle}$. Now, we insert the decomposition of $|^2E\rangle\langle {}^2E|$ projector:

$$\begin{aligned} \eta_E^{(2)} &= -\frac{3}{\Delta} \left(\frac{\delta}{3} \right)^2 \frac{2^2c^2f^2}{2} \times \frac{2}{3} \left(\langle t_{2x}t_{2z}\bar{t}_{2y} | + \langle t_{2x}t_{2y}\bar{t}_{2z} | \right) \times \text{Re} \left[|t_{2x}t_{2y}\bar{t}_{2z}\rangle - e^{i2\pi/3}|t_{2x}t_{2z}\bar{t}_{2y}\rangle + e^{-i2\pi/3}|t_{2y}t_{2z}\bar{t}_{2x}\rangle \right. \\ &\quad \left. \times \left(\langle t_{2x}t_{2y}\bar{t}_{2z} | - \langle t_{2x}t_{2z}\bar{t}_{2y} | e^{-i2\pi/3} + \langle t_{2y}t_{2z}\bar{t}_{2x} | e^{+i2\pi/3} \right) \right] \times \left(|t_{2y}t_{2z}\bar{t}_{2z}\rangle + |t_{2y}t_{2z}\bar{t}_{2x}\rangle \right) \end{aligned} \quad (\text{S42})$$

$$= -\frac{4\delta^2}{9\Delta} \text{Re} \left[\left(1 - 1e^{i2\pi/3} + 0e^{-i2\pi/3} \right) \left(1 - 1e^{-i2\pi/3} + 0e^{+i2\pi/3} \right) \right] = \boxed{\kappa_E^{(2)} = -c^2f^2 \frac{4\delta^2}{3\Delta}} \quad (\text{S43})$$

We have seen in Eqs. (S28) and (S29) that the crystal field for both $|^2T_1\rangle$ and $|^2T_2\rangle$ vanishes. However, the offdiagonal matrix elements does not: $\langle {}^2T_{1x} | \hat{H}_{\text{cf}}^{(1)} | {}^2T_{2y} \rangle = \frac{\delta}{3}$. This allows us calculate the second order perturbation of the crystal field:

$$\eta_T^{(2)} = \frac{\langle {}^2T_{1x}^{\text{corr}} | \hat{H}_{\text{cf}}^{(1)} | {}^2T_{2z}^{\text{corr}} \rangle \langle {}^2T_{2z}^{\text{corr}} | \hat{H}_{\text{cf}}^{(1)} | {}^2T_{1y}^{\text{corr}} \rangle}{\underbrace{E[|{}^2T_1\rangle] - E[|{}^2T_2\rangle]}_{=\Lambda}} = \boxed{\eta_T^{(2)} = -\frac{a^2c^2\delta^2}{\Lambda}}, \quad (\text{S44})$$

where only the leading terms involving (a and c) in multiconfigurational expansion remains because $\langle {}^2T_{1x}' | \hat{H}_{\text{cf}}^{(1)} | {}^2T_{2y}' \rangle$ matrix element for (b and d) is zero. We note that the same correction also exists for the lowest triplet with the opposite sign because the energy difference is being flipped: $\boxed{\kappa_T^{(2)} = -\eta_T^{(2)}}$.

Additional terms In summary, we collect all correction terms terms as follows:

$$\kappa_{\text{theory}} = \kappa^{(1)} + \kappa_T^{(2)} + \mathcal{O}(\delta^3) \approx \underbrace{b^2\delta}_{\substack{V_h:+0.45\text{ meV} \\ V_k:+1.88\text{ meV}}} + \underbrace{a^2c^2\frac{\delta^2}{\Lambda}}_{\substack{V_h:+0.04\text{ meV} \\ V_k:+0.63\text{ meV}}} \quad (\text{S45})$$

and

$$\eta_{\text{theory}} = \eta^{(1)} + \eta_E^{(2)} + \eta_T^{(2)} + \mathcal{O}(\delta^3) \approx \underbrace{-(d^2 + e^2)\delta}_{\substack{V_h: -1.04 \text{ meV} \\ V_k: -4.33 \text{ meV}}} \underbrace{-c^2 f^2 \frac{4\delta^2}{3\Delta}}_{\substack{V_h: -0.12 \text{ meV} \\ V_k: -2.01 \text{ meV}}} \underbrace{-a^2 c^2 \frac{\delta^2}{\Lambda}}_{\substack{V_h: -0.04 \text{ meV} \\ V_k: -0.63 \text{ meV}}} \quad (\text{S46})$$

to evaluate the the theoretical model. We use the C_{3v} crystal field parameters as calculated by P. Udvarhelyi et al, see Table 1. in Ref.¹⁷. Therefore, we use $\delta = 7$ meV for V_h and $\delta = 29$ meV for V_k . We note that these values are intrinsic, they are not multiplied by the Ham reduction factor of the Jahn–Teller effect. However, similarly to \hat{H}_{crystal} in Eq. (S35), the \hat{H}_{JT} Jahn–Teller Hamiltonian¹⁷ is also quenched in the uncorrelated doublet wavefunctions eg. $\langle {}^2T_1 | \hat{H}_{\text{JT}} | {}^2T_1 \rangle = \langle {}^2T_2 | \hat{H}_{\text{JT}} | {}^2T_2 \rangle = 0$. Therefore, we neglect the Jahn–Teller Ham factors for $|{}^2T_2^{\text{corr}}\rangle$, $|{}^2T_1^{\text{corr}}\rangle$ doublet levels for simplicity. We substitute the experimentally observed values of $\Delta = 369$ and (371) meV, $\Lambda = 1095$ and (1065) meV for V_h and (V_k) respectively. Therefore, our theory predicts the following crystal field parameters:

$$\boxed{\begin{array}{ll} V_h : \begin{cases} \kappa_{\text{theory}} = +0.5 \text{ meV} & |\kappa_{\text{expt.}}| < 1 \text{ or} > 10 \text{ meV} \\ \eta_{\text{theory}} = -1.2 \text{ meV} & \eta_{\text{expt.}} = -4 \text{ meV} \end{cases} \\ V_h : \begin{cases} \kappa_{\text{theory}} = +2.5 \text{ meV} & |\kappa_{\text{expt.}}| < 1 \text{ or} > 10 \text{ meV} \\ \eta_{\text{theory}} = -7.0 \text{ meV} & \eta_{\text{expt.}} = -10 \text{ meV} \end{cases} \end{array}} \quad (\text{S47})$$

Therefore, based on Eq. (S47), we can make the following conclusions:

- The sign of the η_{theory} crystal field parameter for $|{}^2T_2^{\text{corr}}\rangle$ is in agreement with the experiments. It was identified from optical polarization measurements (see A, B, C optical peaks in Fig. 4(c-e) of the main text) that the crystal field shifts the orbitally $2\times$ degenerate $|{}^2E''\rangle$ level (of C_{3v} symmetry) downwards while lifts $|{}^2A_2\rangle$ upwards thus $\eta_{\text{expt.}}$ is negative.
- The κ_{theory} crystal field splitting that of $|{}^2T_2^{\text{corr}}\rangle$ is significantly smaller than the previous η_{theory} . Therefore, the present theoretical result suggests that $|\kappa_{\text{expt.}}| > 10$ meV can not be true. This can be interpreted as E, F transitions in Fig. 4(c-e) exhibit a splitting smaller than the experimental spectral resolution: $|\kappa_{\text{expt.}}| < 1$ meV.

S12 Optical selection rules for spin doublets

To determine the optical selection rules of the silicon vacancy center, we work in a representation of the T_2 and T_1 manifolds that is simultaneously adapted to the crystallographic coordinate system of 4H-SiC and to the symmetry operations of the C_{3v} subgroup. Concretely, we express the representation matrices of the T_2 manifold in a basis aligned with the crystallographic axes, which also renders the action of the C_{3v} operations block diagonal. This corresponds to a unitary change of basis from t_{2x}, t_{2y}, t_{2z} to $t_{2,a_1}, t_{2,e_x}, t_{2,e_y}$, where t_{2,a_1} transforms as a vector aligned with the crystallographic c axis, while t_{2,e_x} and t_{2,e_y} transform as vectors lying within the basal plane perpendicular to c . In this basis, the restriction of the T_2 representation to the C_{3v} subgroup decomposes as $T_2 \downarrow C_{3v} = A_1 \oplus E$, and the notation reflects that the selected components of T_2 also correspond to irreducible representations of C_{3v} .

An analogous transformation is performed for the T_1 representation. In this case, the transformed basis functions behave as pseudovectors aligned with the crystallographic coordinate axes. Accordingly, upon restriction to the C_{3v} subgroup, the T_1 representation decomposes as $T_1 \downarrow C_{3v} = A_2 \oplus E$.

In this symmetry-adapted representation, the many-body electronic states are constructed using group-theoretical projection operators,⁵⁴ applied to the direct product of the orbital and spin representations. The resulting basis spans the antisymmetrized three-hole configurations transforming as T_1 and T_2 . In the following, we explicitly list the resulting many-body wavefunctions

corresponding to the T manifolds (to shorten the notation, we define $a \equiv t_{2,a_1}$, $x \equiv t_{2,e_x}$, and $y \equiv t_{2,e_y}$):

$$\begin{aligned}
|T_1(A_2)\rangle &= \frac{1}{\sqrt{6}} (|ax\bar{y}\rangle - |ay\bar{x}\rangle - 2|xy\bar{a}\rangle), \\
|T_1(E_x)\rangle &= \frac{1}{\sqrt{3}} \left(-|ax\bar{y}\rangle - |ay\bar{x}\rangle + \frac{1}{\sqrt{2}}|ay\bar{a}\rangle - \frac{1}{\sqrt{2}}|xy\bar{x}\rangle \right), \\
|T_1(E_y)\rangle &= \frac{1}{\sqrt{3}} \left(\frac{1}{\sqrt{2}}|ax\bar{a}\rangle + |ax\bar{x}\rangle - |ay\bar{y}\rangle + \frac{1}{\sqrt{2}}|xy\bar{y}\rangle \right); \\
|T_2(A_1)\rangle &= \frac{1}{\sqrt{2}} (|ax\bar{x}\rangle + |ay\bar{y}\rangle), \\
|T_2(E_x)\rangle &= \frac{1}{\sqrt{2}} (|ax\bar{a}\rangle + |xy\bar{y}\rangle), \\
|T_2(E_y)\rangle &= \frac{1}{\sqrt{2}} (|ay\bar{a}\rangle + |xy\bar{x}\rangle).
\end{aligned}$$

The electric dipole operator transforms as the T_2 vector representation. In the chosen basis, the dipole component along the c axis, μ_z , transforms as the a component of the T_2 representation, while the in-plane components μ_x and μ_y transform as the x and y components of T_2 , respectively. Consequently, dipole-mediated optical selection rules follow directly from the $T_1 \otimes T_2 \otimes T_2$ coupling. In this representation, the allowed couplings are encoded in the corresponding Clebsch–Gordan matrices (calculated using GTPack package^{55,56}):

$$C_a(\mu_z) = \begin{pmatrix} 0 & 0 & 0 \\ 0 & 0 & \frac{1}{\sqrt{2}} \\ 0 & -\frac{1}{\sqrt{2}} & 0 \end{pmatrix}, \quad C_x(\mu_x) = \begin{pmatrix} 0 & 0 & -\frac{1}{\sqrt{2}} \\ 0 & 0 & 0 \\ \frac{1}{\sqrt{2}} & 0 & 0 \end{pmatrix}, \quad C_y(\mu_y) = \begin{pmatrix} 0 & \frac{1}{\sqrt{2}} & 0 \\ -\frac{1}{\sqrt{2}} & 0 & 0 \\ 0 & 0 & 0 \end{pmatrix}, \quad (S48)$$

where the matrix elements correspond to the actual Clebsch–Gordan coefficients, defined as $(C_l)_{ij} = \langle T_{2;j} T_{2;l} | T_{1;i} \rangle^*$, with $i = 1$ corresponding to a and $i = 2, 3$ corresponding to x, y .

These matrices imply that μ_z polarization induces transitions only between different components of the E manifolds (e.g., $T_1(E_x) \leftrightarrow T_2(E_y)$), whereas in-plane polarizations μ_x and μ_y induce transitions between $T_2(A_1)$ and $T_1(E_{x,y})$, or between $T_2(E_{x,y})$ and $T_1(A_2)$. These selection rules apply both at the many-body level, where only the total many-body symmetries are relevant, and at the orbital level, where they follow from the Slater–Condon rules applied to the wavefunctions listed above.

Supplemental results and discussion

S13 Transient Absorption Spectroscopy Results

As illustrated in Fig. S4-a, a two-dimensional temporal and spectral scan of the sample was conducted, with the sample being pumped at 800 nm (1.55 eV), exciting both V_h and V_k via their phonon-sideband (PSB), with unpolarized probe light. The results of this scan revealed various distinct features that can be interpreted as follows:

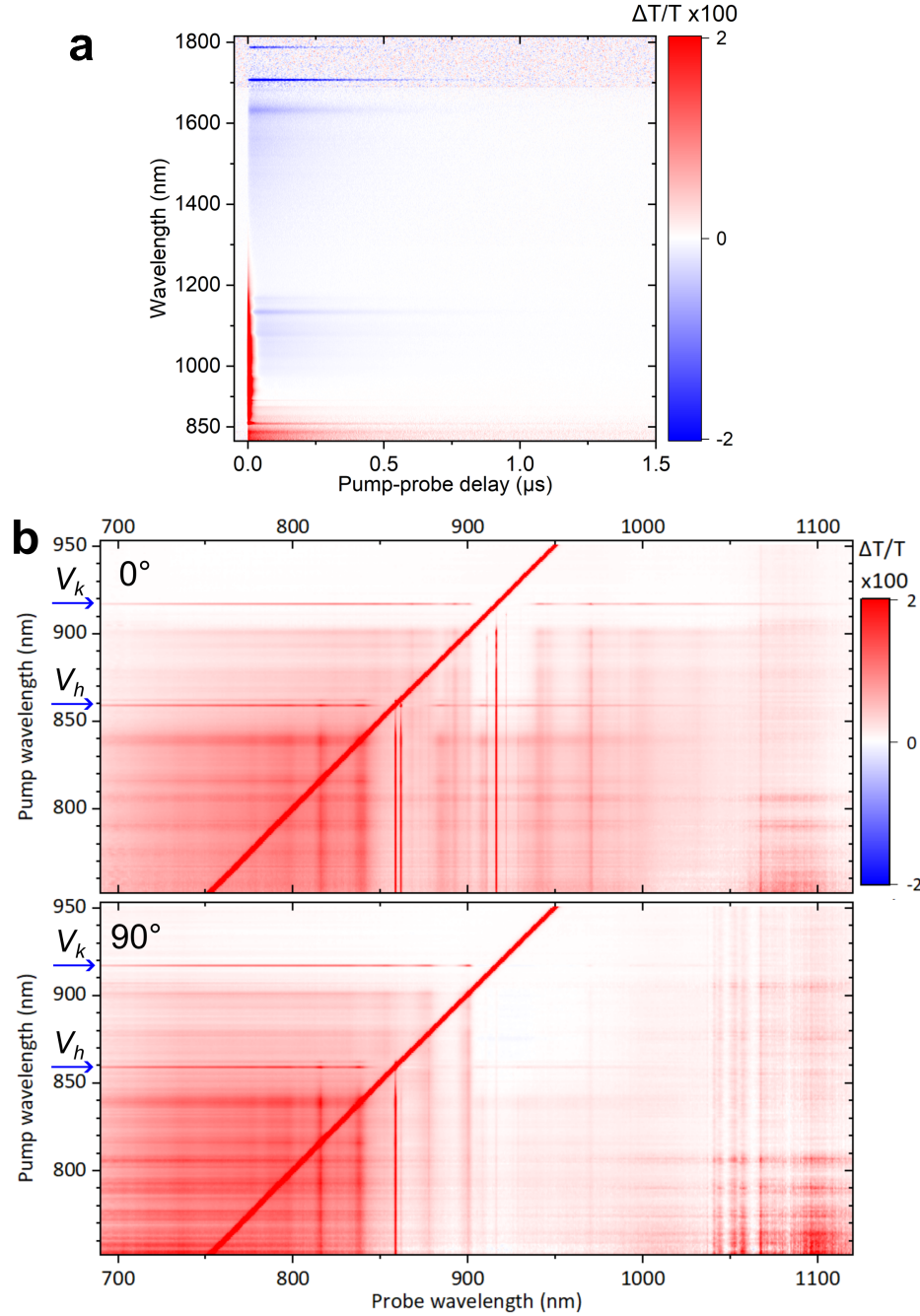


Figure S4. a) Temporal- and spectrally-resolved $\Delta T/T$ of V_{Si} in SiC pumped at 800 nm. b) shows $\Delta T/T$ spectra of V_{Si} while scanning the pump wavelength for 0° and 90° polarized probe, respectively. It is measured at a pump-probe delay of approximately 4 ns.

At energies higher than the ZPL of V_h ($E > 1.44$ eV, $\lambda < 860$ nm), there is increased transmission ($\Delta T/T > 0$), due to ground state bleaching (GSB), which resembles steady-state absorption. GSB arises from population transfer from the ground state to an excited state caused by pump excitation, leading to bleaching of the absorption. At energies lower than the ZPL ($E < 1.44$ eV, $\lambda > 860$ nm), a positive signal is observed ($\Delta T/T > 0$), which is attributed to stimulated emission (SE), spectrally resembling

photoluminescence (PL). Additionally, the contribution from the V_k excitation can be discerned. At energies higher than the ZPL ($E > 1.35$ eV, $\lambda < 916$ nm) GSB is observed, while at energies lower than the ZPL, SE is present. Negative signals in the TA spectrum ($\Delta T/T < 0$) generally originate from excited state absorption (ESA). Typically, this signal indicates the absorption from the first excited state (immediately from the pump) to another higher excited state. However, it is also indicative of the population dynamics between the spin-quartet and the spin-doublet channels. In this particular instance, the ESA signal observed in this spectral region originates from the population in the spin-doublet states, which are populated through ISC and possess a relatively long lifetime (approximately 200 ns). This is characterized by the delayed appearance of the ESA signal, whose rise time corresponds to the population transfer from the spin-quartet excited states to the spin-doublet states (or "upper ISC" lifetime). The decay of this ESA signal is thus the metastable lifetime of the spin-doublet channel before returning to the spin-quartet ground state ("lower ISC" lifetime). Therefore, the ESA signal time trace allows direct observation of the so-called spin polarization cycle of V_{Si}^- in 4H-SiC.

It is noteworthy that the data presented in Fig. S4-a contains the contributions from both V_h and V_k due to the excitation into their PSB. To differentiate between these features, the wavelength from the ns-OPO is scanned through the absorption range of V_h and V_k to excite them selectively. The $\Delta T/T$ spectrum while sweeping the pump wavelength at a pump-probe delay of approximately 4 ns is shown as a 2D contour in Fig. S4-b. Also, a probe polarization dependence was observed in these measurements, which is expected due to the optical selection rules discussed in the manuscript and the SI. The 2D spectrum (pump vs. probe wavelength) for the probe polarization rotated by 90° with respect to the previous case is plotted in the lower panel of Fig. S4-b.

S14 Photoexcitation dynamics of h-site vacancy V_h

The following spectra are obtained from the top panel of Fig. S4b (0°-polarized probe) and indicated with " V_h ". The GSB and SE spectrum of V_h , shown in Fig. 2-b (top panel), are fitted with Gaussian functions to determine the characteristics of the PSB. The fitted graphs are plotted in Fig. S5 and the fitting parameters are listed in Table S1. The separation between the two phonon lines is approximately $37(\pm 3)$ meV. The ZPL of V_1 (V_h) at 1.438 eV is also fitted separately with a Lorentzian function (see Section S19), with the fitting parameters listed in the table. Assuming an equal contribution of GSB and SE on the ZPL, and an equal contribution of both V_1 and V_1' (V_h), the Debye-Waller factor (DWF) is estimated to be 2.9 and 6.5 % for GSB and SE, respectively. The value for SE that corresponds to the DWF of PL value is close to previously reported values^{17,57}.

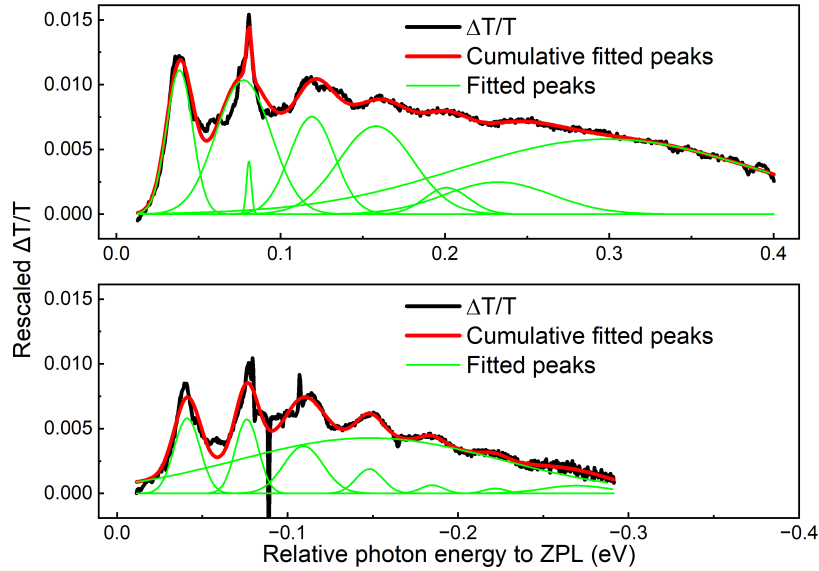


Figure S5. Fitting the GSB and SE of V_h in the top and bottom plot, respectively.

Following the excitation from the ground state 4A_2 , the electrons within the excited state $^4A'_2$, relax back to the ground state 4A_2 via two distinct mechanisms. The first pathway involves a radiative decay process, resulting in PL. The second pathway involves ISC through the intermediate doublet-spin states, which is non-radiative. The radiative relaxation lifetime is 6.6 ns, as demonstrated in Fig. S6-a. Conversely, the non-radiative decay process exhibits a longer duration before reaching the ground state. TA measurements provide direct access to the dynamics associated with this decay process, which is evident as absorptive transitions in the $\Delta T/T$ plot, the spectrum of which is shown in Fig. S6-b. The absorption signal in the plot indicates the occupation of the lowest spin-doublet state from which an excitation to higher spin-doublet states can occur. The plot exhibits two regions of absorption: one at 1708 nm (0.726 eV) with a narrow linewidth and several peaks with broader linewidths at higher

	Peak Index	Intg. area $\times 10000$	FWHM (meV)	Max height $\times 1000$	Center (meV)	Area ratio (%)
ZPL	0	0.9	0.7	87	0	2.9 (GSB), 6.49 (SE)
	1	2.21	19	11.1	38	8.0
	2	4.34	39	10.3	77	15.7
	3	0.15	3.5	4.1	81	0.6
	4	2.59	32	7.5	119	9.4
	5	3.87	54	6.8	158	14.0
	6	0.69	32	2.0	201	2.5
	7	2.03	77	205	232	7.3
	8	11.0	213	5.8	299	39.7
GSB	1	1.10	18	5.8	-41	8.8
	2	0.97	16	5.7	-76	7.8
	3	1.06	27	3.6	-109	8.5
	4	0.37	19	1.19	-148	3.0
	5	7.70	181	4.3	-148	61.9
	6	0.11	16	0.64	-185	0.9
	7	0.06	16	0.38	-222	0.5
	8	0.26	46	0.60	-269	2.1
SE	1	1.10	18	5.8	-41	8.8
	2	0.97	16	5.7	-76	7.8
	3	1.06	27	3.6	-109	8.5
	4	0.37	19	1.19	-148	3.0
	5	7.70	181	4.3	-148	61.9
	6	0.11	16	0.64	-185	0.9
	7	0.06	16	0.38	-222	0.5
	8	0.26	46	0.60	-269	2.1

Table S1. Fitting parameters of ZPL, GSB and SE features of V_h . Intg. area is the area under each fitted function. The area ratio is the ratio of the area under each peak to the entire sideband including ZPL.

energies. This observation suggests that the narrow peak at 1708 nm (0.726 eV) may correspond to a ZPL with its PSB located on the blue-shifted side. The other absorption feature contains two peaks around 1100 nm (1.13 eV).

As shown in Fig. S6c, the dynamics of these absorptive peaks and their fitting to a bi-exponential function are analogous, with a similar build-up within approximately 7 ns (upper ISC time) and a decay with a time constant of 220 ns (lower ISC time). The fitting parameters of these dynamics are listed in Table S2. The lower ISC lifetime measured here, around 220 ns, is in close agreement with previously reported values¹⁸. The GSB dynamics displayed in Fig. S6d can be fitted to a bi-exponential function, with the time constants shown in the legend. Like in the case of the doublet absorption transients, both time constants correspond to the upper and lower ISC time, respectively. The discrepancy between the PL lifetime and the GSB fast time constant of 8.8 ns can be attributed to the electronic artifacts near time-zero (see inset), which is the main source of error for either fits. The lifetimes of these states imply that the population of the excited spin-quartet state is either directly transferred to the lower spin-doublet state or indirectly via a rapid decay from a higher spin-doublet state. A similar phenomenon to the latter case has been observed in nitrogen-vacancy centers in diamond²¹. However, due to the temporal resolution limitations of the ns- μ s TA setup and the possibility of fast decay times (below a nanosecond), the distinction between these two processes remains unresolved.

Wavelength (nm)	Energy (eV)	A_1	A_2	τ_1 (ns)	τ_2 (ns)
1132	1.095	0.649	-0.801	7.2	221.4
1632	0.760	0.841	-1.00	7.1	218.9
1684	0.736	0.467	-0.636	6.5	221
1708	0.726	4.105	-4.831	7	244

Table S2. The parameters of fitting $\Delta T/T$ data at various wavelengths with a bi-exponential function with the following equation: $A_1 \exp(-t/\tau_1) + A_2 \exp(-t/\tau_2)$.

The ISC process can be confirmed by measuring the GSB signal that is measured in the ground spin-quartet state, 4A_2 . The GSB signal is fitted with a bi-exponential function, with time constants of 8.8 and 205 ns as illustrated in Fig. S6-d. The extracted lifetimes are in close agreement with the lifetimes reported in Table S2. This outcome validates the hypothesis that the lower spin-doublet state decays back to the ground spin-quartet state within its lifetime.

S15 Photoexcitation dynamics of k-site vacancy V_k

The following spectra are obtained from the top panel of Fig. S4b (0°-polarized probe) and indicated with "V_k". The PSB of V_k on both the GSB and SE sides are shown in Fig. S7. The shape of the PSB of V_k is observed to depend on the polarization

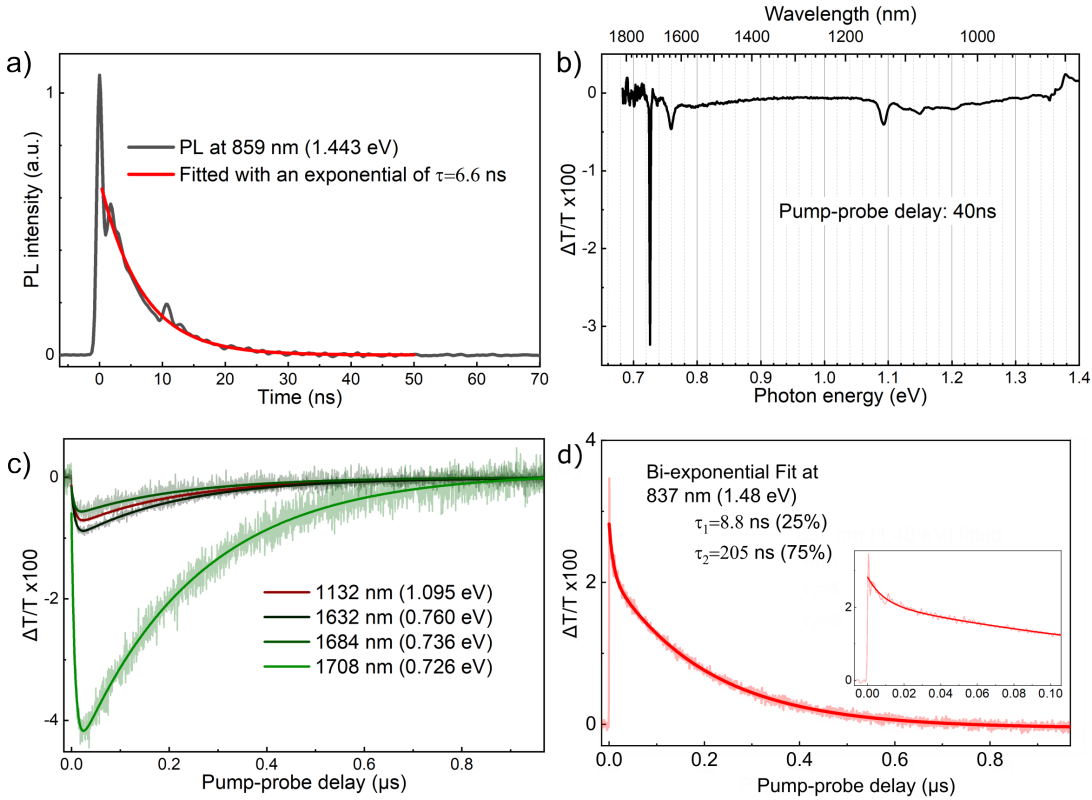


Figure S6. a) The PL decay of V_h fitted with an exponential function with a lifetime of 6.6 ns. b) The absorptive features from the lower spin-doublet states to the higher ones of V_h measured at 40 ns pump-probe delay. c) Dynamics of the absorption from the spin-doublet states indicating the ISC processes fitted with bi-exponential functions d) the GSB dynamics of V_h fitted with a bi-exponential function comprising lifetimes of 8.8 and 205 ns. The percentages indicate the relative amplitude of each exponential component. Inset highlights the electronic signal artifact within the first ~10 ns.

of the probe beam. As the polarization of the probe beam is rotated from 0° to 90° , a significant decrease in the SE is observed (consistent with the drop in V2 ZPL absorption signal), accompanied by a change in the shape of the GSB and the disappearance of some side peaks. The 90° -polarized data is then taken as a single contribution, and subtracted from the 0° -polarized data with proper rescaling. The rescaling factor was determined by eye to ensure that the subtracted data excluded the peaks present in the 90° -polarized spectrum. The result of this subtraction is plotted in Fig. 2-c. Hereafter, the term "0°-polarized only" data will be used to denote the subtraction result. The GSB feature for both 90° - and 0° -polarized are fitted with Gaussian functions and plotted in Fig. S7-a and b, respectively. The SE for 0° -polarized is also fitted with Gaussian peaks and shown in Fig. S7-c. The SE for 90° -polarized is not analyzed because of its low intensity. The parameters of the fittings are listed in Table S3. The ZPL of V2 (V_k) at 1.353 eV is fitted with a Lorentzian function when the sample is pumped at the sideband (880 nm), and the parameters are listed in the table. In this calculation, the signal is rescaled to have a similar area to the ZPL-pumped case (Fig. S7). However, due to complications of different polarization and different contributions between the GSB and SE, the ZPL area is not considered in the area ratio value.

The photoexcitation dynamics of V_k are analogous to those of V_h , wherein the pump excites the electrons from the ground to the excited spin-quartet states ($^4A_2 \rightarrow ^4A_2$). The electrons in the excited state either decay back to the ground state through either PL or a non-radiative channel via ISC to the spin-doublet states. The excited state lifetime, as determined through PL signal fitting, is estimated to be approximately 7.1 ns, as illustrated in Fig. S8-a. Similar to V_h , absorptive features corresponding to the ISC and spin-doublet states absorption are observed. They are considered to be the absorption from the lower to higher spin-doublet states. The $\Delta T/T$ spectrum showing this feature is illustrated in Fig. S8-b. These features look almost identical to V_h with shifted energies. The graph reveals two distinct peak sets: one at approximately 1778 nm (0.694 eV) with a narrow linewidth, suggesting a ZPL of a transition accompanied by its PSB with higher energies from the lowest populated spin-doublet state to the intermediate spin-doublet state; and another at about 1160 nm (1.065 eV) with a broader linewidth than the previous one. Additionally, there are several lower-energy peaks, which are presumed to be the PSB of this transition. In contrast to the V_h case, the latter absorptive feature exhibits two peaks separated by 10 meV (peaks at 1.071 and 1.061 eV). The dynamics of the absorptive features are plotted in Fig. S8-c.

The dynamics of two absorptive peaks at 1158 nm (1.071 eV) and 1778 nm (0.697 eV), along with their fittings with bi-

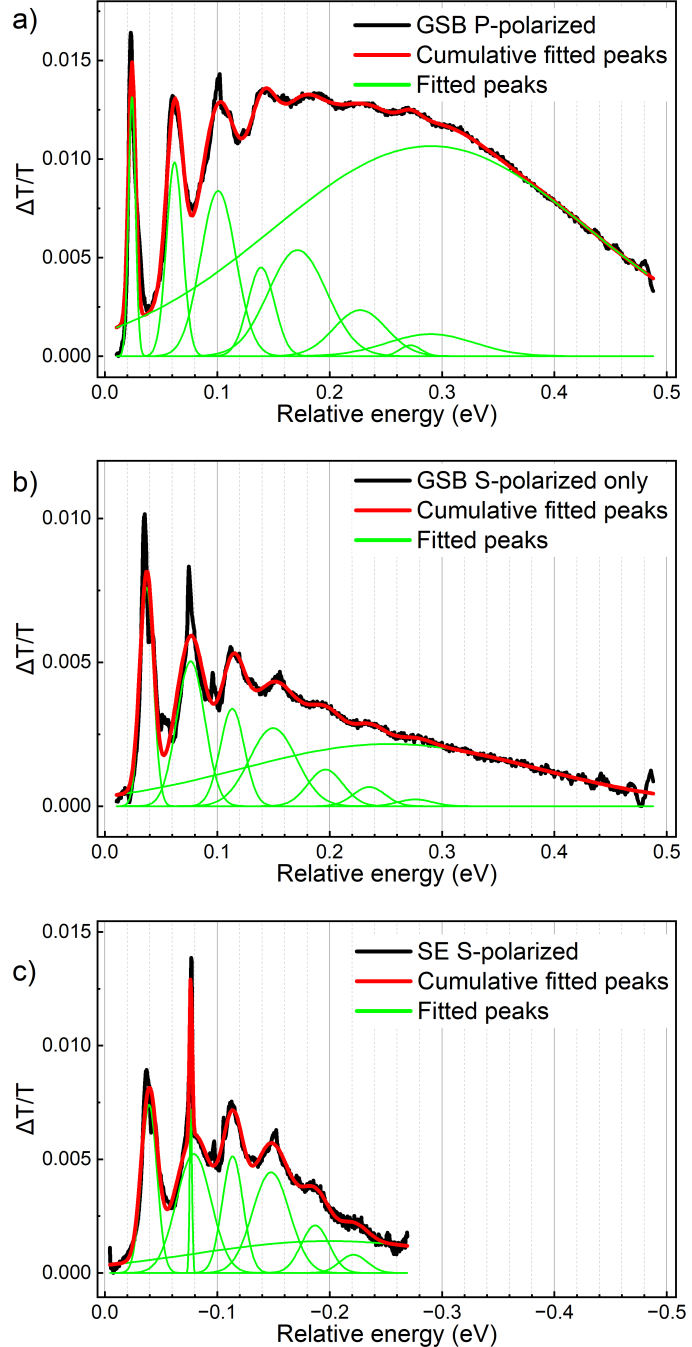


Figure S7. Fitting the PSB (GSB and SE) of V_k for various conditions: a) GSB with 90°-polarized probe; b) GSB with 0°-polarized only probe (subtracted signal as explained in the text); and c) SE for 0°-polarized probe.

exponential functions are plotted in Fig. S8-c. The fitting parameters are listed in Table S4. The absorption builds up with a lifetime similar to the excited spin-quartet state lifetime, around 8 ns, representing the populating of the ground doublet state via ISC from the excited spin-quartet state. The absorption lasts around 165 ns, which is the lifetime of the lower spin-doublet state, which decays back to the ground spin-quartet state via ISC. It is noteworthy that the lifetimes observed here are of the same order as the V_h ISC lifetimes.

As illustrated in Fig. S8-d, the GSB of V_k is fitted with a bi-exponential function, comprising two lifetimes: 7.8 and 154 ns. The fast component corresponds to the lifetime of the spin-quartet excited state, as substantiated by the PL lifetime. Similarly to the V_h case, the difference between the measured PL and GSB lifetimes are due to the instrumental error near time-zero by the large signal artifact. The longer component is the relaxation time of the spin-doublet states to the ground spin-quartet state via

	Peak Index	Intg. area $\times 10000$	FWHM (meV)	Max height $\times 1000$	Center (meV)	Area ratio (%)
GSB-90°	1	1.02	7.3	13.1	25	2.2
	2	1.77	17	9.8	62	3.8
	3	3.28	37	8.4	101	7.0
	4	1.33	28	4.5	139	2.8
	5	3.51	61	5.4	171	7.4
	6	1.37	55	201.0	227	2.5
	7	1.32	22	0.56	272	0.3
	8	1.09	91	1.1	290	2.3
	9	34.0	331	10.7	290	71.4
GSB-0°	1	1.31	14	7.6	37	9.0
	2	1.57	29	5.0	76	12.6
	3	0.92	26	3.4	113	7.4
	4	1.43	49	2.7	150	11.4
	5	0.50	37	1.3	196	4.0
	6	0.24	34	0.67	235	1.9
	7	6.63	310	2.2	253	53.4
	8	0.24	36	0.24	276	0.7
SE-0°	1	1.27	16	7.4	-39	12.5
	2	0.20	2.6	7.2	-77	1.9
	3	2.03	37	5.2	-79	20.0
	4	1.19	22	5.1	-114	11.6
	5	1.83	39	4.4	-148	17.9
	6	0.65	29	2.1	-187	6.3
	7	2.80	281	1.4	-200	27.4
	8	0.25	29	0.8	-221	2.4
ZPL-0°	0	0.81	0.7	87.0	0.0	–

Table S3. Fitting parameters of GSB (for both 90°-polarized and 0°-polarized only, labeled as GSB-90° and GSB-0°, respectively), and SE (for 0°-polarized probe) of V_k . The ZPL for 0°-polarized probe (ZPL-0°) is also fitted while the sample is pumped at the sideband and rescaled accordingly. Intg. area is the area under each fitted function. The area percentage is the ratio of each peak to the entire sideband excluding ZPL area.

Wavelength (nm)	Energy (eV)	A_1	A_2	τ_1 (ns)	τ_2 (ns)
1158	1.071	0.299	-0.407	7.8	168.1
1778	0.697	1.646	-1.972	9.4	160.2

Table S4. The parameters of fitting $\Delta T/T$ data at various wavelengths with a bi-exponential function with the following equation: $A_1 \exp(-t/\tau_1) + A_2 \exp(-t/\tau_2)$.

ISC.

S16 V2' PSB characterization and analysis

In the oblique incidence case, exciting the V2' will also excite the V2 transition (would require polarization control of the pump pulse otherwise). To obtain a clean absorption spectrum of V2', we perform a TA measurement pumping selectively at the V2' ZPL at 1.38 eV with the probe beam entering with the normal incidence case. Here, the probe only interacts with transitions allowed by μ_x and μ_y , thereby eliminating the response of V1 and V2. Furthermore, pumping below the ZPL of V1' (1.43 eV) eliminates the contribution of V1' to the spectrum, hence only the response of V2' will be observed with the probe.

Unfortunately, the TA spectrum is susceptible to the pump scattering at the excitation wavelength. Thus, at the ZPL wavelength (and any spectral position of the pump), the spectrum has an artifact that cannot be filtered out. In order to obtain a spectrum of the V2' with both the ZPL and PSB, we take a spectrum pumped at the ZPL, then another spectrum pumped at the 1-phonon line. The resultant spectrum uses the data at the ZPL in the 1-phonon pump case, and the data at 1-phonon peak comes from the

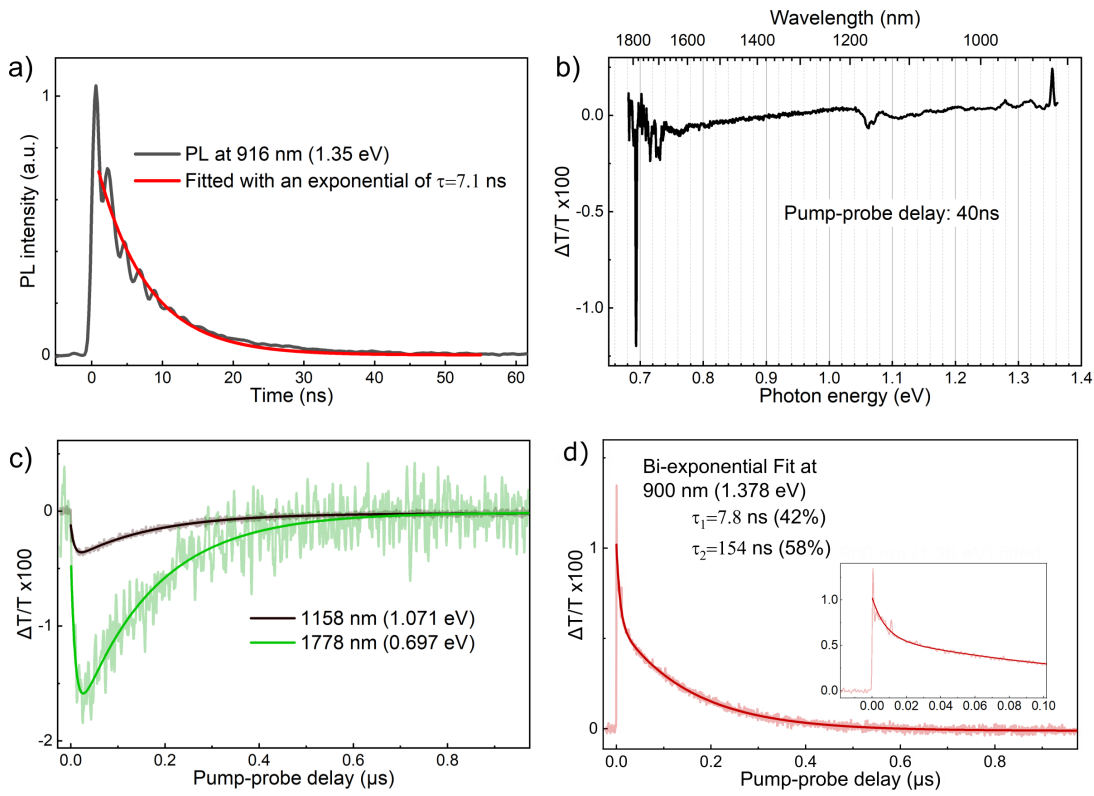


Figure S8. a) The PL decay of V_k fitted with an exponential function with a lifetime of 7.1 ns. b) The absorptive features from the lower spin-doublet states to the higher ones of V_k measured at 40 ns pump-probe delay. c) Dynamics of the absorption from the spin-doublet states, representing the ISC processes fitted with bi-exponential functions. d) The GSB dynamic of V_k fitted with a bi-exponential function comprising lifetimes of 7.8 and 154 ns. The percentages indicate the relative amplitude of each exponential component. Inset highlights the signal artifact within the first ~ 10 ns.

ZPL pump case. The rest of the spectrum is the averaged spectrum of the two cases. It is noted that the absorption cross-sections of the $V2'$ ZPL and its 1-phonon peak are comparable from the SETA measurements (Fig. S4). A FFT lowpass filter was also applied to the spectrum to remove interference artifacts due to the thin sample.

A 9-peak model was used, where the first peak is a Lorentzian fit to the expected ZPL, while the rest of the peaks are Gaussian fits to model the response of vibronic modes. The overall fit result is shown in Fig. S9. The response shows a rather intricate

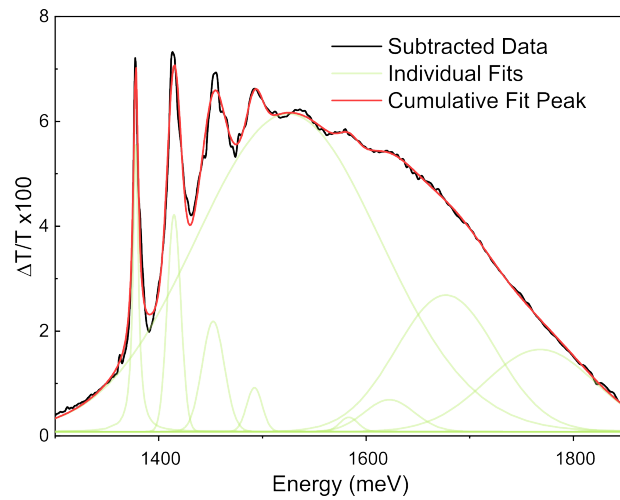


Figure S9. $V2'$ GSB spectrum obtained from selective pumping at normal incidence. Parameters detailed in Table S16.

Peak Index	Peak Type	Area Intg x10000	FWHM (meV)	Center Energy (eV)	Area (%)
1	Lorentz	5.17	6.08	1.378	2.46
2	Gaussian	6.70	15.2	1.415	3.19
3	Gaussian	5.64	25.2	1.452	2.68
4	Gaussian	1.57	17.6	1.492	0.750
5	Gaussian	135	209	1.525	64.2
6	Gaussian	0.60	20.7	1.583	0.287
7	Gaussian	3.67	56.6	1.622	1.75
8	Gaussian	31.3	113	1.677	14.9
9	Gaussian	20.6	124	1.768	9.78

Table S5. Fitting parameters of the V2' GSB spectrum as shown in Fig. S9.

structure, with a rather large red onset of the ZPL response and a sharp response at 121 meV, indicating a local vibrational mode (LVM) at higher energy than the LO phonon mode of 4H-SiC at 119 meV. The red onset is modeled by a broad peak, serving similarly to a baseline for the first 4 peaks within the first replica regime. The peaks at higher energy than this broad peak models the second replica regime of the phonon modes which are much more broadened than their first replica counterparts.

S17 Polarization dependence of the spin-doublet transitions

In this Section, we provide an analysis of the polarization-dependent spectra of the spin-doublet transitions, which were shown in Fig. 4 of the main manuscript. For either h- or k-site, we model the transition from the lower spin-doublet 2T_1 to the splitting of the upper spin-doublet 2E and 2A_1 (from 2T_2) with two Lorentzian peaks and fit the model to the experimental data. To condition for the fitting, the background signal not contributing to the peaks are subtracted from the data.

V_h	Integrated Area x10000 (a.u.)		FWHM (meV)		Center Energy (meV)	Area Ratio (%)	
	0°	90°	0°	90°		0°	90°
	Peak 1	2.8	1.9	7.2	4.6	1091	63 26
Peak 2	1.6	5.3	6.4	6.4	1095	37 74	

Table S6. Fitting parameters of the D^2 transitions of the V_h center with 0°-polarized and 90°-polarized probe light. The curves are shown in Fig. S10a.

V_k	Integrated Area x10000 (a.u.)		FWHM (meV)		Center Energy (meV)	Area Ratio (%)	
	0°	90°	0°	90°		0°	90°
Peak 1	5.7	1.9	9.6	9.7	1061	86 49	
Peak 2	0.9	1.9	5.8	6.6	1071	14 51	

Table S7. Fitting parameters of the D^2 transitions of the V_k center with 0°-polarized and 90°-polarized light. The curves are shown in Fig. S10b.

The fit results are shown in Fig. S10 for both V_h and V_k cases and summarized numerically in Table S6 for V_h and Table S7 for V_k . While the two peaks are rather well-separated spectrally in the V_k case, the V_h case is not as clear. This is largely because the linewidth (in FWHM) of the doublet transitions are in the 6-8 meV range even at 5 K and therefore a resolution of two peaks separated by less than ~5 meV is less reliable. However, the two-peak model for V_h can still yield the relative strength of two transitions and approximate the 2T_2 splitting. We notice a similarity in the behavior of the relative peak strength in either V_h or V_k shifting from the lower energy peak to the higher energy peak when the polarization is changed from 0° to 90°. We interpret this observation as the lower-energy peak (Peak 1) representing the C transitions with the μ_z component and the higher-energy peak (Peak 2) representing the B transitions with μ_x and μ_y components. As the polarization is switched to 90°, the probe no longer

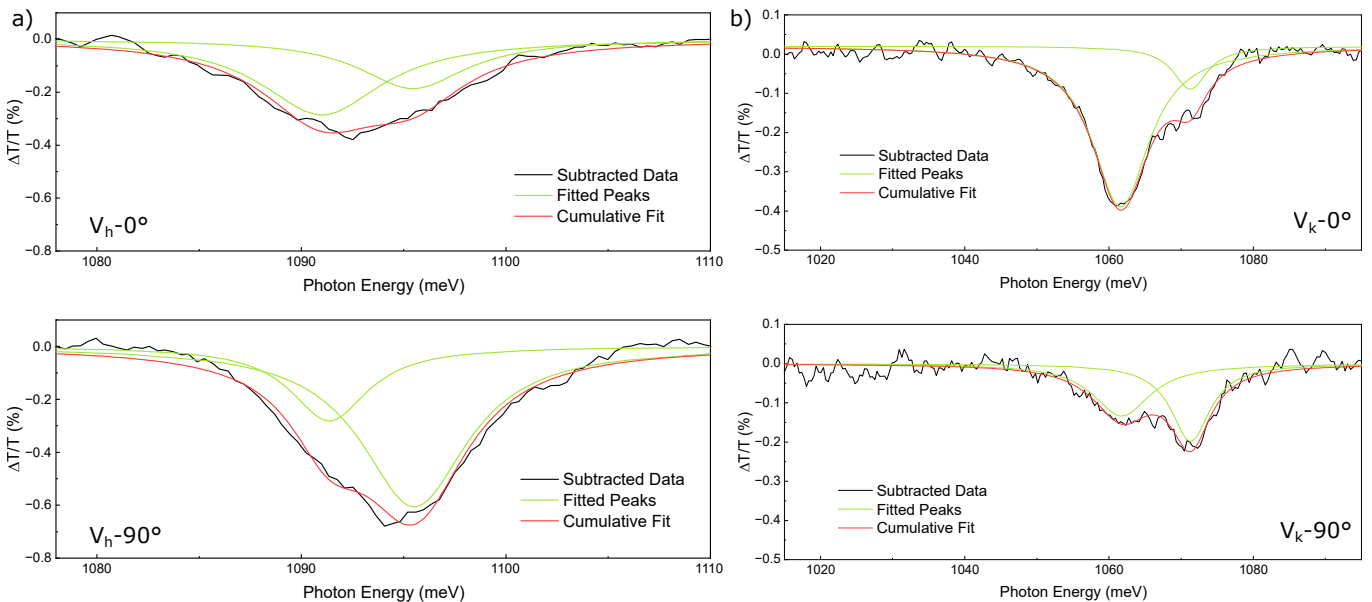


Figure S10. Lorentzian fitting of the spin-doublet transitions in either 0°-polarization or 90°-polarization cases: a) V_h site; b) V_k site.

probes the μ_z component and instead couples to μ_y , shifting the signal towards Peak 2. From this, we conclude that ordering of the upper orbital-triplet splitting (2T_2) as illustrated in Fig. 4c in the main text from the assignment of the B and C transitions in both V_h and V_k .

S18 Temperature dependence of spin-doublet transitions

As shown in Fig. S11, a temperature dependence measurement was carried out in the normal incidence configuration primarily to determine the splitting energy of the lower doublet 2T_1 , which we will call κ . The normal incidence configuration eliminates the spectral contribution of the C transition, and thus only A and B transitions are expected (transition names shown in Fig. 4). We observed transitions at 1071 meV and 1095 meV (Fig. S11a), which are attributed to either A or B transitions in h- and k-sites, respectively. These transitions do not exhibit any substantial spectral shift or clear new spectral feature with increasing temperature, only slight red shifts of these transitions. This is further made difficult by the linewidth of these transitions, which is about 6-8 meV (FWHM) and increases with temperature. While it is possible to analyze the slight peak shifts by considering the spectral shift of the area under curve to determine κ , this is complicated by the dependence of the relative oscillator strength between the A and B transitions. Other temperature-related effects such as thermal expansion of bulk SiC and electron-phonon coupling will also contribute to the spectral shift (as observed in the NV center in diamond^{21,58}).

Despite such complications, we can still make a few observations about the splitting of the 2T_1 states. The insensitivity to temperature dependence implies two possible scenarios:

- κ is small (sub-1 meV): population in the 2A_2 and 2E states are already approximately equal at 5 K, thus increasing temperature does not change the population in either states.
- κ is large (> 10 meV): population in the upper state cannot be thermally occupied significantly at 5 K and elevated temperatures. From the polarization dependence measurements (Fig. 4) in the main text, this case is only valid if 2E is the lower energy state due to the sensitivity to the μ_z transition dipole at 5 K.

From the temperature dependence results here and the results observed in the polarization dependence measurements, the transitions at 1071 meV and 1095 meV are attributed tentatively to the B transitions in h- or k-sites, as they signify the population from the 2E , sharing the same lowest state as the C transitions.

While a $\kappa < 1$ meV splitting cannot be verified experimentally due to the linewidth of these transitions, we can explore the possibility that the splitting is > 10 meV by spectrally identifying transition A and F. From Fig. 4c, the energy for the transition A would be $E_A = E_B - (\kappa + \eta)$, or a spectral red-shift from the B transitions. Therefore, the expected spectral shift would be $>\sim 14$ meV and $>\sim 20$ meV for V_h and V_k , respectively. Transition F red-shift would simply be the κ splitting. In the case of V_h that means:

- Transition A: In Fig. S11, there is a region in between 1075-1085 meV that has a rise in signal as the temperature is increased. One may interpret this rise in signal as thermal populating of the 2A_2 , thereby suggesting that the κ splitting is

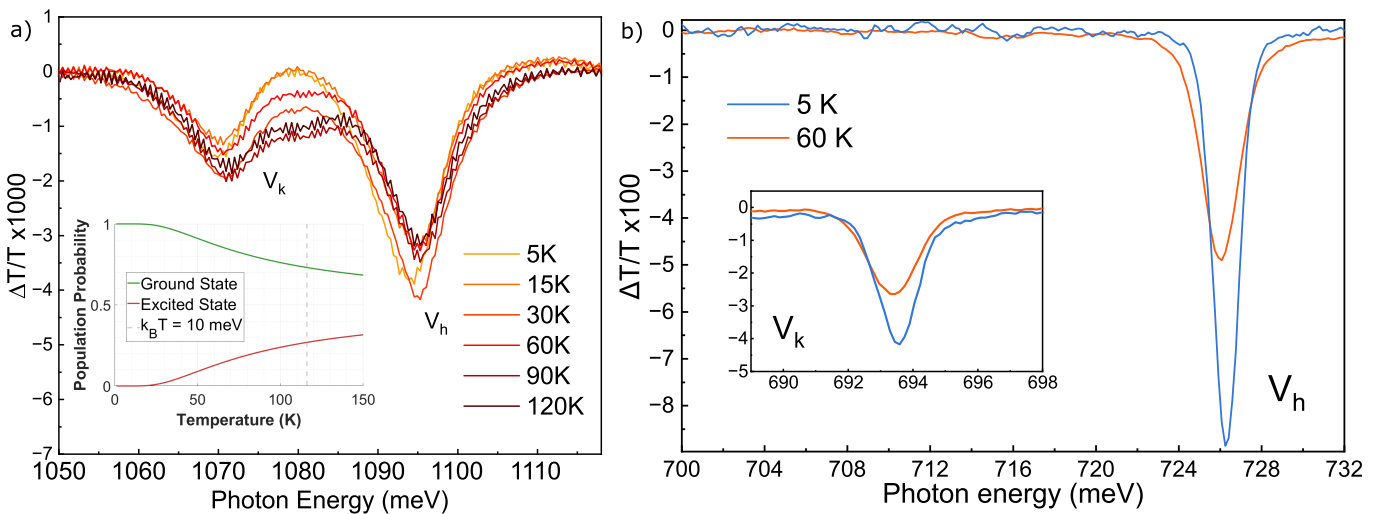


Figure S11. a) Spectra of the A transition in either h- or k-sites in the normal incidence case with temperature between 5 K and 120 K. Inset shows the population probability of a two-level system separated by 10 meV in energy against temperature using a Boltzmann distribution model. b) Spectral comparison of the E transitions at 5 K and 60 K. Obtained with oblique incidence configuration with mixed 0°- and 90°-polarized light.

~ 10 meV. A simple Boltzmann factor model of a two-level system separated by 10 meV (see the inset of Fig. S11a) also predicts a similar pattern to the signal rise: the signal onset is around 30 K and saturates at around 100 K. Unfortunately, the signal observed here could also simply arise from the broadening of the B transitions. Without precise parameters regarding the oscillator strength of the A transitions, it is not possible to discern the two possibilities in this case.

- Transition F: Following the observations for transition A, one would expect a resonance to appear at about 716 meV (10 meV red-shifted). However, there is a complete lack of any other spectral feature at elevated temperature (Fig. S11b) in this region. It is also possible that while the 2A_2 can be thermally populated, the F transition may be too weak to be observed.

In the case of V_k , there is no observable red-shifted spectral feature until the spectral cutoff of our measurement at 690 meV. This can once again point to a splitting too large to be thermally populated. While there are some arguments supporting $\kappa > 10$ meV (at least in V_h) from the A transition, the lack of evidence in the F transition renders this hypothesis inconclusive. A splitting much larger than this value is also not supported by the crystal field splittings observed in other states. Nevertheless, we could not rule out the possibility that the κ is in the 10-30 meV range for either V_h or V_k from the data obtained here and would likely require a different spectroscopy technique to determine this splitting.

S19 ZPL characteristics of the spin-doublet and spin-quartet transitions

The fitting and analysis of the V1, V1', V2 (and its splittings) and the D¹ transitions are presented in Fig. S12. The spectra for the spin-quartet transitions are taken from Fig. S4b taken at non-resonant pumping wavelength (840 nm/1.476 eV for V1/V1' and 880 nm for V2); The spectra for D¹ transitions are taken from the data presented in Fig. 4d and e. Combined with the data already analyzed and presented in previous sections, Table S8 summarizes the linewidth properties and lineshape functions used to determine the profile of the ZPLs. The values for the V2' line is taken from Table S16 and the D² lines from Tables S6 and S7. The uncertainties given for the D² lines reflect the multiple transitions arising from the splitting of the 2T_2 (and potentially 2T_1 states). Figure S13 is a graphical representation of the linewidth values shown in Table S8, highlighting the clear broad (~ 5.5 -10 meV) and sharp (~ 0.7 -1.5 meV) linewidth regimes of these ZPLs.

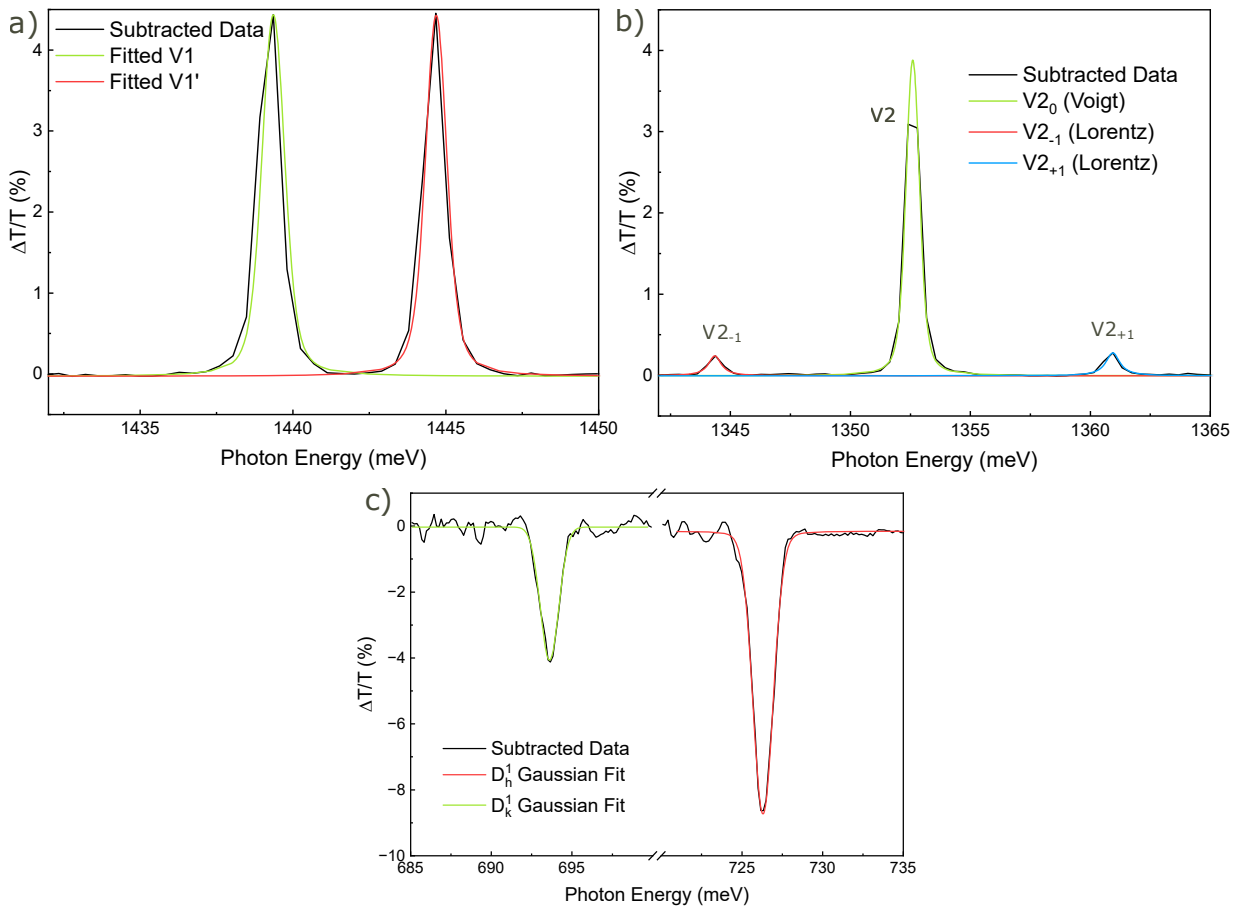


Figure S12. Peak Fitting of the ZPLs: a) V1 and V1'; b) V2 (center) and the two unknown splittings. c) D¹ transitions.

Ideally, ZPL profiles are within the homogeneous broadening limit at cryogenic temperature (5 K). Deviation from this model gives information on whether inhomogeneous broadening processes are involved, or whether that is simply caused by instrumental limitations. In our case, the limitation is mainly the spectral resolution of the monochromator in the ns- μ s setup. This method can also be used as a tool to determine whether the optical transition observed is a ZPL (Lorentzian profile) or a vibronic mode of the PSB (Gaussian profile) - see Section S6 for a theoretical description. This was employed to determine the nature of the V2' line as a ZPL instead of a LVM peak, as demonstrated in Section S16, since Gaussian fit could not produce a solution to fit the ZPL of the V2' line.

In Table S8, we list the center energies, linewidths and lineshapes of all ZPLs in both quartet and doublet channels. We attribute the Gaussian lineshapes of the D¹ transitions to the spectral resolution of the monochromator that is used in the ns-ms setup. In this case, the "broadening" is most likely due to instrumental response rather than an inhomogeneous broadening process. The broader lineshapes of D² transitions, however, all have Lorentzian characteristics, suggesting being dominated by homogeneous broadening.

Transition Name	Center Energy (meV)	FWHM (meV)	Fit Type
V1	1439	0.9	Lorentz
V1'	1444	0.8	Lorentz
V2 ₀	1353	0.7	Lorentz
V2 ₋₁	1344	0.7	Lorentz
V2 ₊₁	1361	0.7	Lorentz
V2'	1378	6.1	Lorentz
D _h ¹	726	1.5	Gaussian
D _k ¹	694	1.4	Gaussian
D _h ²	1095	6.2 ± 0.5	Lorentz
D _k ¹	1065	7.9 ± 1.8	Lorentz

Table S8. Summary of the linewidth of the ZPLs for all observed transitions presented in Fig. S13.

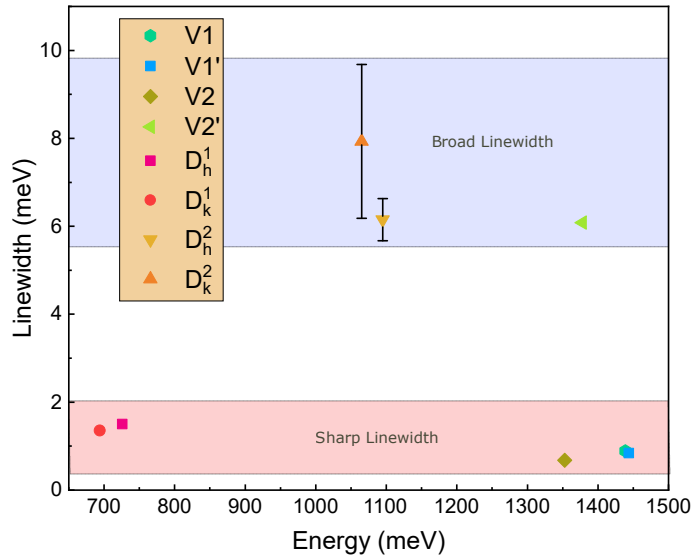


Figure S13. Linewidths of the ZPLs of all transitions observed in the spin-quartet and spin-doublet transitions. The error bars represent the FWHM distribution of D² transitions from all measurements instead of peak fitting error.

S20 Calculated emission and absorption spectra of V_{Si}^-

Figure S14 shows the calculated normalized emission (${}^4A'_2 \rightarrow {}^4A_2$) and absorption (${}^4A_2 \rightarrow {}^4A'_2$) lineshapes for $V_{\text{Si}}^-(h)$ and $V_{\text{Si}}^-(k)$ defects, with the horizontal axis shifted relative to the respective V1 and V2 ZPL values. The inset figures contain the calculated spectral functions of electron–phonon coupling $S(\hbar\omega)$ together with the total electron–phonon coupling strength S_{tot} . Lineshapes were computed with the $r^2\text{SCAN}$ meta-GGA functional using HR theory (described in Sec. S6) excluding the vibronic coupling between different components of the excited state and then extrapolated to the dilute limit using embedding methodology for size-effects (described in Supplementary Note S7).

The calculated emission lineshapes are in strong agreement with the experiment, capturing the fine features in the PSB. Specifically, the double-peak feature associated with quasi-local vibrational modes for $V_{\text{Si}}^-(h)$, observed at (74.0, 76.4) meV below the V1 ZPL, and the double-peak feature arising from bulk-like vibrational modes for $V_{\text{Si}}^-(k)$ at (36.2, 42.0) meV below V2 ZPL are reproduced due to the large number of vibrational modes obtained using embedding methodology for size-effects.

The ${}^4A_2 \rightarrow {}^4A'_2$ absorption lineshape which was calculated for $V_{\text{Si}}^-(h)$ configuration reproduces nearly all experimentally observed vibronic features (blue shaded area in Fig. S14b). The remaining spectral broadening can be attributed to the presence of a second ZPL located approximately 5 meV higher in energy. This effect is illustrated by an additional absorption lineshape obtained by rigidly shifting the calculated ${}^4A_2 \rightarrow {}^4A'_2$ spectrum by 5 meV to the V1' ZPL energy (dashed blue line in Fig. S14b). The reproduction of nearly all observed PSB features by adiabatic HR theory implies that non-adiabatic Jahn–Teller coupling within the 4E manifold and between the ${}^4A'_2$ and 4E states is not dominant.

For the $V_{\text{Si}}^-(k)$ configuration the calculated ${}^4A_2 \rightarrow {}^4A'_2$ absorption lineshape (blue shaded area in Fig. S14d) does not capture several PSB features seen in the experiment, especially the feature 25 meV above the V2 ZPL. This feature is theoretically predicted to be V2' ZPL¹⁷. An additional absorption contribution is included by rigidly shifting the calculated V2 absorption lineshape by 25 meV (dashed blue line in Fig. S14d). The resulting superposition reproduces several additional PSB features, suggesting that overlapping absorption from two transitions may contribute to the observed spectrum. The anomalous linewidth of the V2' ZPL can be understood as arising from resonant coupling between the nominal zero-phonon state of the 4E manifold and a dense manifold of vibronic states associated with the ${}^4A'_2$ configuration. The V2' ZPL lies within an energy range that overlaps with the energy range of the first vacancy-related vibrational resonance (the first PSB peak at 35 meV). Consequently, the oscillator strength is redistributed over many closely spaced vibronic states, leading to an effective broadening of the ZPL.

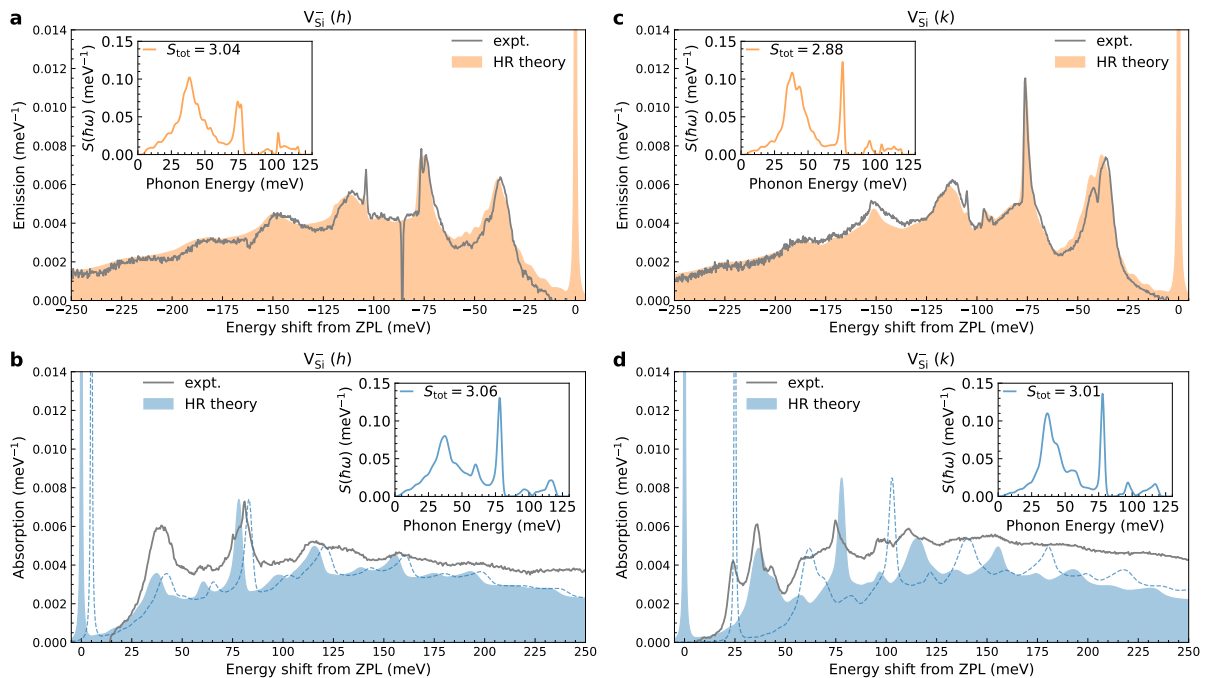


Figure S14. Calculated PSB of V1 and V2 in emission (orange-shaded) and absorption (blue-shaded) lineshapes for unstrained (6 x 6 x 2) size supercells with $V_{\text{Si}}^-(h)$ and $V_{\text{Si}}^-(k)$ defects. The inset figures contain the calculated spectral functions of electron–phonon coupling. The intensities of the experimental lineshapes have been scaled to match the peaks of the computed lineshapes. Lineshapes were computed with $r^2\text{SCAN}$ functional using HR theory and extrapolated to the dilute limit, approximated by a (25 x 25 x 8) supercell with 40 000 atomic sites.

S21 Quantum embedding results

First, spin polarized DFT was used to relax the geometry until the maximal force (acting on any ion) was smaller than 10 meV/Å.

We tested both regular semi-local DFT using the Perdew-Bruke-Ernzerhof (PBE) functional⁵⁹ exchange correlation functional as well as the the hybrid Heyd-Scuseria-Ernzerhof HSE06 functional⁶⁰. The plane wave cutoff was 520 eV and the Brillouin zone was sampled with the zone center only. The lattice parameters are given in Tab. S9. The computations were performed on a 128-atom supercell.

a. *Electronic structure at the semi-local DFT level (PBE):* The ground state of $V_{Si,k}^{-1}$ exhibits spin 3/2. The α spin-channel contains 3 additional electrons in comparison with the β channel (Figure S15a). These states are localized as given by the inverse participation ratio (IPR) (Figure S15b). In the β spin-channel there are 3 unoccupied states that are localized.

Table S9. Lattice parameters for the considered computational unit cells.

	a (Å)	b (Å)
PBE	3.09	10.13
HSE06	3.07	10.05

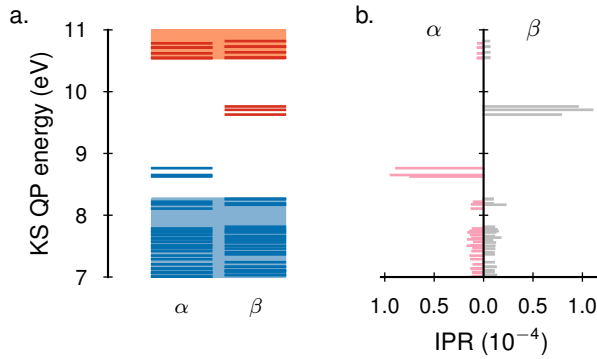


Figure S15. (a) Kohn-Sham (KS) quasi-particle energies and (b) corresponding inverse participation ratio (IPR) at the level of semi-local DFT.

The initial state was obtained by spin pairing the system. The spin-pairing forces the occupied α -channel states up in energy and the corresponding empty β -channel states down in energy (Figure S16). There are 3 electrons that populate these quasi-degenerate states with unequal occupation factors. With very low electronic smearing (0.005 eV), the population of the in-gap states is such that the lowest populated in-gap state at 9.12 eV contains 2 electrons and the state at 9.14 eV contains a single electron and the state at 9.23 eV is empty at the PBE level. Together with a low lying fully occupied state, these states make up the active space (Figure S16).

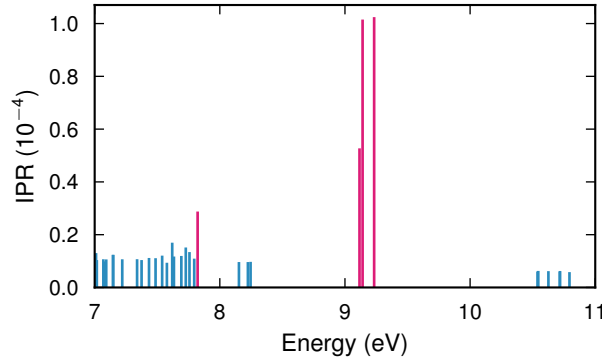


Figure S16. Inverse participation ratio (IPR) for the spin paired (spin 0) calculation. The active space states are indicated with magenta and the environment with blue color.

The active space is chosen such that states with IPR above 0.2 are included. There are 4 spatial states in total, and Wannier functions corresponding to these states are constructed using sp^3 projectors on the neighbouring C atoms. The spread of the Wannier functions ranges between 4.0 Å and 4.2 Å. The resulting Wannier functions are shown in Figure S17. The imaginary part is negligible.

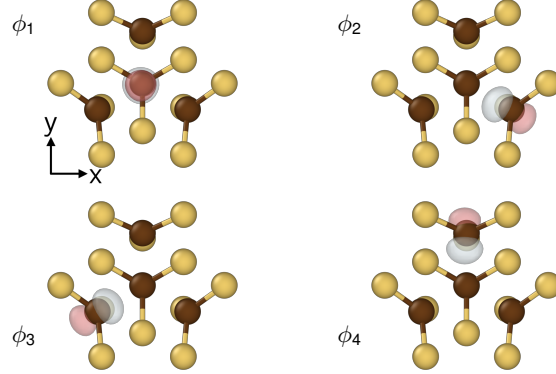


Figure S17. The single particle basis $\{\phi\}$ for the embedding.

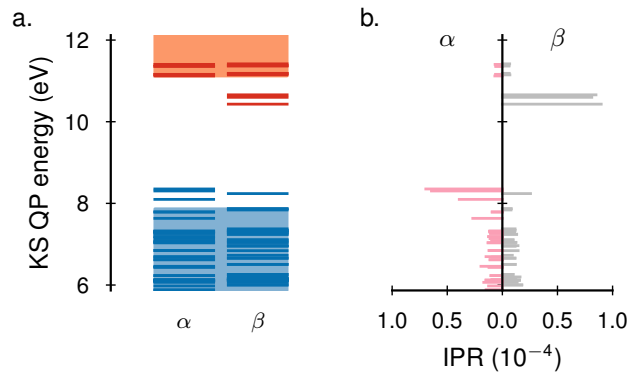


Figure S18. Kohn-Sham eigenstates using the HSE06 exchange functional.

For the constrained random phase approximation, we consider 1120 bands in total in the cRPA calculation for the 128 atom supercell, which is 32 eV above the conduction band minimum. The resulting interaction parameters are tabulated in Table S10. At the level of semi-local DFT on the negatively charged silicon vacancy in the k site, the many-body states are tabulated in Table S11 and shown in Figure S19.

The current data (PBE, 128 atom supercell, FCI+cRPA) would give possible transition energies in the doublet manifold (from the ground state) of 0.86, 0.75, 0.72, 0.52, and 0.46 eV.

Using the HSE06 functional, the overarching picture remains the same, but the eigenenergies change (Fig. S18). The resulting electronic structure using cRPA+FCI shows better agreement with experiment for $V_{Si,k}^{-1}$ than PBE-level calculations (Fig. S20).

Table S10. Hubbard interaction parameters from cRPA.

	bare	screened
$\langle U \rangle$	8.70	1.76
$\langle u \rangle$	4.24	0.56
$\langle J \rangle$	0.03	0.01

Table S11. Many-body states of the negatively charged silicon vacancy at k site as computed with FCI+cRPA on the 128 atom supercell using PBE single particle basis consisting of 4 orbitals (Figure S17).

Energy (eV)	Spin
0.00	3/2
0.18	1/2
0.21	1/2
0.23	1/2
0.64	1/2
0.70	1/2
0.90	1/2
0.93	1/2
1.04	1/2
1.24	3/2
1.38	3/2
1.51	3/2

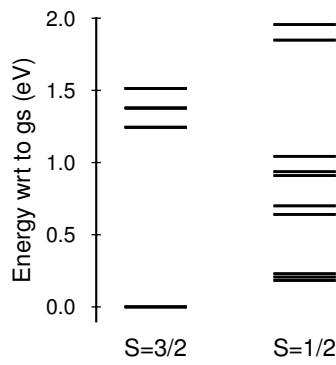


Figure S19. Many-body spectra for the k site negatively charged silicon vacancy as computed with FCI+cRPA on a 128-atom supercell and using PBE for the underlying DFT calculations.

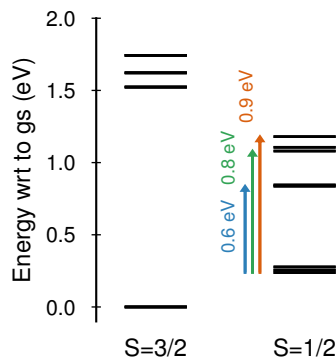


Figure S20. Many-body spectra for the k site negatively charged silicon vacancy as computed with FCI+cRPA on a 128-atom supercell and using HSE06 for the underlying DFT calculations.